FT-Infrared Spectroscopic and Computational Studies of the Matrix-Isolated Products Formed Following Gas-Phase Electron Bombardment of Rare-Gas/Organic Molecule Mixtures

by

Travis D. Fridgen

A thesis submitted to the Department of Chemistry

in conformity with the requirements for the degree of

Doctor of Philosophy

Queen's University

Kingston, Ontario, Canada

February, 1999

Abstract

The technique of gas-phase electron bombardment and subsequent matrix isolation (EBMI) of rare gases doped with oxalyl chloride, dichloromethane or methanol was utilized in the studies of the gas-phase chemistry of the oxalyl chloride radical cation, dichloromethane radical cation and methanol radical cation. The EBMI technique was characterized and the processes involved include electron-bombardment ionization of rare gas, ionization and excitation of the dopant molecules by a charge-transfer reaction with the rare-gas cation, unimolecular decomposition or isomerization of the energetic cation, followed by matrix isolation and subsequent neutralization of the product cations. It is concluded that the neutralization step occurs only if the electron affinity of the cation is similar to the photoelectron emission threshold of the matrix within which it is isolated. Excited states of neutral rare-gas species, although long lived, are shown to play an insignificant role in the chemistry observed.

Introduction of N_2 or CO to the initial gas mixture or increasing the concentration of dopant results in the quenching of internal energy of the initially-formed cation and products. Utilizing this technique, it was determined that carbonyl chloride radical cation is formed not only by cleavage of the C-C bond in the oxalyl chloride radical cation but, also by secondary decomposition of phosgene radical cation, formed by extrusion of CO from the oxalyl chloride radical cation.

EBMI of methanol doped in mixtures of rare gases has resulted in the

formation and spectroscopic characterization of $ArHKr^+$, Kr_2H^+, $ArHXe^+$ and Xe_2H^+ in predominantly argon matrices as well as $KrHXe^+$ and Xe_2H^+ in predominantly krypton matrices. The disagreement between observed and calculated asymmetric stretches of the homogenous species has been interpreted as being due to a strong interaction between the isolated triatomic cation and the matrix resulting in very large matrix shifts. It is proposed, based on density functional theory (DFT) calculations, that the matrix isolated cation is better characterized as a proton in a flattened octahedral matrix site with D_{4h} symmetry.

The presence of excess rare gas and other neutral bases in the gas phase has also been studied by DFT with respect to their catalytic effect on 1,2-hydrogen shift isomerization. It is concluded that Ar and Kr have only small effects on the barrier for $CH_3OH^{\bullet+}$ to $CH_2OH_2^{\bullet+}$ isomerization but that Xe and N_2 can sufficiently reduce the barrier such that it may be competitive with the lowest energy decomposition pathway of the methanol radical cation. Furthermore, the difference in proton affinity of the catalyst and that of the hydrogen leaving site is linearly related to the decrease in the barrier height from the uncatalyzed to the catalyzed hydrogen transfer.

Acknowledgment

Much has happened since the time I began undergraduate studies at Trent University almost one decade ago. The entire experience has been highlighted by meeting many lifelong friends, meeting many colleagues, meeting my wife and, of course, an amount of learning that will not likely be surpassed by any similar time frame in the years to come. There are many people to thank for this.

I would like to start by thanking my supervisor, friend and colleague, Dr. J. Mark Parnis for the opportunities to independently explore my interests and conduct research. Mark has aided in making my experience as a graduate student both enjoyable and prosperous.

I am also indebted to, and wish to thank Professor Raymond E. March for his guidance and support throughout my years at Trent University and for his considerable input into the writing of this thesis. Congratulations to Professor March on his recent retirement. I would also like to acknowledge Dr. Errol G. Lewars' assistance in the computational part of this work.

I am thankful to have worked and shared the experience as a graduate student with Dave Pedersen and Rick Lafleur, two friends who I will always cherish and colleagues I will always admire. I also will never forget the great times spent outside of school with Dave, Rick and Barry.

I would especially like to thank Lisa for her support when things were not

going so well, for her unconditional love, and for her patience, even when I tried it the most. The support and understanding of Mom and Dad as well as Lisa's parents, even though I know it was hard to understand, is greatly appreciated. I am so lucky to have such a large and warm family who always made it enjoyable to try to explain my work to.

I would also like to acknowledge Queen's University for their financial support as well as the Chemistry Department at Trent University for teaching assistantships and a great place to work.

For Lisa and our family

"Once in Hawaii I was taken to see a Buddhist temple. In the temple a man said, 'I am going to tell you something that you will never forget.' And then he said, 'to every man is given the key to the gates of heaven. The same key opens the gates of hell.'

And so it is with science. In a way it is a key to the gates of heaven , and the same key opens the gates of hell, and we do not have any instructions as to which is which gate. Shall we throw away the key and never have a way to enter the gates of heaven? Or shall we struggle with the problem of which is the best way to use the key?"

-Richard P. Feynman, 1918-1988

Statement of Originality

The gas-phase chemistry of the oxalyl chloride radical cation $(COCl)_2^{\bullet+}$ is still largely undetermined. In chapter three it is clearly shown that the phosgene radical cation, presumably formed by extrusion of CO from $(COCl)_2^{\bullet+}$, undergoes further decomposition to form a chlorine atom and a carbonyl chloride cation. This was shown by introduction of an inert gas-phase quenching agent which is a technique which was introduced through the course of this work. Similarly in chapter three, through electron bombardment matrix isolation experiments (EBMI) of rare-gas mixtures containing oxalyl chloride and dichloromethane, the processes occurring during these experiments have been elucidated.

EBMI experiments conducted on methanol/rare gas mixtures have resulted in the formation and spectroscopic characterization of mixed proton-bound dimers of rare gases with the structure $(RgHRg')^+$, where Rg=Ar, Kr or Xe but Rg≠Rg'. These species have, until now, remained elusive. Prior to this work, the experimental infrared spectra of these species as well as the homogenous rare-gas species (Rg=Rg') and the calculated infrared spectra have not qualitatively agreed let alone quantitatively. Qualitative agreement in the form of BP86/DN** density functional theory calculations are reported in this work. The poor quantitative agreement is shown to be due to the fact that the calculated spectra are for isolated gas-phase species while the experimental values are from matrix-isolated species. It is shown that the matrix-isolated proton-bound dimers are better described as

Rg_6H^+ rather than triatomic cations.

In these experiments, the methanol radical cation is formed in a gas-phase bath of neutral bases (rare gases, products such as CO, and impurities such as N_2 and H_2O). In the recent literature some calculations have been performed on neutral-base catalyzed intramolecular proton-transfer isomerization. The calculations reported in this thesis show that Ar and Kr are not likely to be effective in catalyzing the isomerization reaction from methanol radical cation to its distonic isomer. Xe and N_2, on the other hand, may be very effective catalysts. Furthermore, it is shown for the first time here that there is a distinct linear relationship between the proton affinities of the neutral bases and the lowering of the barrier heights for these isomerization reactions. Using this relationship, the observation of various isotopomers of decomposition fragments of the methanol radical cation, and the observation of elusive isomeric species from other works (utilizing the EBMI technique) are easily explained.

Table of Contents

List of Tables

List of Figures

Chapter 1

Introduction To Matrix-Isolation Spectroscopy And Rare-Gas Chemistry

1.1 Introduction

The present work deals largely with identification of products resulting from ion/molecule reactions and/or unimolecular isomerization or decomposition reactions occurring during EBMI experiments. The relatively new technique of electron bombardment matrix isolation (EBMI) combines two well-established techniques for the production and isolation, respectively, of novel species for spectroscopic characterization. Electron bombardment has been employed for ion production for roughly the last 100 years, while matrix-isolation spectroscopy has been used since 1954 for probing the chemical and physical properties of stable, unstable and reactive species. Much of this work focuses on the elucidation of the mechanism(s) to product formation by experimental and theoretical means.

The combination of electron bombardment and matrix-isolation spectroscopy to produce species for infrared spectroscopic detection in rare-gas matrices was first employed by Suzer and Andrews only a decade ago. They produced and spectroscopically characterized OH^- and NH_2^-, for the first time in a rare-gas matrix, by electron bombardment of a growing Ar matrix doped with either H_2O or NH_3, respectively.[1,2] The technique was taken up again in the early 90's when Szczepanski *et al.* generated and spectroscopically characterized the naphthalene radical cation by electron bombardment matrix isolation.[3] Since then, work in this laboratory, employing EBMI, has focused on aspects of gas-phase ion chemistry concerning the synthesis and characterization of novel organic and inorganic species,[4,5,6] and the effects of adding dopants to the initial gas mixture to resolve unimolecular ionic reaction mechanisms.[7]

First of all, it will be quite beneficial to give a general overview of the matrix-isolation technique. This will be accomplished in this introductory chapter along with a general discussion of the effect the matrix plays on the spectroscopy of isolated atoms, molecules and ions. Included in this chapter is a discussion of some techniques available to matrix-isolation spectrosopists for identification of matrix-isolated species, including an introduction to the very important technique of computational chemistry. As well, a discussion of matrix isolation and matrix-isolated species would not be complete without addressing techniques whereby the chemist generates these species for spectroscopic observation.

To a large extent, the chapters to follow will focus on species containing rare-gas atoms. Similarly, the presence of a large amount of rare gases in EBMI

experiments requires that thought be given to their impact on the chemistry observed during these experiments. The rare gases are generally given no more than cursory treatment in introductory chemistry texts and inorganic chemistry textbooks alike, and the discussions in these texts are not always current. In the last decade or so, many new ionic or neutral compounds have been generated which contain one or more rare-gas atoms. It will be shown in this work, that rare-gas chemistry is predicted to be much richer than their use as inert atmospheres would indicate. A brief history of rare-gas compounds and rare-gas chemistry will be given in the last section of this introductory chapter.

1.2 Matrix Isolation and Matrix-Isolation Spectroscopy

1.2.1 Introduction

Since its independent advent in 1954 in the laboratories of both G. Porter[8] and G.C. Pimentel,[9] matrix-isolation spectroscopy has become an invaluable tool in experimental chemistry and physics. This is evidenced by the thousands of published papers and numerous monographs,[10] all of which have been referenced in two bibliographical volumes on matrix isolation.[11]

Matrix isolation is a technique whereby reactive species such as radicals, ions, reaction intermediates or thermodynamically- and/or kinetically-unstable species are isolated in an inert solid or matrix. For isolation of reactive species, the requirements of the matrix material are that it must be: inert to reaction; rigid, such that no diffusion takes place; and, since species in matrices are detected by

spectroscopic means, transparent to radiation in the spectral region of interest. Most often, the rare gases meet all of these conditions. N_2, CO, CO_2, freons and organic glasses are also used as matrices, however, organic glasses may be quite reactive, especially with ions and radicals.

Generally, a species of interest (the precursor or guest) is diluted in an excess of matrix gas (the host). This gas mixture is deposited onto a transparent substrate which has been pre-cooled to temperatures ranging typically from 4 K for Ne matrices to 77 K and higher for organic glasses. Under these low-temperature rigid-solid conditions, bimolecular collisions are prohibited and reactions with an energy requirement of more than a few hundred joules per mole are prevented. Since the lifetimes of the guest are indefinite when matrix isolated, their properties may be probed at leisure by many different spectroscopic means.

Matrix isolation was initially intended as a tool for trapping reactive species such as radicals. For example, as early as one year after its inception Norman and Porter[12] prepared CS, ClO and various aromatic radicals by photolysis of CS_2 and ClO_2 etc. in hydrocarbon matrices at liquid nitrogen temperatures. The radicals were detected by absorption spectroscopy. This technique, which replaced transient detection techniques such as flash photolysis for the direct observation of radicals, is challenged today by laser techniques. With laser techniques one is able to obtain high-resolution spectra in the gas phase, free of perturbations by the matrix. Laser techniques are, however, complemented by matrix isolation since observation in rare-gas matrices is open to a wide spectral range. In contrast, a single laser is tunable over only a limited spectral range. Matrix-isolation plays an

important role in guiding the choice of laser and tuning of the lasers for high-resolution gas-phase studies.

Matrix isolation has also evolved to include fields such as synthetic organic[13] and organometallic[14] chemistry, photochemistry, [15]metal atom and cluster chemistry,[16] studies of molecular interactions,[17] reactive intermediates and molecular ion chemistry.[17,18,19]

1.2.2 Spectroscopy of Matrix-Isolated Species

A multitude of spectroscopic techniques have been employed for probing species isolated in cryogenic matrices. The most commonly-used techniques are UV/visible and infrared (IR) absorption spectroscopy, and electron spin resonance spectroscopy (ESR). Many others, including laser-induced fluorescence, Raman spectroscopy, and Mössbauer spectroscopy, have also been employed. While it is not intended to explain here the salient features of each of these different spectroscopic tools, it is beneficial to describe the effect of the matrix on the isolated species in comparison to gas-phase spectra. These effects, mainly on UV/visible and infrared spectroscopy of isolated guest species, will be discussed in this section. At least three excellent reviews of matrix effects on spectroscopic properties of matrix-isolated species exist[19,20,21] which go into much greater detail than is afforded in the following discussion.

The band centre of a vibrational absorption of a species isolated in a rare-gas matrix is shifted, usually but not invariable to lower energy. While the magnitude of the energy shift can be as much as 1% with respect to the gas-phase band centre,

the precise value depends solely upon the guest-host interaction. In Fig. 1.1 are shown the portions of infrared spectra, in the region of the CO stretching fundamental, of methanol isolated in N_2, Ar, Kr and Xe matrices. The position of the gas-phase band center of the CO stretching fundamental[22] is denoted by the vertical line. This figure clearly shows the effect of the different matrix cages on the position of the absorption.

In N_2, the absorption is shifted to higher energy compared with the gas-phase value by about 1 cm^{-1}. A repulsive interaction between the matrix cage and the oscillator must be in effect in order to account for this blue shift. In Fig. 1.2 is shown the effect on a diatomic potential of a repulsive interaction with the matrix cage where the modified potential is depicted by the dashed line. It is evident from this figure that the equilibrium bond distance has decreased to r_e' and the potential energy of the minimum has increased. The force constant of the vibrational mode depends upon the second derivative of the potential along the coordinate of the oscillation. It is clear from Fig. 1.2 that the potential has become steeper which results in a larger force constant and a blue shift in the position of the absorption.

In the rare-gas matrices, the CO stretch has shifted to lower wavenumbers (Fig 1.1). Contrary to the N_2 case, an attractive potential, of the order of van der Waals interactions, must be in effect. The result of this attractive potential depicted in Fig. 1.3 (dashed line) is to increase r_e' and lower the value of the potential minimum. Near the bottom of the potential (which is the only part of interest for infrared absorption spectroscopy in cryogenic matrices, *vida infra*), the well is less steep resulting in a smaller force constant, with respect to the unperturbed value,

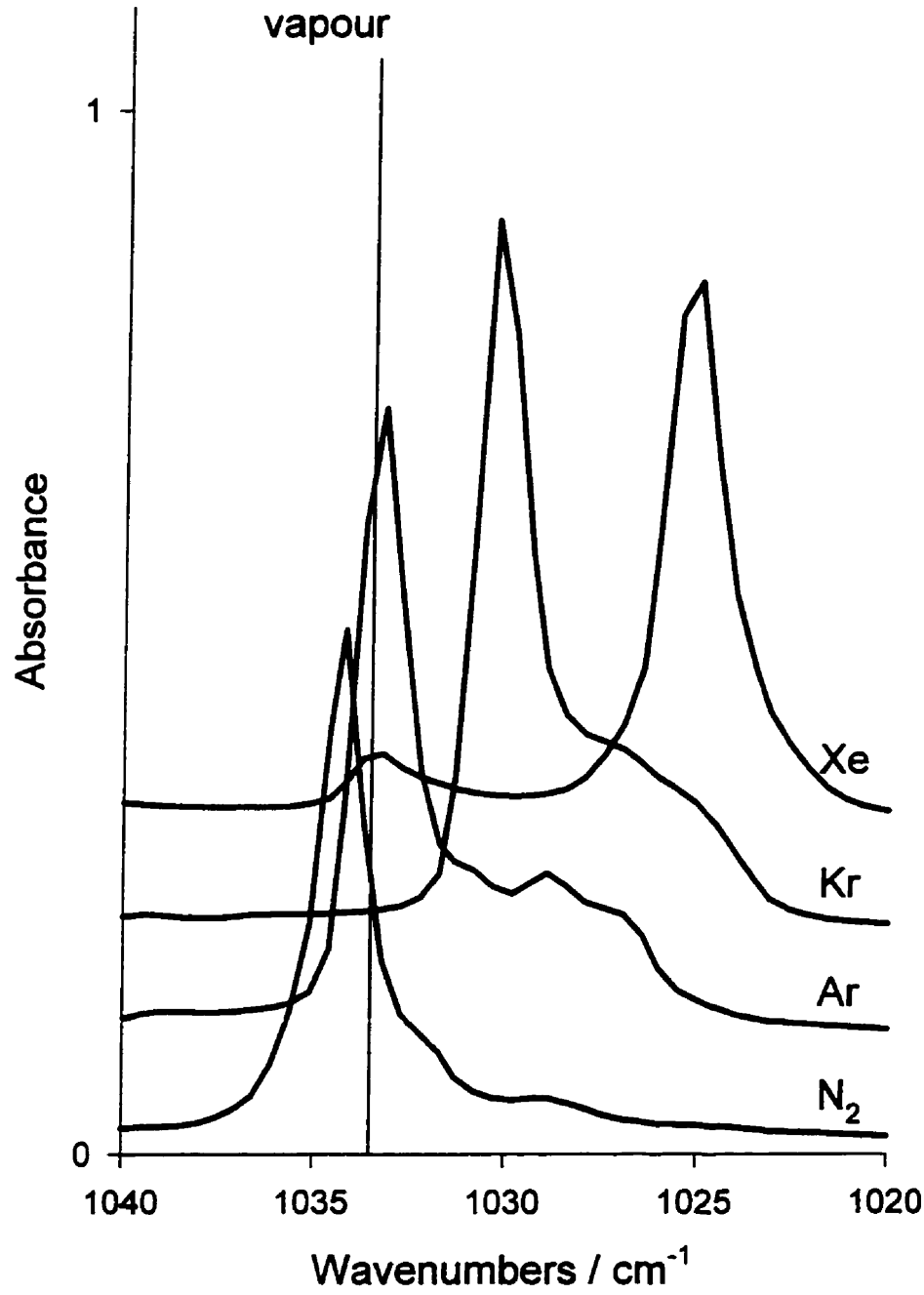

Figure 1.1. Portion of the FT-infrared spectrum of methanol isolated in N_2, Ar, Kr and Xe showing the effect of different environments on the CO stretching fundamental . The vertical line shows the position of the vapour-phase band centre.

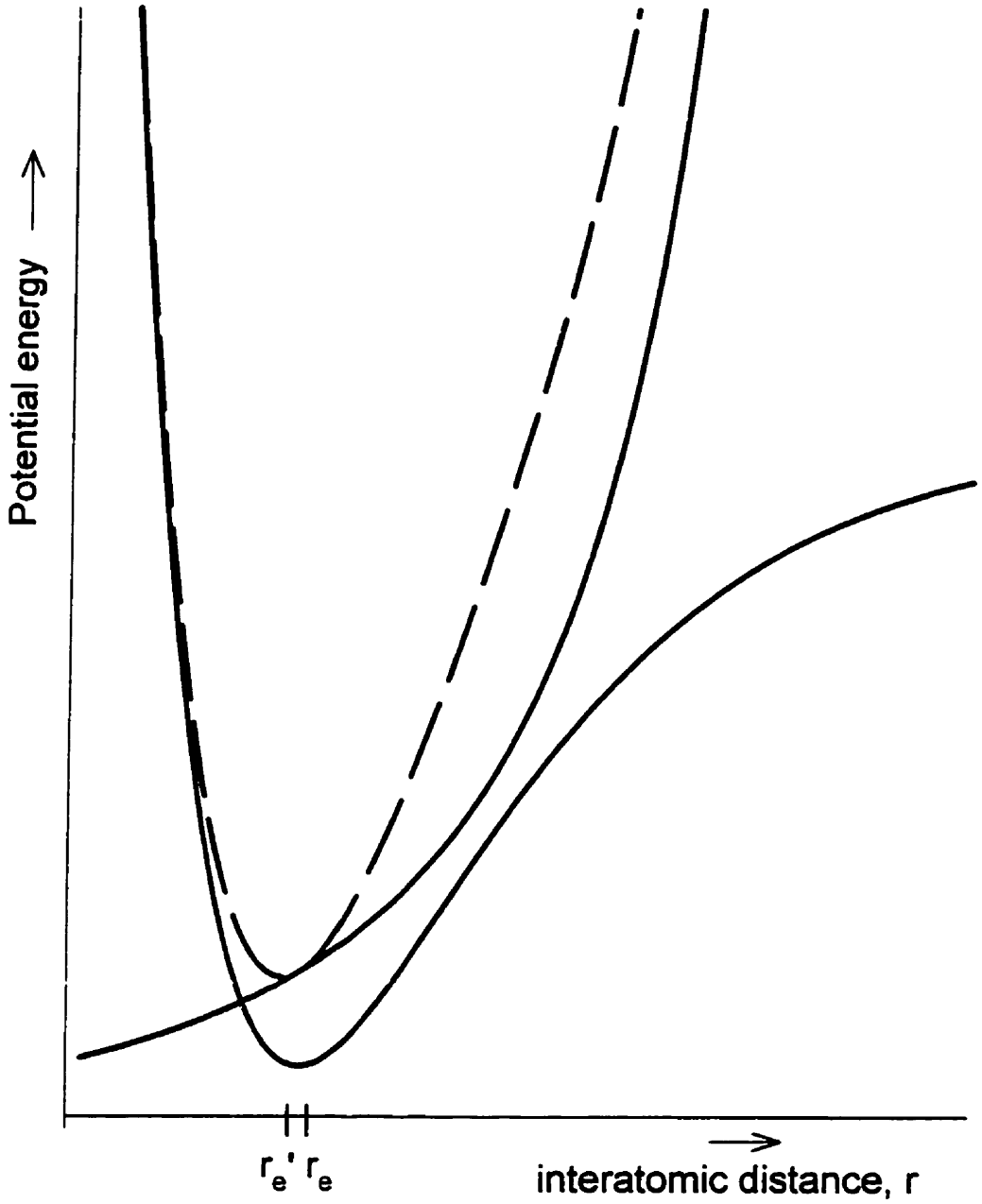

Figure 1.2. The effect of a repulsive potential between the host and guest on the anharmonic potential of a trapped diatomic guest.

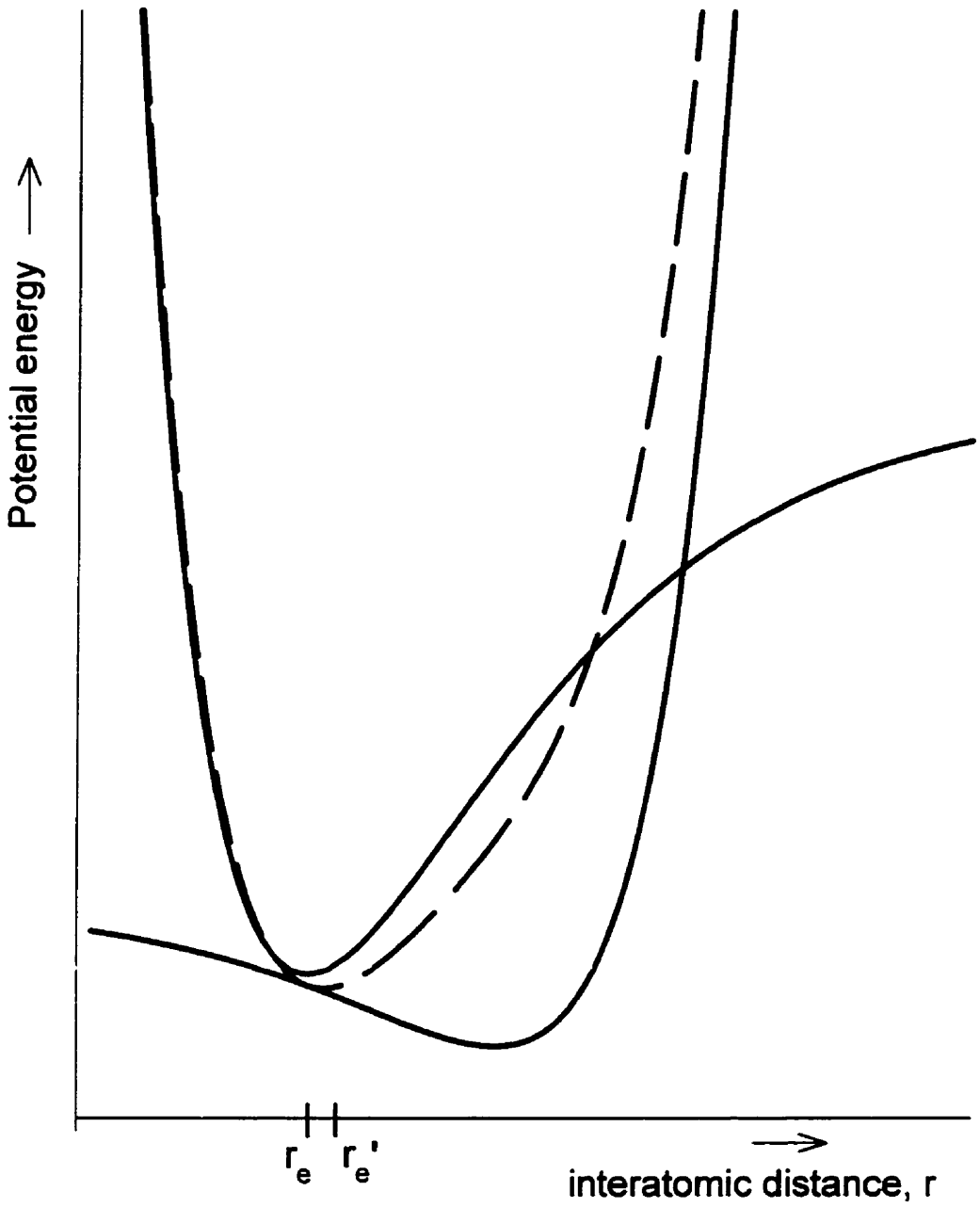

Figure 1.3. The effect of an attractive potential between the host and guest on the anharmonic potential of a trapped diatomic guest.

and the absorption wavenumber is red shifted. The shift is expected to become more prominent as the polarizability of the cage and, therefore, the depth of the attractive van der Waals interaction, increases; this explains the increasing magnitude of the shifts in Fig. 1.1 as the matrix changes from Ar to Kr and Xe.

Larger shifts have been observed for ionic species. These shifts have been shown to be greatly dependant upon the species in question as well as the matrix. For example, red shifts of 10.2, 6.0 and 2.9 % are observed for HI_2^-, HBr_2^- and HCl_2^-, respectively, on going from krypton to xenon matrices.[23] The differences in shifts can be correlated to the electronegativity of the halogen in these anions.

It is evident in Fig. 1.3 that, although the anharmonicity near the bottom of the well increases, near the top of the well there is a decrease in anharmonicity with respect to the gas-phase potential. An increase in harmonicity is also seen in the case of the repulsive guest-host interaction (Fig. 1.2) which would show up in the overtone progression in the infrared spectrum.

Shifts are also observed in UV/visible spectroscopy of matrix-isolated atoms and molecules. With respect to the electron cloud, when the excited species is larger than in the ground-state, the increased potential energy due to the repulsive force acting on the larger excited species will increase the transition energy. Similarly, when the excited species is smaller, an attractive potential may result and the absorption will be red shifted from the gas-phase value. These shifts can be more than 1000 cm^{-1} in magnitude, resulting in difficulties in assigning spectral features.

One of the major advantages of matrix isolation is that the infrared spectra

of molecules isolated in cryogenic matrices are less complicated than their gas-phase spectra. At cryogenic temperatures, population of vibrational levels other than the lowest state are improbable. Also, since the guest is trapped in a rigid cage, it is not common to observe rotational structure in the condensed medium. However, it has been observed that some simple hydride species, such as H_2O[24] and NH_3,[25] do rotate in rare-gas matrices since infrared spectra reveal vibration-rotation bands for these species. More recently, rotational transitions of CN have been observed[26] in xenon and krypton matrices by laser-induced infrared fluorescence. For these few examples, vibrational-rotational bands can be characterized employing the fact that marked changes occur reversibly in their relative intensities as the temperature of the matrix changes. This is due to different distributions of the rotational levels at different temperatures; the rotational transitions originating from $J \neq 0$ are more intense, and those from $J=0$ levels are less intense upon increasing the temperature of the matrix. The intensity change in the vibration-rotation bands is reversible, the original intensity distribution of the rotational bands is returned upon cooling to the original temperature.

Although the infrared spectrum is generally less complicated due to quenching of rotational structure and the absence of vibrational hot bands, splittings and satellite peaks, often called multiplets, are sometimes observed and can be attributed to a number of factors. As discussed above, an absorption may be shifted significantly from the gas-phase value due to interaction of the guest with the matrix cage. In an ideal matrix, the guest is trapped in only one matrix site. Due to

the non-equilibrium nature of the trapping process, however, a variety of trapping sites exist which can result in different shifts due to site-specific interactions. Two specific trapping sites are interstitial and substitutional. The latter site is a result of the guest occupying a position where a host atom would reside in the guest's absence. In fact, depending upon the size of the guest, it may substitute for two or more host atoms since a substitutional site in argon has a diameter of only 3.75 Å. Furthermore, the presence of the guest with a diameter greater than the substitutional site will perturb the rest of the host atoms, resulting in a local amorphous nature of the site. Depending upon the rate and temperature of deposition, one can envisage an infinite number of different trapping environments which would simply lead to broadening of the spectral features. Most often, deposition rates are sufficiently slow to allow only a few drastically different sites resulting in a small number of satellite peaks. It has been shown through ESR spectroscopy that hydrogen atoms occupy substitutional sites in all rare-gas matrices and that satellite bands are due to the occupation of interstitial sites.[27] Annealing, which is discussed in more detail below, can confirm that the satellite peaks are due to multiple trapping sites. Diffusion of the species at a slightly elevated temperatures can result in an irreversible redistribution to the more stable trapping site(s).

In a crystalline rare-gas solid, there exist two different types of sites in which only small species such as hydrogen atoms (or protons, see Chapters 4 and 5) may reside. These are the octahedral hole and the tetrahedral hole, otherwise known as interstitial sites, and can accommodate species with diameters less than 1.56 Å

and 0.85 Å, respectively, without significant distortion of the lattice.

The effect of multiple trapping sites is closely related to the presence of close and distant neighbor molecules. Impurities, for example from leaks can result in satellite peaks due to the various weak interactions of dissimilar neighboring molecules. Similarly, at high guest/host ratios, different interactions due to different orientations of neighboring guest species give rise to multiplets and, at very high guest concentrations, bands due to dimers and higher multimers may be observed. In these cases, it is beneficial to conduct studies in which the concentration of guest is varied. Splittings due to intermolecular interactions should decrease in intensity as the concentration of isolated species decreases to the limit where only one band is observed due to the isolated monomeric species.

The splitting of UV/visible bands can be illustrated with an example. The principal gas-phase electronic transitions of metal atoms, such as the alkali metals, copper, silver and gold, give rise to two lines due to the $^2P_{3/2} - {}^2S_{1/2}$ and the $^2P_{1/2} - {}^2S_{1/2}$ transitions; splitting arises from spin-orbit coupling in the excited state of the atom. In the matrix, however, these transitions give rise to three broad bands in the spectral vicinity of the gas-phase bands. This secondary splitting, which in the case of the lighter metal atoms is greater than splitting due to spin-orbit coupling, is due to the effect of the matrix on the $^2P_{3/2}$ state of the atom. This state is orbitally degenerate in the gas phase, and also if the atom is isolated in a substitutional site which has perfect octahedral symmetry. When the matrix site is distorted the symmetry about the atom is lifted, completely removing the three-fold degeneracy of the p-orbitals resulting in the observation of all three transitions. All electronic

transitions of guests, where a change of the orbital quantum number ℓ, should be effected in this way if they occupy unsymmetric lattice sites. ESR spectra of atoms such as N and the halogens, where the ground state has $\ell \neq 0$, will also be effected in this way.

1.2.3 Identification of Matrix-Isolated Species

Identification or characterization of neutral or charged species, whether in the gas phase or matrix-isolated, can commonly be supported by chemical intuition. However, when the expected appearance of a set of spectral features is observed, for example under experimental conditions where a common fragmentation product should be formed, considerable care should be taken to ensure unambiguous identification of the absorber. This is especially true when employing techniques for generating species, such as EBMI discussed above and in following chapters, where many species are produced and highly-complicated infrared spectra are produced. Further supporting evidence may be provided by the existence of characteristic group frequencies. However, the bonding in species with a deficiency or excess of electrons may result in considerable deviations from the spectral range in which similar vibrations are observed for stable or unreactive species.[28] In this section some of the 'tricks' used by matrix-isolation spectroscopists to aid in the identification and spectroscopic characterization of matrix-isolated species will be discussed.

1.2.3.1 Isotopic Substitution

The most definitive and widely-used technique for identification of species, whether matrix-isolated or gas-phase, is the use of isotopic substitution. The vibrational frequency v is dependant upon the reduced mass μ and the force constant k and is given by equation 1.1 for the case of a harmonic oscillator.

$$\nu = \frac{1}{(2\pi)}\sqrt{\frac{k}{\mu}} \qquad (1.1)$$

The force constant is a measure of the strength of the bond formed as a result of the coulombic attractions and repulsions within the molecule and are not affected by isotopic substitution. The reduced mass, however, is affected by isotopic substitution as it is dependent upon the masses of the constituent atoms. For a diatomic molecule A-B

$$\mu = \frac{m_A m_B}{m_A + m_B} \qquad (1.2)$$

For two isotopomers where a certain mode has reduced masses μ and μ*,

$$\nu^* = \nu\sqrt{\frac{\mu}{\mu^*}} \qquad (1.3)$$

For hydrogen/deuterium substitution μ_D/μ_H is 2 for a pure stretching vibration so that

ν_H/ν_D is 1.414. This is a maximum value for the frequency ratio; the value decreases for those modes where the degree of hydrogen stretching is reduced. In fact, for a symmetric stretching vibration of a molecule with $D_{\infty h}$ symmetry and hydrogen as a central atom, deuterium substitution has no effect on the vibrational frequency since hydrogen would not be expected to have any motion. Nevertheless, H/D substitution generally results in the largest shifts, and where possible, this method of isotopic substitution is recommended. The sharpness of the matrix-isolated spectral bands and the availability of high-resolution spectrometers makes infrared spectroscopy well suited to even C and O isotopic substitution. Detailed vibrational assignments of isotopomers may even result in information on the strengths of the chemical bonds. Yet, it is not necessary to purchase expensive isotopically-pure isotopomeric compounds; for most purposes, simple isotopic enrichment is adequate and many compounds enriched in isotopes such as ^2H (D), ^{13}C and ^{18}O can be readily purchased.

1.2.3.2 Irradiation

Irradiation studies utilizing filtered radiation can provide valuable evidence for identification of species. Many processes for generating matrix-isolated species also produce side products which complicate the infrared spectrum. Correlating the photolytic stability of spectral features according to the filtered radiation effecting their demise aids in sorting these absorptions. For example, irradiation of a matrix with red light, following EBMI of dichloromethane diluted in rare gases (discussed more fully in Chapter 3), resulted in the total elimination of infrared absorptions associated with isodichloromethane while all other features in the spectrum were

unaffected or only slightly affected by this process. Similarly, identification of photo-products or photo-fragments can provide evidence for the identification of the parent species.

1.2.3.3 Annealing

Annealing is achieved by simply increasing the temperature of the matrix substrate, taking care not to evaporate the matrix. The maximum annealing temperatures are generally 35 K for argon and 50 K and 65 K for krypton and xenon, respectively. Since the difference in average kinetic energy for species increases by only about 0.4 kJ/ mol^{-1} on going from 15 K to 65 K, the reason for annealing is clearly not to provide extra energy for unimolecular reactions other than simple dimerizations or conformer isomerization. Rather, annealing allows limited diffusion of species throughout the matrix. Small atoms such as hydrogen and fluorine are known to be mobile at slightly elevated temperatures.[29] It has also been shown, though, that even chlorine and bromine atoms undergo some diffusion, albeit to a limited extent, at temperatures as low as 20 K.[30]

As discussed above, annealing can aid in the identification of satellite bands due to site splitting and molecular aggregates. Matrix isolation of hydrogen atoms serve as a good example of this effect. Hydrogen atoms produced by photolysis of HI in argon at 4.2 K have been shown to occupy the substitutional site as well as both the octahedral and tetrahedral holes.[27] Furthermore, it was shown that at 12 K the atoms occupying tetrahedral holes were able to diffuse, while diffusion of those from the octahedral hole and substitutional hole did not occur until 23 K and 39 K respectively. Like irradiation of matrices, sorting of spectral features

according to their thermal stability and identification of annealing products can provide further evidence as to the identification of a matrix-isolated species.

1.2.3.4 Presence of Other Spectral Features

As discussed in section 1.2.2 small hydrides such as water can rotate in rare-gas matrices and vibration-rotation bands are observed in the infrared spectra of these matrix-isolated species. The relative intensities of the vibration-rotation bands are, under normal circumstances, determined by the temperature of the matrix at the time when the spectrum was being recorded. Jacox[31] observed that when ionic species are present in the matrix, the relative intensities of the vibration-rotation bands of water differ from those when no ionic species are present. That is, the presence of ions tends to hinder rotation of water in its matrix cage, and the bands associated with rotating water diminish in intensity while the purely vibrational bands increase in intensity (see Fig. 1.4). Although the absence of these vibrational-rotational bands obviously cannot result in identification of a species, it can suggest that charged species may be present.

1.2.3.5 Computational Chemistry

Computational chemistry has now reached a level whereby accurate predictions of thermodynamic and kinetic properties rival even some of the best experimental efforts. In fact, Szulejko and McMahon[32] list direct *ab initio* calculation as one of the three methods for obtaining accurate data for gaseous ion energetics. Curtis *et al.* even claim that determinations of gas-phase proton affinities by *ab initio* calculation are as reliable as the best experimental methods stating that "For a

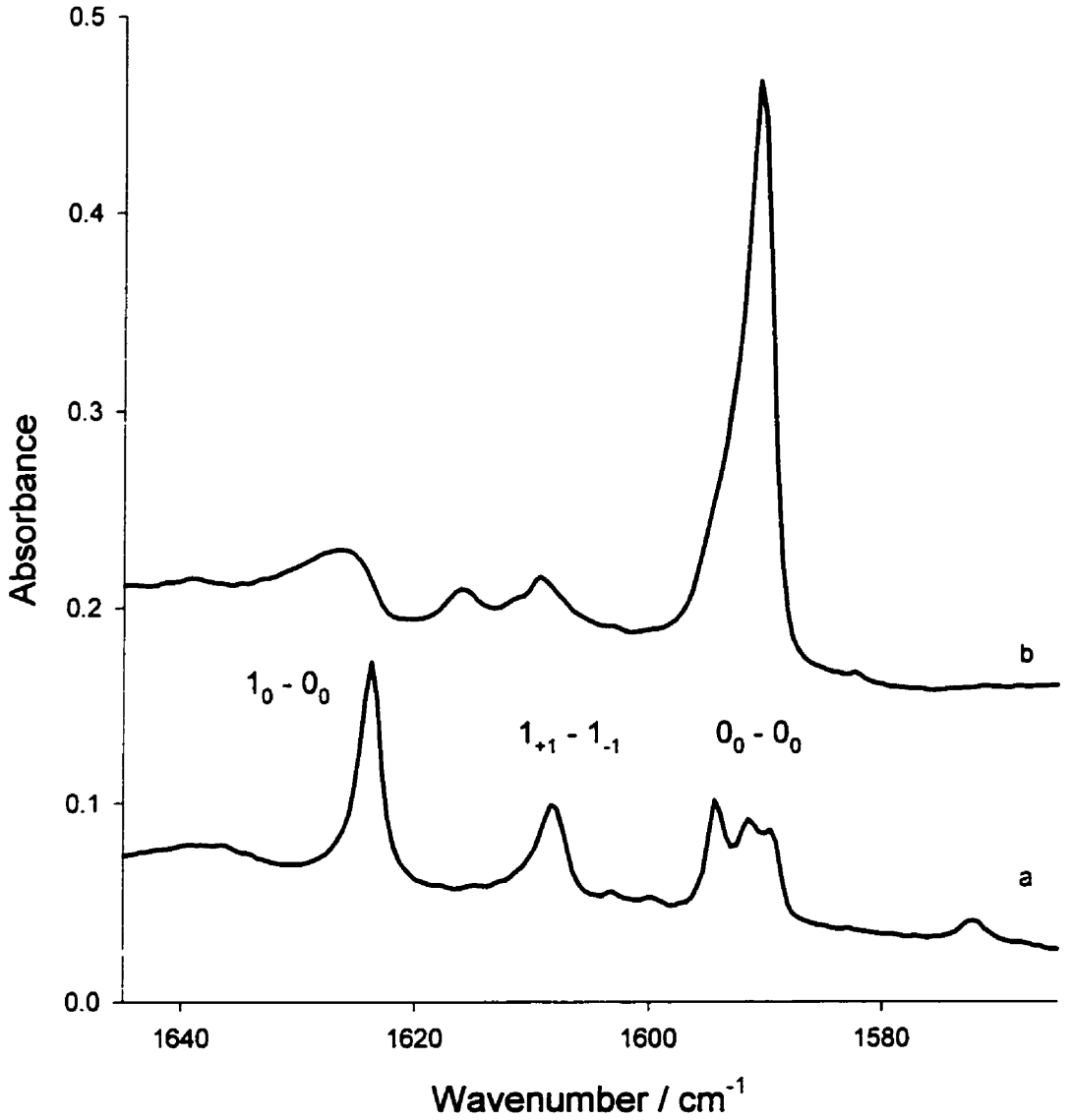

Figure 1.4. Portions of the FTIR spectra in the H_2O bending region recorded a) on 8 h straight deposition of dichloromethane and b) after 8 h EBMI of dichloromethane. The water in these spectra are believed to be due to impurities from leaks.

number of species, the results of G2 theory indicate that values in thermochemical tables are in error and should be re-examined."[33] Calculations based on the G2 procedure are much more reliable than density functional theory (DFT) methods for thermodynamic quantities. This was concluded recently by utilizing a set of 146 experimentally well-established ionization potentials and electron affinities to compare with calculated values.[34] However, the use of second-order Møller-Plesset perturbation theory in conjunction with triple-ζ basis incorporating additional polarization and diffuse functions in G2 theory[33] makes the use of large, expensive computers essential. Use of the more computationally-expedient DFT can be advantageous, but its limits with respect to thermochemical results must be considered.

Comparison of calculated infrared spectra with experimental infrared spectra can be quite beneficial when attempting to characterize newly-formed species. A portion of the work reported here utilizes the advantages of *ab initio* computational chemistry in the spectroscopic characterization of novel species in cryogenic rare-gas matrices. In order to compare calculated infrared spectra with experimental wavenumbers, scaling factors are normally required. Scaling factors for DFT methods range from 0.96 to close to unity, while HF and MP2 calculated wavenumbers are generally scaled by 0.90 and 0.94-0.95, respectively.[35] While DFT calculations of thermodynamic properties are inferior to other computational methods incorporating electron-correlation, they prove to be quite precise with respect to infrared wavenumber calculations. In Table 1.1 are listed the experimentally-determined vibrational wavenumbers[22] for methanol and those

Table 1.1. A Comparison of calculated and observed vibrational wavenumbers for neutral methanol.

vibration	observed[a] / cm^{-1}	(BP86/DN**) / cm^{-1}		HF/6-311G**		MP2/6-311G**	
		calc	scaled	calc	scaled	calc	scaled
ν_1 (a'), ν(OH)	3681.5	3742.3	3731.1	4185.3	3733.3	3924.2	3680.9
ν_2 (a'), ν(CH_3) asym	2990.0	3073.3	3064.1	3256.7	2905.0	3183.3	2985.9
ν_9 (a"), ν(CH_3) asym	2970.4	2997.2	2988.2	3184.5	2840.6	3108.7	2916.0
ν_3 (a'), ν(CH_3) sym	2844.2	2942.3	2933.5	3140.0	2800.9	3044.4	2855.6
ν_4 (a'), δ(CH_3) asym	1477.2	1468.2	1463.9	1630.1	1454.0	1537.6	1442.3
ν_{10} (a"),	1465.3	1466.0	1461.6	1617.5	1442.8	1518.1	1424.0
δ(CH_3)asym	1454.5	1453.1	1448.4	1615.2	1440.8	1517.8	1423.7
ν_5 (a'), δ(CH_3) sym	1339.5	1344.6	1340.6	1489.1	1328.3	1403.5	1316.5
ν_6 (a'), δ(COH)	1145	1136.7	1133.3	1277.6	1139.6	1196.9	1122.7
ν_{11} (a"), $\gamma_\perp$(CH_3)	1074.5	1065.4	1062.2	1179.3	1051.9	1114.6	1045.5
ν_7 (a'), $\gamma_\parallel$(CH_3)	1033.5	1016.4	1013.5	1160.3	1035.0	1089.1	1021.6
ν_8 (a'), ν(CO)	271.5[b]	268.2	267.4	358.6	319.9	346.6	325.1
ν_{12} (a"), τ(OH)							
Scaling factor (standard deviation)		0.997(±0.016)		0.892(±0.044)		0.938(±0.050)	

a: From J. Mol. Spectrosc. 52, 14 (1974); reference 22.

b: Argon matrix

calculated at the BP86/DN**, HF/6-311G**, and MP2/6-311G**[36] method/basis sets. It is readily seen from this table that the scaling factor required to bring the DFT-calculated wavenumbers (BP86/DN**) in to agreement with the experimental wavenumbers is far less than the scaling factor required for both the HF- and MP2-calculated numbers. Even more important is the standard deviation (SD) calculated for the scaling factors for each of these methods. The BP86/DN** calculated SD is a mere 0.016 while that for the HF and MP2 methods are 0.044 and 0.050, respectively, indicating that the scaling factor for the BP86/DN** wavenumbers can be applied with greater confidence than can the scaling factors for the other methods. An analysis of the calculated IR and Raman spectra of cubane[37] showed essentially the same results. The average scaling factor for MP2/6-31G*-calculated wavenumbers is found to be 0.98 with a SD of 0.027 while the B3LYP-, B3P86-, B3PW91- and BLYP-calculated wavenumbers (all using the 6-31G* basis set) had average scaling factors of 0.96±0.015, 0.96±0.016, 0.96±0.017 and 1.00±0.018, respectively. These SD values compare well with results of the much more thorough study by Scott and Radom[35] on 1066 individual vibrations; their results show that on average the DFT-calculated wavenumbers are more dependable than MP2- or HF-calculated wavenumbers based on the percentage error of the scaled values compared with experimental wavenumbers.

1.2.4 Generation of Ionic or Neutral Species for Matrix Stabilization

1.2.4.1 Photolysis

The experimental part of the work reported in later chapters does not utilize irradiation as a technique for generating species for spectroscopic observation in the matrix. However, since irradiation of the matrix is a technique used to differentiate between absorptions observed after EBMI experiments as discussed above in section 1.2.3.2., a brief discussion is given here of the types of reactions which are possible when a matrix doped with molecular species is irradiated.

One of the most widely-used methods for generating a desired species is the production *in situ* by irradiation of a matrix doped with a suitable precursor. Indeed, one of the strengths of matrix isolation is that one is able to convert a stable compound into an isomer that would be unstable under conditions other than within a cryogenic matrix. In the absence of quenching, the nascent isomerized species retains the excitation energy, at least sufficient to surmount the reverse energy barrier and may back isomerize. In a cryogenic matrix, it is possible that the energetic isomer will become stabilized by the dissipation of energy to matrix phonon modes.

Two mechanisms for isomerization of small molecules are dissociation-

$$ABC \xrightarrow{h\nu} A + BC \rightarrow BCA \qquad (1.4)$$

$$ABC \xrightarrow{h\nu} \begin{array}{c} A \\ / \backslash \\ B\text{—}C \end{array} \rightarrow BCA \qquad (1.5)$$

recombination and a concerted mechanism via a cyclic intermediate (Eq. 1.4 and 1.5, respectively).[15b]

Varetti and Pimentel[38] displayed a beautiful example of a quantitative reversible isomerization process. They converted the stable asymmetric isomer of N_2O_3 to the higher energy symmetric isomer. The structure of the symmetric isomer was confirmed using the $O^{15}N^{14}NO_2$ isotopomer which photochemically isomerized yielding only one isotopomer. The reverse photochemical isomerization yielded both the precursor and $O^{14}N^{15}NO_2$.

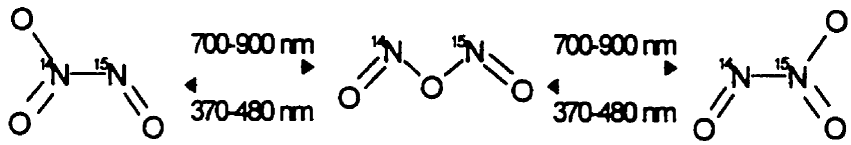

(1.6)

Photochemically-induced intermolecular reactions are also quite plentiful. Irradiation of N_2O produces $O(^1D)$ which is mobile enough in the matrix to find and react with other matrix dopants producing the oxidized compounds. When argon matrices containing small amounts of N_2O and inorganics such as CO and CO_2 or hydrocarbons such as methane and ethane are irradiated with UV radiation, products such as CO_2, CO_3, methanol and ethanol are observed.[39] These *primary reaction products* would be highly excited and not observed in the gas phase due to rapid dissociation. This example clearly illustrates the ability of the cryogenic matrix to quench and to stabilize excited reaction intermediates.

Another important aspect of photochemistry in matrices is the role of the

cage effect. Bondybey and Brus[21] discuss this effect in detail. It has been observed that species such as the mixed halogen compound ICl have very low quantum yields for permanent photochemical dissociation even at energies as much as 77 kJ mol^{-1} above the excited-state dissociation barrier, yet, fluorescence from lower-energy bound states are observed. The effect of the cage is not to induce additional quantized vibrational levels in the dissociative region, rather the cage effect is dependent upon the lifetime of the excited state. For dissociation or isomerization processes which occur slowly, the elastic rare-gas solid resolvation of the product(s) is efficient and dissociation or isomerization is not hindered. However, for processes that occur more rapidly than the resolvation time, such as the photochemical dissociation of ICl, a Cl atom carrying large amounts of kinetic energy simply collides with a nearest neighbor Ar atom transferring its kinetic energy. Since emission from bound states is observed, this kinetic-energy transfer must be efficient and, after a few collisions, sufficient kinetic energy is lost such that ICl relaxes into a bound excited state.[21]

Ions such as Rg_2H^+ (Rg=Ar, Kr or Xe) and X_2H^- (X=Cl, Br or I) have been photogenerated in rare-gas matrices.[23] The former will be discussed extensively in chapters 4 and 5. The bihalide ions (X_2H^-) were first produced by vacuum-UV photolysis of rare-gas matrices doped with HX. All plausible mechanisms involve an initial photochemically-induced dissociation of HX to H^+ and X^-. It is likely that the ion pair is not effected by the cage effect due to the size of H^+ and its high mobility in rare-gas matrices. There are two possible steps for the formation of the bihalide anion, one of which is the direct reaction of X^- and HX. It is probable that

the size of X^- precludes it from having high mobility and so this mechanism must include the assumption that HX is in the vicinity of the initially-produced X^-. The other possibility is the photo-induced electron transfer from X^- to HX dimers that would directly form bihalide anions and H atoms. It was shown earlier that the same matrices doped with Cs only required radiation from a Mercury arc, rather than vacuum-UV light, to produce the same species.[40] The process occurring in the Cs-doped experiments is photo-induced electron transfer from Cs to $(HX)_2$ which gives more merit to the photo-induced electron-transfer mechanism without Cs present.

1.2.4.2 Microwave Discharge

The passage of a suitable precursor diluted in argon through a microwave discharge and the subsequent freezing of the products onto a matrix substrate was used in an early attempt to produce free radicals for spectroscopic observation. This technique was only suitable for production of small free radicals such as $NH_2^\bullet$ and the NH diradical due to extensive fragmentation of the precursor. A more general method is the passage of Ar/H_2 mixtures through a microwave discharge so as to produce H atoms for reaction with other molecules introduced into the cryogenic cell through a separate deposition port.

Experiments conducted by passing pure rare gases through the microwave discharge have also been fruitful in the production of new radicals and ionic species for subsequent spectroscopic characterization.[19,31] Jacox[31] passed argon or krypton through the microwave discharge and reacted the emanate with chloroform before condensation on the matrix substrate. Products of these reactions included $HCCl_2^-$, $HCCl_2^+$, CCl_3^+, $CCl^\bullet$, $CCl_3^\bullet$ and $HCCl_2^\bullet$. These species are thought to be products

of the reaction between chloroform and metastable Ar or Kr. In the case of Ar the longest-lived metastable states (Ar*) would transfer 11.54 or 11.72 eV to the chloroform molecule on collision. This energy is sufficient to produce all of the products listed above. However, the metastable states of Kr (Kr*) transfers only 9.91 or 10.64 eV which is insufficient to produce either $HCCl_2^+$ or CCl_3^+. The explanation Jacox gives for the presence of $HCCl_2^+$ and CCl_3^+ is that the interaction of Kr* with the precursor produces the corresponding free radical which is subsequently ionized by a second interaction with Kr*. Even the reaction between the higher energy Ar* with chloroform to produce $HCCl_2^+$ is only exothermic by about 18 kJ mol^{-1} which leaves little energy to overcome any significant barrier to decomposition. Jacox does not discuss the possibility of Ar^+ or Kr^+ being involved in these experiments which, in a charge-transfer collision, would transfer in excess of 400 and 250 kJ mol^{-1}, respectively, to the newly-formed chloroform radical cation. Charge transfer collisions are ruled out simply due to the absence of substantial Ar^+ emissions from the microwave discharge tube which is not necessarily proof that substantial amounts of ground-state Ar^+ (or Kr^+) are not present.

In electron bombardment matrix isolation, rare gases are doped with small amounts of precursor such as methanol or dichloromethane. These mixtures are passed through an electric discharge above the matrix substrate. In the chapters to follow, it will be shown that the chemistry observed is not a result of Penning ionization (ionization following collision with Rg*) but is more likely a result of charge exchange ionization reactions between the dopant species and rare-gas cations.

1.2.4.3 Electron Bombardment

It is not the intent in this section to discuss in detail the technique of EBMI. Rather, short descriptions of experiments which involve both the electron-bombardment and matrix-isolation techniques will be given.

Suzer and Andrews were the first to couple electron bombardment and matrix isolation for the production and subsequent IR spectroscopic characterization of novel species. In the apparatus designed by Suzer and Andrews, the electron beam impinged on a rare-gas matrix doped with various small precursors such as H_2O and NH_3; in this manner, OH^- and NH_2^- were spectroscopically characterized for the first time.[1,2]

A similar arrangement for producing charged radicals for ESR characterization has been used extensively by Knight and co-workers.[41,42] Bombardment of a growing neon matrix with 50 eV electrons produced charged species such as $N_2^{+\bullet}$,[41] $H_2CO^{+\bullet}$,[43] and various isotopomers of $CH_3OH^{+\bullet}$ [44] which were characterized by ESR spectrosopy. Attempts to generate ions such as $CH_3OH^{+\bullet}$ in argon matrices[44] and other small ions in freon matrices[42] have proved to be unsuccessful. Knight notes that, when attempting to trap cation radicals having electron affinities above 10-11 eV, it is necessary to use neon matrices and attributes these observations to the extreme chemical inertness, low polarizability and the large conduction band-gap of neon.[42]

It is unlikely that in any of the experiments either by Suzer and Andrews or by Knight and co-workers that any appreciable amount of the ions observed resulted from gas-phase ionization of a suitable precursor. The ions observed were

more likely products of either direct electron impact of the matrix-isolated species or a series of charge transfers throughout the solid matrix beginning with electron-impact ionization of a matrix host atom and ending with charge-transfer ionization of the guest species. Modifications to the electron-bombardment matrix-isolation apparatus by Szczepanski *et al.*,[3] and subsequently duplicated by Zhang[45] and utilized for the present work, ensures that ionization occurs in the gas phase by directing the electron beam parallel to the growing matrix.

1.2.4.4 Mass-Selection Matrix Isolation

Information regarding the structure of many ionic species is still quite sparse. Mass spectrometrists attempt to elucidate the structure of gas-phase ions in collision-induced dissociation experiments whereby the structure of the parent ion is determined following high- or low-energy collisions with a target gas and mass-analysis of the charged fragments. The neutral fragments of these collisions can also be analyzed following their ionization in a second collision. These structure determinations are, however, indirect since the parent ion itself is not observed directly.

Most methods of producing neutral or charged species for isolation and direct spectroscopic observation in a cryogenic matrix (only some of which are discussed above) have a inherent flaw in that there are always many other species isolated along with them. These 'impurities' are due to the precursor, side reactions and to further reactions of the desired isolate. The impurities can greatly complicate the matrix spectra and hinder the observation or identification of the intended isolate. Unfortunately the EBMI technique shares this complication.

Simplification of the matrix spectra can be effected by mass selection of the isolate. These two needs, to directly determine the structure of ionic species and to simplify the matrix spectra, led directly to the coupling of mass spectrometry with matrix isolation. Maier and co-workers[46] designed an instrument where ions were generated in a modified residual gas analyser and, following mass selection in a quadrupole mass filter, were co-deposited onto a cold substrate with neon. Success was achieved by the observation of the electronic transitions of both C_2^+ and $C_4H_2^{+\bullet}$ ions.

A modification of this instrument was made by Sabo *et al.*[47] who had two modified residual gas analysers; one for positive and one for negative ions in order to maintain charge neutrality. To date, vibrational spectra of mass-selected ions such as $CS_2^{+\bullet}$,[47,48] $CS_2^{-\bullet}$,[48] $CO_2^{+\bullet}$,[49] and $CF_3^{\bullet}$ [50] have been observed in neon matrices utilizing their instrument.

It was also shown that addition of small amounts of CO_2 to the neon diluent increases the spectral intensity due to both cations and CO_2^-. Their explanation is that when CO_2 is bound to the copper matrix-substrate support it has a bent geometry which allows it to accept an electron with little or no energy barrier. Once the matrix reaches a certain potential, the CO_2^- anions are attracted to and deposited in the matrix maintaining charge neutrality. This behaviour is only observed with neon matrices and not with argon matrices possibly because argon freezes to the copper block and inhibits CO_2 from sticking to it.[49] It was deduced that although they did not observe counterions in some of their experiments, such as those conducted in argon, the presence of an observable amount of cations

requires that they be present so that the matrix maintains charge neutrality.

Some success has also been achieved by coupling an ion trap with the matrix isolation apparatus. However, due to the pulsed nature of the ion trap, deposition times on the order of days were required to observe infrared absorptions corresponding to protonated acetone.[45]

It may seem that only investigations of ionic species are appropriate by coupling mass selection with matrix isolation. However, the advent of neutralization-reionization mass spectrometry[51] (NRMS) for the study of neutral species has brought mass spectrometrists into the field of indirect structural elucidation of neutral species. Likewise, Lindsay and co-workers,[52] Rivoal *et al.*[53] as well as Moskovits and co-workers[54] have generated metal cluster ions by sputtering a metal rod with high-energy argon cations. The cluster ions are then mass selected by a pair of quadrupole mass filters, slowed down with a retarding potential[55] and, prior to being condensed in an argon or krypton matrix, they are neutralized with a mesh grid kept at a slightly negative potential or a low-energy electron beam. The mass-selected matrix-isolated neutral clusters are then observed by various spectroscopic means. Thus far, the groups of Lindsay and Rivoal have simply been characterizing clusters composed of various metals and different sizes by using spectroscopic tools such as UV/Vis,[52,53] laser-induced fluorescence[56] and Raman scattering.[57] Only one result has been reported whereby a reactant has been introduced with the neutral clusters.[54] In these experiments, the infrared spectra revealed bands which were associated with Fe, Fe_2 and Fe_3 ligated to various degrees with CO.

Although it has not been attempted, the mass-selection matrix isolation

technique has the potential for the selection of organic cations for neutralization and infrared detection in the cryogenic matrix. Possible isolates of interest utilizing this technique are OCCO, oxirene, and the isomers of formamide which have eluded direct observation to date but whose existence has been indicated in NRMS experiments.[58,59]

1.3 The Chemistry of the Rare Gases

1.3.1 The Early Years: Fluorine and Oxygen Compounds

Since the discoveries of argon in 1894 by Rayleigh and Ramsay and of krypton and xenon four years later by Ramsay and Travers, attempts have be made to include these atoms in chemical compounds.[60] Many of the early attempts failed but, in 1933, Yost and Kaye observed an etching in the quartz of their reaction vessel when attempting to produce a xenon fluoride. They reported both that they had failed in making a xenon-containing compound[61] but, that they had observed the etching. Many now believe that Yost and Kaye had succeeded in producing XeF_6, which is a strong oxidizing agent, and had probably reacted with the quartz vessel.[60] With the report of this failure, however, and the acceptance by many chemists that the rare gases were indeed inert, believing unreservedly in the octet rule, no further attempts were reported for 30 years. It is pointed out by Laszlo and Schrobilgen[60] that although Linus Pauling predicted the ability of xenon to form compounds[62] and that he was instrumental in Yost and Kaye's attempts, he succumbed to the notion that the rare gases were completely inert by not including

any mention of their possible chemistries in his many texts and his statement in a 1961 paper,[63]

> "Xenon is completely unreactive chemically. It has no ability whatever to form ordinary chemical compounds involving covalent or ionic bonds."

This statement by such a renowned chemist may also be the reason why the rare gases are still considered inert by many today. It may also be responsible for the octet rule being taught vigorously to students in their inaugural studies of periodicity and chemical compounds even though the vast majority of the elements do not obey such a rule.

In 1962, shortly after Pauling's statement, three independent and almost simultaneous accounts of the production of xenon-containing compounds entered the literature. Bartlett[64] gave the first account of his success of the direct reaction between PtF_6 and Xe to produce $XePtF_6$ at his laboratory at the University of British Columbia. XeF_2 and XeF_4 were produced by Hoppe *et al.*[65] and Classen *et al.*,[66] respectively, that same year. The following year, XeF_6 was generated at high pressures and low temperatures in an excess of F_2.[67] The oxides of xenon are generally formed by reacting water or some oxygen-containing compound (SiO_2) with the xenon fluorides. These early rare-gas compunds were predicted to have use as fluorinating agents and, in fact, XeF_2 is widely used as a fluorinating agent by synthetic organic chemists.[68] The physical properties of the fluorides and their oxide derivatives as well as the bonding properties of these species can be seen

in reviews and the many papers concerning these compounds.[69]

It is evident that the early years of rare-gas chemistry included only xenon combined with the most electronegative elements, fluorine and oxygen. However, a bond between xenon and nitrogen in the form of $FXeN(SO_2F)_2$ was first reported in 1974[70] and since then there have been many other compounds containing Xe-N bonds such as $Xe[N(SO_2F)_2]_2$ and $[(FSO_2)_2NXe]_2F^+AsF_6^-$.[71] Fourteen years later, an ionic krypton-containing compound, $(HCNKrF)^+(AsF_6)^-$, was prepared and was the first example of a compound with a Kr-N bond.[72]

Moving to the left of the periodic table, Xe-C bond strengths in methylenexenonium cation $XeCH_3^+$ have been determined to be 230±10 kJ mol^{-1}, by methyl-cation exchange studies between CH_3F and Xe in an ion cyclotron resonance mass spectrometer.[73] Neutral compounds with a xenon-carbon bond first became known with the synthesis of $Xe(CF_3)_2$.[74] More recently ionic compounds with Xe-C bonds have been synthesized.

1.3.2 Matrix-Isolated Rare-Gas Species

Over the last decade or so, most of the compounds containing rare-gas atoms have been produced and isolated in cryogenic rare-gas matrices and characterized by UV/visible or infrared spectroscopy. Even though these species are observed in cryogenic matrices, it should not be concluded that they are unstable at room temperature. Typical routes to their formation leave them with much excitation energy and the technique of matrix isolation provides an ideal medium for dissipation of this energy. For example, an interesting complex,

F_2C=CXe, has been characterized by infrared spectroscopy in an argon matrix and is calculated to be bound by about 13 kJ mol^{-1} with respect to Xe and difluorovinylidene. The magnitude of this binding energy suggests that this charge-transfer complex should be stable in the gas phase at normal ambient temperatures.[75]

A host of xenon-containing molecules with new bonds such as HXeCl, HXeBr, HXeI,[76,77] HXeCN and HXeNC[78] have recently been characterized by matrix-isolation infrared spectroscopy. These molecules are formed by first photolyzing monomeric HX (X=halogen or CN) to produce isolated H atoms and X. Annealing of the matrices activates the hydrogen atoms which react with Xe atoms surrounding X producing the Xe compounds. Conversion of HXeNC to HXeCN can be achieved by exciting the Xe-H and C-N stretches with infrared radiation suggesting a low barrier to isomerization.[78] Similar compounds HKrCl[76] and HKrCN[78] have been generated in the same way, the latter being the first example of a bond between krypton and carbon. Krypton compounds with the less electronegative halogens Br and I are calculated to be unbound unlike all of the species mentioned above. These calculations suggest that similar argon compounds with Br and I as the halogen will not be bound either. Calculations do predict, however, HArF and HArCl to be bound molecules with the former having a dissociation energy of about 17 kJ mol^{-1}. It is expected that solvation by the matrix and the cage effect would further increase this barrier.[76] The bonding in these molecules is described as charge-transfer with the rare-gas donating electron density to the halogen and, at the extreme of charge transfer, the

molecule would look like a strongly bound HRg^+ cation bound to X^-.

Along with the absorptions due to the HXeX molecules listed above, the experiments by Pettersson *et al.* produced species, without the electronegative halogen, deduced to have the structure HXeH.[79] This structure was confirmed by the observation of the HXeD and DXeD isotopomers and by *ab initio* calculations. The nature of the bonding in this molecule is assumed to be analogous to the valence bond description of xenon difluoride and may be described as a resonance hybrid of H^--Xe^+-H and H-Xe^+-H^- with a positively-charged xenon atom. Similarly, Feldman and Sukhov[80] irradiated xenon matrices doped with hydrocarbons with 1.2 MeV electrons and, after annealing the matrices, observed growth of infrared bands ascribable to HXeH. Excellent evidence that these species are formed from neutral molecules comes from the monitoring of hydrogen atom ESR signals and HXeH infrared bands as functions of annealing temperature. The abundance of hydrogen atoms was found to be directly related to the abundance of HXeH leading to the conclusion that they are formed by neutral atom reactions.[81]

1.3.3 Rare-Gas Cations and the Interaction of Rare Gases With Cations

Rare-gas species in the form of cations have also evoked considerable attention by chemists. Most important to this work are the three cations Rg_2H^+ (Rg=Ar, Kr or Xe) which were determined to have a linear centrosymmetric structure in rare-gas matrices[82] and in the gas phase.[83,84] A more detailed introduction to these species will be afforded later in this work, pertaining to the first successful attempts to prepare the mixed cations, $(RgHRg')^+$ (where $Rg \neq Rg'$) in

Chapter 4, and a density functional theory study designed to aid in the interpretation of experimental matrix-isolation infrared data in Chapter 5.

The effect of rare-gas atoms on the chemistry of hydrogen-containing cations was of major interest in these studies. In Chapter 6, density functional theory is used to probe the possibility of rare-gas catalyzed intramolecular proton transfer. The results of this study should be of paramount concern to mass spectrometrists or anyone utilizing rare gases and N_2 as *'inert'* atmospheres, within which studies of the chemistry of hydrogen-containing cations are conducted.

1.4 References to Chapter 1

1. Suzer, S.; Andrews, L. *J. Chem. Phys.* **1987**, *88*, 916.
2. Suzer, S.; Andrews, L. *J. Chem. Phys.* **1988**, *89*, 5347.
3. Szczepanski, J.; Roser, D.; Personette, W.; Eyring, M.; Pellow, R.; Vala, M. *J. Phys. Chem.* **1992**, *96*, 7876.
4. Zhang, X.K.; Parnis, J.M.; Lewars, E.G.; March, R.E. *Can. J. Chem.* **1997**, *75*, 276.
5. Fridgen, T.D.; Zhang, X.K.; Parnis, J.M.; March, R.E. manuscript in preparation.
6. Fridgen, T.D.; Parnis, J.M. *J. Chem. Phys.* **1998**, *109*, 2155.
7. Fridgen, T.D.; Parnis, J.M. *J. Phys. Chem.* **1997**, *101*, 5117.
8. Norman, I.; Porter, G. *Nature* **1954**, *174*, 508.
9. Whittle, E.; Dows, D.A.; Pimentel, G.C. *J. Chem. Phys.* **1954**, *22*, 1943.
10. For example a) Andrews, L.; Moskovits, Eds., *Chemistry and Physics of Matrix-Isolated Species*, **1989**, Elsevier, New York. b) Moskovits, M.; Ozin, G.A., Eds., *Cryochemistry*, **1976**, Wiley, New York.
11. a) Ball, D.W.; Kafafi, Z.H.; Fredin, L.; Hauge, R.H.; Margrave, J.L., Eds., *A Bibliography of Matrix Isolation Spectroscopy 1954-1985*, **1988**, Rice University Press, Houston. b) Oshsner, D.W.; Ball, D.W.; Kafafi, Z.H., Eds. *Bibliography of Matrix Isolation Spectroscopy 1985-1997*, **1998**, National Technical Information Service, Washington.
12. Norman, I.; Porter, G. *Proc. Roy. Soc. (London)* **1955**, *A230*, 399.
13. Dunkin, I.R., Chapter 8, in reference 10a.
14. a) Perutz, R.N, Chapter 9, in reference 10a. b) McGlinchey, M.J.; Skell, P.S., Chapters 4 and 5, in reference 10b.
15. a) Burdet, J.; Turner, J.J., Chapter 11, in reference 10b. b) Perutz, *Chem. Rev.* **1985**, *85*, 77. c) Perutz, R.N. *Chem. Rev.* **1985**, *85*, 97.

16. a) Moskovits, M., Chapter 3, in reference 10a. b) Hauge, R.H.; Margrave, J.L.; Kafafi, Z.H., Chapter 10, in reference 10a. c) Moskovits, M.; Ozin, G.A., chapter 8, in reference 10b.

17. Andrews, L., Chapter 2, in reference 10a.

18. a) Jacox, M.E., Chapter 4, in reference 10a. b) Knight, L.B.Jr., Chapter 7, in reference, 10a.

19. Jacox, M.E. *Rev. Chem. Intermed.* **1978**, *2*, 1.

20. Cradock, S.; Hinchcliff, A.J., *Matrix Isolation: A Technique for the Study of Reactive Inorganic Species*, 1st Ed., **1975**, Cambridge University Press, Cambridge.

21. Bondybey, V.E.; Brus, L.E. *Adv. Chem. Phys.* **1980**, *41*, 269.

22. Serrallach, A.; Meyer, R.; Günthard, Hs.H. *J. Mol. Spectrosc.* **1974**, *52*, 94.

23. Kunttu, H.M.; Seetula, J.A. *Chem. Phys.* **1994**, *189*, 273.

24. a) Reddington, R.L.; Milligan, D.E. *J. Chem. Phys.* **1962**, *37*, 2162. b) Milligan, D.E *J. Chem. Phys.* **1959**, *30*, 45.

25. a) Cugley, J.A.; Pullin, A.D.E. *Spectrochimica Acta* **1973**, *29A*, 1665. b) Milligan, D.E.; Hexter, R.M. *J. Chem. Phys.* **1961**, *34*, 1009.

26. Schallmoser, G.; Thoma, A.; Wurfel, B.E.; Bondybey, V.E. *Chem. Phys. Lett.* **1994**, *219*, 101.

27. Foner, S.N.; Cochran, E.L.; Bowers, V.A.; Jen, C.K. *J. Chem. Phys.* **1960**, *32*, 963.

28. Jacox, M.E. *J. Phys. Chem. Ref. Data* **1984**, *13*, 945.

29. Willard, J.E. *Cryogenics*, **1982**, 359.

30. Milligan, D.E.; Jacox, M.E. *J. Chem. Phys.* 1967, *47*, 278.

31. Jacox, M.E. *Chem. Phys.* **1976**, *12*, 51.

32. Szulejko, J.E.; McMahon, T.B. *J. Am. Chem. Soc.* **1993**, *115*, 7839.

33. Curtiss, L.A.; Raghavachari, K.; Trucks, G.W.; Pople, J.A. *J. Chem. Phys.* **1991**, *94*, 7221.

34. Curtiss, L.A.; Redfern, P.C.; Raghavachari, K.; Pople. J.A. *J. Chem. Phys.* **1998**, *109*, 42.

35. Scott, A.P.; Radom, L. *J. Phys. Chem.* **1996**, *100*, 16502.

36. MP2/6-311G** vibrational wavenumbers were calculated by E.G. Lewars, Department Of Chemistry, Trent University, Peterborough, ON.

37. Jursic, B.S. *J. Mol. Struct.* **1997**, *394*, 15.

38. Varetti, E.L.; Pimentel, G.C. *J. Chem. Phys.* **1971**, *55*, 3813.

39. Parnis, J.M.; Hoover, L.E.; Fridgen, T.D.; Lafleur, R.D. *J. Phys. Chem.* **1993**, *97*, 10708.

40. a) Milligan, D.E; Jacox, M.E. *J. Chem. Phys.* **1970**, *53*, 2034. b) Milligan, D.E; Jacox, M.E. *J. Chem. Phys.* **1971**, *55*, 2550.

41. Knight, L.B. Jr.; Bostick, J.M.; Woodward, R.W.; Steadman, J. *J. Chem. Phys.* **1983**, *78*, 6415.

42. Knight, L.B. Jr. *Acc. Chem. Res.* **1986**, *19*, 313.

43. Knight, L.B. Jr.; Steadman, J., *J. Chem. Phys.* **1984**, *80*, 1018.

44. Knight, L.B. Jr.; Kerr, K.; Villanueva, M.; McKinley, A.J.; Feller, D. *J. Chem. Phys.* **1992**, *97*, 5363.

45. Zhang, X.K., Ph.D. Thesis, Queen's University, Kingston, Ontario, 1993.

46. Forney, D.; Jakobi, M.; Maier, J.P. *J. Chem. Phys.* **1989**, *90*, 600.

47. Sabo, M.S.; Allison, J.; Gilbert, J.R.; Leroi, G.E. *Applied Spectroscopy*, **1991**, *45*,535.

48. Halasinski, T.M.; Godbout, J.T.; Allison, J.; Leroi, G.E. *J. Phys. Chem.* **1996**, *100*, 14865.

49. Godbout, J.T.; Halasinski, T.M.; Leroi, G.E.; Allison, J. *J. Phys. Chem.* **1996**, *100,* 2892.

50. Halasinski, T.M.; Godbout, J.T.; Allison, J.; Leroi, G.E. *J. Phys. Chem.* **1994**, *98*, 3930.

51. See for example a) Holmes, J.L. *Mass Spectrom. Rev.* **1989**, *8*, 513. and b) Schwarz, H. *Pure and Appl. Chem.* **1989**, *61*, 685.

52. Lyndsay, D.M.; Meyer, F.; Harbich, W. *Z. Phys.* **1989**, *12D*, 15.

53. Rivoal, J.C.; Grisolia, C.; Lignieres, J.; Kreisle, D.; Fayet, P.; Wöste, L. *Z. Phys.* **1989**, *12D*, 481.

54. Fedrigo, S.; Haslett, T.L.; Moskovits, M *J. Am. Chem. Soc.* **1996**, *118*, 5083.

55. Harbich, W.; Fedrigo, S.; Buttlet, J.; Lindsay, D.M. *Mat. Res. Soc. Symp. Proc.* **1991**, *206*, 369.

56. Wang, H.; Liu, Y.; Haouari, H.; Craig, R.; Lombardi, J.R.; Lindsay, D.M. *J. Phys. Chem.* **1997**, *101*, 7036.

57. Wang, H.; Hu, Z.; Haouri, H; Craig, R.; Liu, Y.; Lombardi, J.R.; Lindsay, D.M. *J. Chem. Phys.* **1997**, *106*, 8339.

58. a) Sülzle, D.; Weiske, T.; Schwarz, H. *Int. J. Mass Spectrom. Ion Processes* 1993, *125*, 75. b) Chen, H.; Holmes, J.L. *Int. J. Mass Spectrom. Ion Processes* **1994**, *133*, 111.

59. Hop, C.E.C.A.; Holmes, J.L.; Terlouw, J.K. *J. Am. Chem. Soc.* **1989**, *111*, 441.

60. For an excellent history leading up to the actual creation of xenon fluorides see Laszlo, P.; Schrobilgen, G.J. *Angew. Chem. Int. Ed. Eng.* **1988**, *27*, 479.

61. Yost, D.M.; Kaye, A.L. *J. Am. Chem. Soc.* **1933**, *55*, 3891.

62. Pauling, L. *J. Am. Chem. Soc.* **1933**, *55*, 1895.

63. Pauling, L. *Science* **1961**, *134*, 15.

64. Bartlett, N. *Proc. Chem. Soc.* **1962**, 218.

65. Hoppe, R.; Dähne W.; Mattauch, H.; Rödder, K. *Angew. Chem. Int. Ed. Eng.* **1962**, *1*, 599.

66. Claassen, H.H.; Selig, H.; Malm, J.G. *J. Am. Chem. Soc.* **1962**, *84*, 3593.

67. Malm. J.G.; Sheft, I.; Chernick, C.L. *J. Am. Chem. Soc.* **1963**, *85*, 110.

68. To date, a series of 44 papers on fluorination with XeF_2 by a Slovenian group of which the most recent is: Zupan, M.; Iskra, J.; Stavber, S. *J. Org. Chem.* **1998**, *63*, 878.

69. For example: Rundle, R.E. *J. Am. Chem. Soc.* **1963**, *85*, 112. For an excellent review of the physical, chemical and bonding properties see: Bartlett, N.; Sladky, F.O. *Comprehensive Inorganic Chemistry Vol.1*, **1973**, Pergamon Press: New York, Chapter 6.

70. LeBlond, R.D.; DesMarteau, D.D. *J. Chem. Soc., Chem. Commun.* **1974**, 555.

71. a) DesMarteau, D.D. *J. Am. Chem. Soc.* **1978**, *100*, 6270. b) DesMarteau, D.D.; LeBlond, R.D.; Hossain, S.F.; Nothe, D. *J. Am. Chem. Soc.* **1981**, *103*, 7734.

72. Schrobilgen, G.J. *J. Chem. Soc. Chem. Commun.* **1988**, 863.

73. Hovey, J.K.; McMahon, T.B. *J. Am. Chem. Soc.*, **1986**, *108*, 528.

74. Turbini, L.J.; Aikman, R.E.; Lagow, R.J. *J. Am. Chem. Soc.* **1979**, *101*, 5833.

75. Kötting, C.; Sander, W.; Breidung, J.; Thiel, W.; Senzlober, M.; Bürger, H. *J. Am. Chem. Soc.*, **1998**, *120*, 219.

76. Pettersson, M.; Lundell, J.; Räsänen, M. *J. Chem. Phys.* **1995**, *102*, 6423.

77. Pettersson, M.; Nieminen, J.; Khriachtchev, L.; Räsänen, M. *J. Chem. Phys.* **1997**, *107*, 8423.

78. Pettersson, M.; Lundell, J.; Khriachtchev, L.; Räsänen, M. *J. Chem. Phys.* **1998**, *109*, 618.

79. Pettersson, M.; Lundell, J.; Räsänen, M. *J. Chem. Phys.* **1995**, *103*, 205.

80. Feldman, V.I.; Sukhov, F.F. *Chem. Phys. Lett.* **1996**, *255*, 425.

81. Feldman, V.I.; Sukhov, F.F.; Orlov, A.Y. *Chem. Phys. Lett.* **1997**, *280*, 507.

82. Kunttu, H.; Seetula, J.; Räsänen, M.; Apkarian, V.A. *J. Chem. Phys.* **1992**, *96*, 5630.

83. Adams, N.G.; Bohme, D.K.; Ferguson, E.E. *J. Chem. Phys.* **1970**, *52*, 5101.

84. Hvistendahl, G.; Saastad, O.W.; Uggerud, E. *Int. J. Mass Spectrom. Ion Processes* **1990**, *98*, 167.

Chapter 2

Experimental And Theoretical Methods

2.1 Experimental Apparatus and Methods

2.1.1 The Vacuum System

Besides the infrared spectrometer, the main apparatus used in the experimental studies to be presented in some of the chapters to follow is illustrated in Figure 2.1. It shows the stainless steel vacuum shroud which also contains the electron-impact housing (EI), the cold window (CW), and the gas-handling manifold. The vacuum system consists of an Edwards model 63 silicon-based oil diffusion pump (DP) backed by an Edwards E2M2 2-stage mechanical roughing pump (MP). The pressure of the system was normally between 10^{-6} and 10^{-7} Torr at room temperature but, after the cold window had been cooled to between 15 and 16 K, the vacuum improved to 10^{-8} Torr as a result of the cryopumping capabilities of the

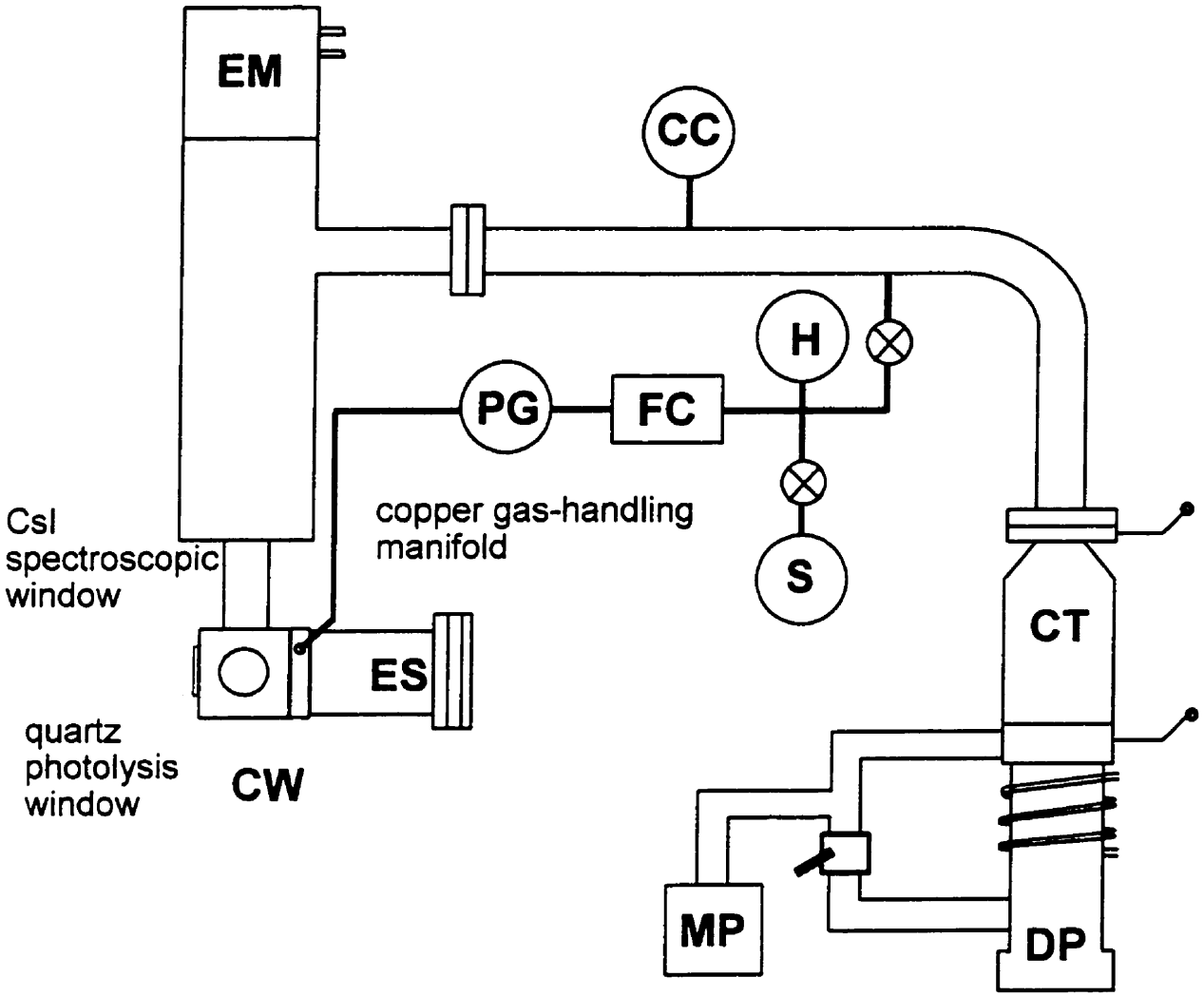

Figure 2.1. Schematic diagram of the stainless-steel matrix-isolation vacuum shroud utilized in the EBMI FT-infrared spectrosopic work. Symbols refer to the following components of the system: EM, displex expander module; CC, cold cathode pressure gauge; H, helicoil pressure gauge; PG, Penning pressure gauge; FC, mass flow controller; S, sample gas mixture; ES, electron source; CW, cold window or substrate made of CsI and is inside the vacuum shroud; CT liquid nitrogen cold trap; MP, mechanical roughing pump; and DP, diffusion pump.

cold window. Due to the strong cryopumping capabilities of a 15 K surface a liquid nitrogen trap was mounted on the top of the diffusion pump in order to stop diffusion of organic material and pump oil itself to the cold window from the diffusion pump. The pressure in the stainless steel vacuum shroud was monitored with an HPS model 941 cold cathode pressure gauge (CC).

Glass bulbs containing pre-mixed gas samples (S) were connected to the gas inlet system via a Cajon Ultra-torr fitting. During experiments, the pressure in the bulb was monitored by a 0-760 torr helicoil pressure gauge (H). The gas flow was controlled by an MKS Instruments Inc. mass-flow controller (FC) and monitored with a model 247-C 4-channel readout. Gas flows differed between experiments but were generally between 0.80 and 1.60 $cm^3\ min^{-1}$ of gas at standard temperature and pressure (298.15 K and 10^5 Pa). The pressure in the copper gas-handling line, between the mass-flow controller and the gas outlet, was monitored by an HPS model 917 Pirani sensor (PG).

2.1.2 Cryogenics and Temperature Control

The cryogenic refrigerator was an Air-Products Displex model CSW-202 closed-cycle helium refrigerator consisting of a compressor module and an expander module (EM in Fig. 2.1). It should be noted that in Fig. 2.1, only the head of the EM is shown and it actually extends down to the bottom of the vacuum shroud where the matrix substrate is mounted on to it.

In the compressor module (see Fig. 2.2), helium is compressed to 20 atm and cooled to ambient temperatures by a continuous flow of water. High-pressure

helium enters the head of the EM above a displacer and pressurizes a thermal regenerator below the head. While the pressure is rising, the charge above the displacer heats up due to the adiabatic nature of the compression; however, there is no appreciable rise in temperature in the regenerator end since it has such a high heat capacity. Once pressure equilibrium is attained, the displacer moves from the cold to the warm end of the expander module. During this cycle the gas from the warm end of the EM moves to the cold end through the thermal regenerator. Cooling of this transferred gas would result in a pressure decrease, however, 20 atm of pressure is maintained since the intake valve remains open, allowing high-pressure gas to enter the EM.

Once all of the gas has been displaced to the cold end (top of the dispacer stroke) the intake valve is closed and the exhaust valve is opened very slowly. During this part of the cycle the displacer is motionless and the gas at the low-temperature end of the EM undergoes expansion. The refrigeration that results is transferred to the heat load or the thermal regenerator. To complete the cycle, the displacer is moved from the warm to the cold end of the EM such that the residual expanded gas is transferred through the regenerator and out the exhaust valve carrying with it the heat exchanged from the heat load or thermal regenerator. The exhaust valve is closed and the cycle is repeated until the desired temperature is reached and while cryogenic temperatures are maintained.

The low-temperature gas expansion single-stage closed cycle was first developed by Gifford and McMahon.[1] The refrigeration unit used for the experimental part of this work is a two-stage closed-cycle refrigerator. Optimally,

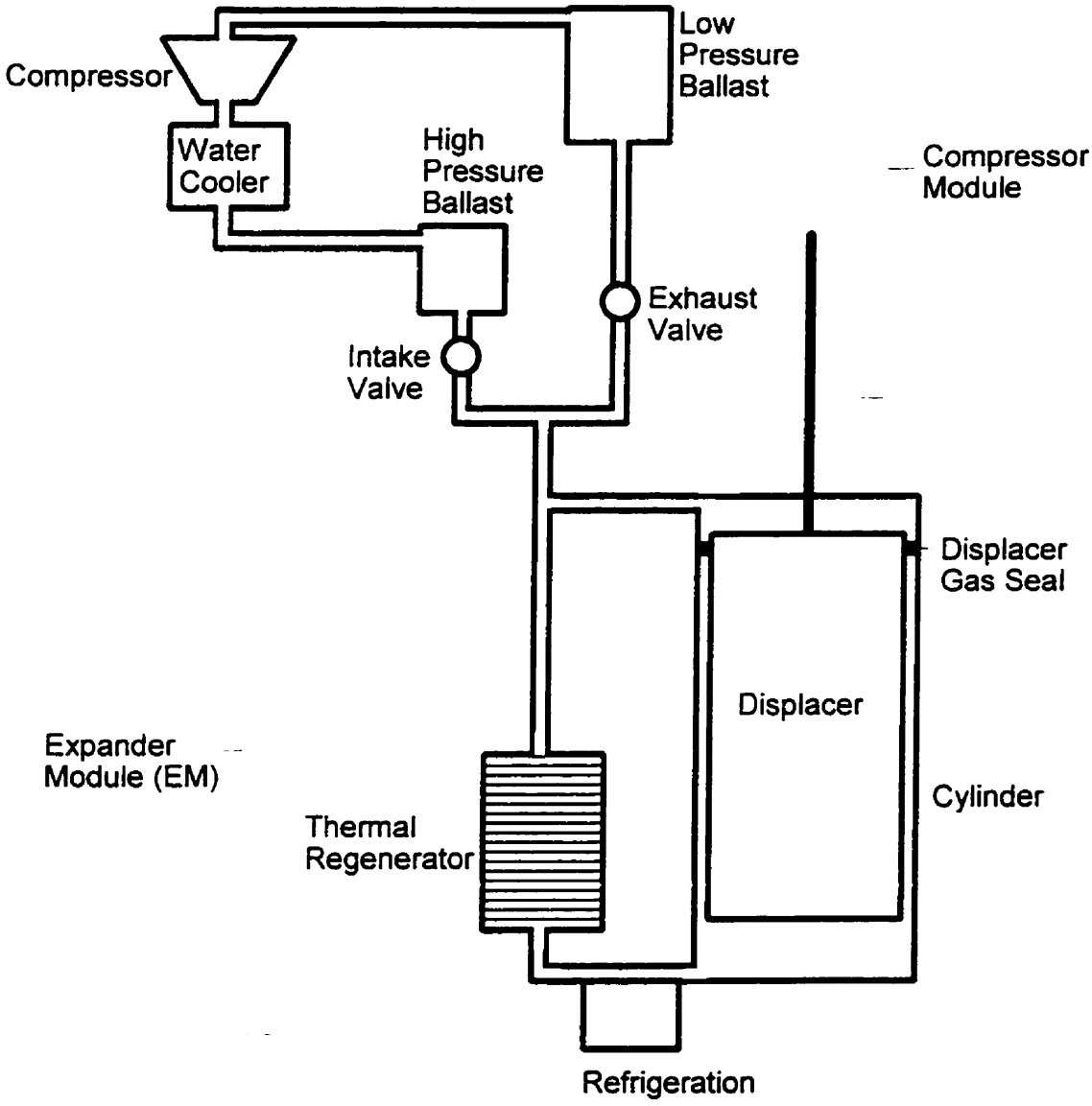

Figure 2.2. Schematic diagram of a single-stage low-temperature heat pump refrigerater.

cooling to 77 K is achieved at the first stage and 10 K can in principle be achieved at the second stage (matrix substrate). The actual refrigeration unit used has around 9000 hours of use and has trouble attaining temperatures much lower than 15.5 K.

The compressor and expander are connected by flexible helium transfer lines (intake and exhaust) permitting free rotation and movement of the displex expander module (D in Fig. 2.1) with respect to the compressor. The displex expander was mounted on two O-rings so that the cold window could be rotated through 360 degrees.

The surface onto which the matrix was formed (matrix substrate) was a CsI window which was mounted into a copper block. To allow efficient heat transfer and avoid cracking due to expansion and contraction during heating and cooling, the CsI cold window was mounted into the copper block using indium gaskets.

The temperature of the cold window was monitored by a Scientific Instrument Inc. model 9600-1 temperature controller which measures the temperature via a calibrated silicon diode temperature sensor mounted near the matrix substrate. When thermal annealing was done, the desired temperature was programmed into and controlled by the temperature controller which sends power to a heater mounted near the matrix substrate.

2.1.3 The Electron Source and Electron Bombardment Region

The electron bombardment matrix-isolation apparatus was modified from the design of Szczepanski *et al.*[2] The schematic diagram of the electron-impact

housing (EI in Fig. 2.1) is expanded and depicted in Figure 2.3. A 0.008 inch diameter thoriated-tungsten cathode was connected to a home-made DC power supply (8 V, 6 A) through pins A and B shown in the diagram. The filament current was normally maintained at 3.0 to 3.5 A. The cathode was also biased between -150 and -175 V (V_A) from ground. A steel plate with a 1 inch diameter mesh hole was grounded (V_C) and served as an electron extractor. A piece of zinc foil, labelled D in Fig. 2.3, was placed at the far side of the copper block holding the CsI cold window and care was taken to ensure that it was insulated from the rest of the system. This plate served as an anode and was biased between +125 and +150 V (V_D) from ground. This system produced electrons with between 275 and 300 eV of kinetic energy. The anode also served as a Faraday plate in order to monitor the number of electrons entering the ionization zone. Before the gas flow began the typical current measured was of the order of milliamperes. Compared to the 150 eV electrons used in previous experiments[3] it was determined that higher electron currents could be obtained employing voltages which produced ~300 eV electrons. This also resulted greater destruction of the precursor and a higher abundance of products (see below).

As shown in Fig. 2.3, a Teflon spout was inserted into the gas outlet line so that the gas sample could be sprayed directly onto the matrix substrate after crossing orthogonally the electron beam. This allowed the matrix substrate to be kept parallel to the electron beam which ensured that electrons did not directly impinge on the growing matrix and that photons emanating from the filament were not able to irradiate the matrix. This was a modification to the original design[3]

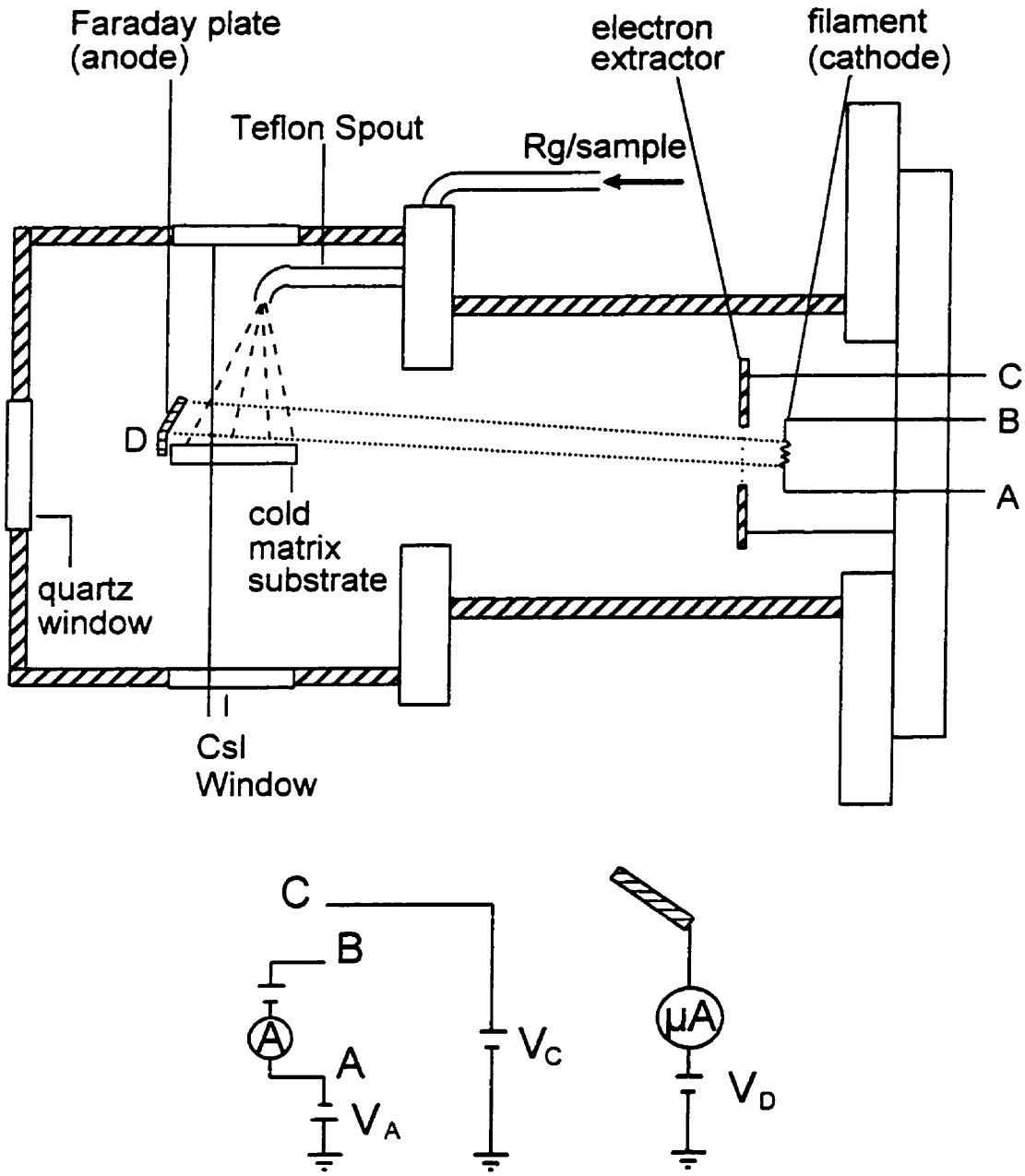

Figure 2.3. Schematic diagram of the electron source and electron-bombardment region of the EBMI apparatus showing the potentials on each electrode (see text) and the trajectory of the electron beam which crosses the gas flow on route to condensation on the cold matrix substrate.

which greatly enhanced product abundance. With this modification, it was observed that on straight deposition (*i.e.* no electron bombardment) at least twice as much gas was actually condensed onto the cold window. The greater amount of gas deposited is definitely a result of the Teflon tube; with the Teflon tube the gas line ends directly above the cold window (approximately 3 cm above). Without the Teflon tube present, the gas is much more dispersed before reaching the cold window and much of it would have been deposited onto the copper mounting block or the cold surfaces above it.

In Figure 2.4 (trace c) is shown the infrared spectrum recorded after 6 h of EBMI of a 1 in 400 mixture of CH_2Cl_2 in Ar from the work of Zhang[3] using the former apparatus which did not include the Teflon tube. Trace b was recorded after 8 hrs EBMI of the same 1 in 400 gas mixture except with the Teflon tube. Zhang's experiments were performed with 150 eV electrons whereas trace b was generated with 300 eV EBMI. It should be noted that the absorbance axis scale for trace c has been enlarged 10-fold, thus the production of CH_2Cl-Cl (isodichloromethane) is appreciable enhanced with the optimized experiment. The enhancement of isolated product is due to a combination of a number of factors. With the Teflon tube the gas mixture flows directly above the matrix substrate. The use of higher energy electrons is expected to increase the number of electrons crossing the path of the gas flow directly above the matrix substrate. The combination of more gas and more electrons directly above the matrix substrate results in a greater destruction of the precursor and much more product formed in this region which are then condensed onto the cold window. Furthermore, with the Teflon tube present, the

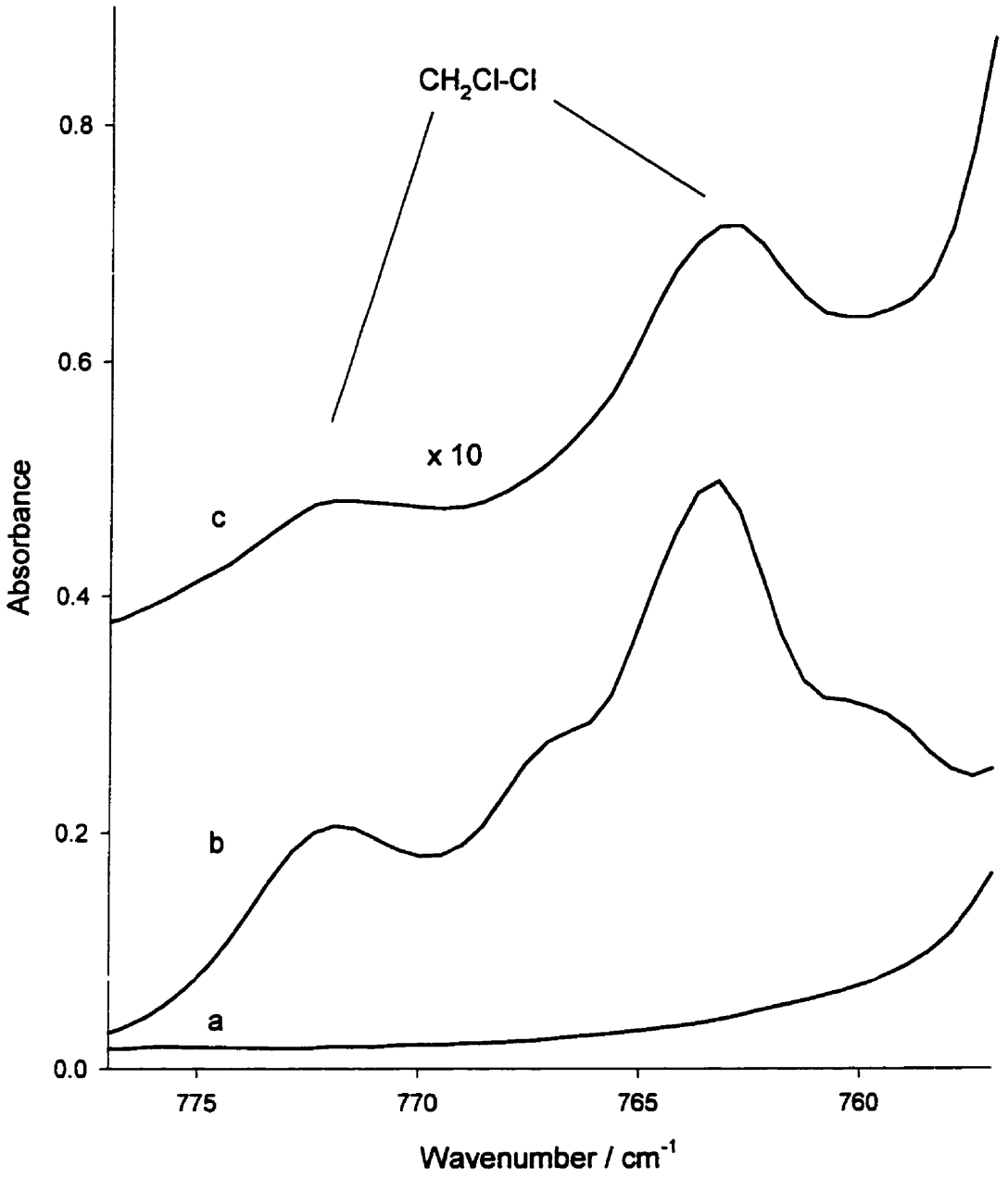

Figure 2.4. Portion of the infrared spectra recorded a) after 8 h straight deposition of a 1 in 400 CH_2Cl_2 in Ar mixture at a flow rate of 1.6 sccm and b) after 8 h EBMI of the same mixture and flow rate. Spectrum c) has been expanded by 10 times and was recorded after 6 h EBMI of a 1 in 400 mixture of CH_2Cl_2 in Ar at a flow rate of 0.85 sccm (spectrum c is adapted from Zhang's work, reference 3). See text for further details of the experiments.

matrix substrate could be oriented so that during EBMI the photons and electrons emanating from the filament were not able to impinge upon the growing matrix. Isodichloromethane, the species responsible for the bands shown in Fig. 2.4, is quite sensitive to visible light (see chapter 3 for further details of EBMI of dichloromethane) and with the shading of the matrix from the light produced by the filament it is expected that much less of it is destroyed photolytically.

2.1.4 Infrared Spectrometer and Spectroscopic Windows

Infrared spectra were acquired with a Bomem Michelson, MB 102 Fourier Transform Infrared Spectrometer. To eliminate interference and complication of the spectrum due to moisture in the air, the infrared beam path was purged with dry air at a flow rate of 14.1 L min^{-1} from a Balston Filter Products, Type 75-10 Compressed Air Dryer. Typically 500 scans at 1 cm^{-1} resolution were obtained and averaged for each infrared spectrum.

Before each experiment, the spectroscopic windows and CsI matrix substrate were cleaned with methanol and dichloromethane. After a suitable period of pumping and cooling for one hour to reach ~15 K, a background or reference spectrum of the spectroscopic and substrate windows was obtained. Each spectrum obtained afterwards within a given experiment had the reference spectrum automatically subtracted from it.

The matrix substrate was a CsI crystal as were the two spectroscopic windows. CsI was used since it is transparent to radiation in the region 10 000 cm^{-1} to 200 cm^{-1}.

2.1.5 Light Source for Irradiation

The irradiation light source used in these experiments was an Oriel Corp. Model 66021 universal arc lamp housing with a xenon arc lamp. The lamp was powered by an Oriel Corp. Model 68820 1000 Watt universal arc lamp power supply operated at 450 W. The xenon lamp gives off visible and UV light but the irradiance begins to fall off drastically at wavelengths lower than 230 nm.

Various cut-off filters were used to allow irradiation with broad-band light with wavelengths >550 nm, >345 nm and >300 nm. Irradiation of the deposited matrix was done by rotating the expansion module and, therefore, the matrix substrate, by 90 degrees to face a quartz window which has good transmission of radiation between 200 and 2500 nm.

2.1.6 Gas Mixture Preparation and Chemical Specifications

Gas mixture preparation was carried out in a 1/4" stainless-steel vacuum line. Vacuum in this line was attained as described above for the EBMI apparatus. Typically, the sample preparation line, large sample bulb, and stainless-steel lines from the gas cylinders to the preparation line were evacuated to 10^{-7} torr. Precursors used in all experiments were liquids at ambient temperature and pressure which necessitated their degassing. Numerous 'freeze-pump-thaw' cycles were performed by first freezing the sample in a small glass bulb submerged in liquid nitrogen. While frozen, the bulb was exposed to the vacuum so that the gases above the sample were drawn off. The bulb was then sealed and the liquid

was allowed to thaw. This cycle was repeated until the pressure above the frozen sample was less than 10^{-6} torr.

Once the liquid was degassed, the sample preparation line and sample bulb were subjected to the vapours of the liquid precursor in order to condition the line. These vapours were evacuated and a sample of the vapour was transferred to the large sample bulb. The pressure in the bulb was then increased with matrix gas to a point which corresponded to the desired precursor/matrix gas ratio was reached. For example, 2.00 torr of precursor diluted to 800 torr of matrix gas comprised a 1 in 400 mixture of precursor to matrix gas. The gases listed in Table 2.1 were used without further purification.

Table 2.1. Chemicals used for the experiments reported in this work as well as their grade and supplier.

Chemical	Grade	Supplier
Ar	Prepurified	Matheson
Kr	Research Purity	Matheson
Xe	Research Grade	Praxair
N_2	Prepurified	Matheson
CO	CP-Grade	Matheson
CH_3OH	99.9 % spectrophotometric grade	Aldrich
CD_3OD	99.95+ atom % D	Aldrich
$^{13}CH_3OH$	99 atom % ^{13}C	Aldrich
CH_2Cl_2	99.9+ % HPLC grade	Aldrich
CD_2Cl_2	99.95 atom % D	Aldrich

2.2 Theoretical Methods

The aim of the theoretical studies in the chapters to follow included calculating the structures and vibrational spectra of species containing rare-gas atoms Ar, Kr and/or Xe. These species were complexes such as the methanol radical cation complexed with argon or actual bound species such as Ar_2H^+. Some of the calculations involved structures with molecular formulas Xe_4H^+ and $Ar_{14}H^+$ which include 216 and 252 electrons, respectively. The theoretical methods used, needed to be able to handle and complete these calculations with a large number or electrons in a reasonable period of time and, of course, give acceptable results which favourably compare with other theoretical calculations and/or experimental data. Similarly, it would be advantageous to use similar theories and basis sets for all calculations to compare effects of the different rare gases. Density functional theory was chosen simply because it gives "MP2-quality results at a fraction of the time."[4a]

2.2.1 Basis Sets

All-electron Gaussian basis sets of sufficiently high quality for the studies presented in following chapters are not readily available for krypton and xenon. The SPARTAN 5.0[5] set of programs, however, makes use of numerical basis sets for which all elements, H through Xe, are supported. There are advantages and disadvantages to using numerical basis sets rather than the more common Gaussian basis sets. First of all, in order to accurately reflect the shape of the

atomic orbital one must use a linear combination or contraction of simple Gaussian functions. For example, the popular 3-21G and 6-31G basis sets represent the 1s orbital with 3 and 6 simple Gaussian functions, respectively. With these basis sets the valence shell is doubly split (double-ζ) and the first sub-set of the doubly split valence shell is contracted with 2 and 3 simple Gaussian functions, respectively. The number of Gaussian functions or contractions is called the contraction number and the computational cost of calculating the two-electron integrals increases as the fourth power of the contraction number.[6] In contrast, the numerical basis sets are approximations to atoms in molecular environments and need not be contracted. They are defined at selected points, meaning that one is working with a table of function values and it is assumed that the function varies linearly or quadratically between the selected points called a grid. The two-electron integrals must be calculated numerically (rather than analytically as is the case for Gaussian basis sets). Since these numerical basis sets are zeroth order approximations to atoms in molecular orbitals they need not be contracted like the Gaussian basis sets which results in an increase in computational speed. However, with the advantage of speed comes a loss of accuracy due to round-off errors during the numerical integration. One can attempt to diminish these round-off errors by utilizing a finer grid which simply means selecting more points to define the basis set with some loss of computational expediency.

2.2.2 Computational Methods

Hartree-Fock (HF) theory yields values which, in general, do not compare

favourably with experimental results with respect to post-Hartree-Fock theories. This can be attributed to the fact that it does not take into account the correlation energy or that it does not adequately account for the coulombic interaction between pairs of electrons which is especially noticeable for electron pairs with antiparallel spins.[7] Methods such as Møller-Plesset perturbation theory (MPPT) move beyond the single configurational method of HF theory, however, the consideration of multiple configurations results in the need for very expensive computer resources.[8] Density functional theory (DFT) is, as are the methods mentioned above, based on the Schrödinger equation and, like MPPT theory, takes into account electron correlation. However, DFT does not calculate a wavefunction and is based on the notion that the energy of an electronic system can be expressed in terms of an electron density.[9] DFT is better than HF theory in that the incorrect treatment of correlation, inherent in HF, is corrected. These corrections, however, are approximate and are not complete. The computational expedience of DFT and the MP2-quality results make it a desirable choice for the calculations reported in this work.

2.2.3 Computational Details

Before summarizing the density functional methods utilized in chapters 5 and 6 of this work a few definitions will be given. For excellent introductions to density functional theory and the calculus involved the reader is directed to Bartolotti and Flurchick,[10] Ziegler,[9] as well as Baerends and Gritsenko.[11] First of all, a functional maps a function into a number. An arbitrary functional is given by,

$$\Omega = \int f(r) d\tau \qquad \textbf{(2.1)}$$

where $f(r)$ is the integrand, r is the spatial coordinates and $d\tau$ is the volume element of integration. Generally $f(r)$ has a dependence on one or more well-defined functions. For instance, if

$$f(r) = \rho(r) \qquad \textbf{(2.2)}$$

where $\rho(r)$ is some function (say the electron density in this context) then Ω is a functional of $\rho(r)$. A functional whose integrand is only a simple function of ρ, such as Eq. 2.2 is called a *local functional* of ρ. Functionals whose integrand contains gradients (or higher derivatives) of ρ, such as Eq. 2.3 where ∇ is the gradient operator

$$f(r) = \frac{\nabla\rho(r)\cdot\nabla\rho(r)}{\rho(r)}, \qquad \textbf{(2.3)}$$

are called gradient-corrected functionals of ρ.[10] In general, the local density approximation gives very large errors which are associated with poor treatment of exchange and correlation energies. Much work has gone into the development of gradient-corrected exchange and correlation functionals and many of each are

available. Similarly, much work has been done assessing the different combinations of gradient-corrected exchange and correlation functionals.[12,13]

In the SPARTAN 5.0[5] suite of programs there is only one gradient-corrected spin density approximation DFT method. This method employes Becke's gradient-corrected exchange functional[14] in conjunction with Perdew's 1986 gradient-corrected correlation functional[15] which is from this point on denoted as the BP86 method. Similarly, SPARTAN 5.0[5] has no choice of basis set for DFT calculations. The only one supported is a numerical basis set with polarization functions added to all atoms, DN**, which is of comparable size to the 6-31G** Gaussian basis set but, it has been repeatedly observed to give results as good as the triple-ζ Gaussian basis set 6-311G**.[16] These BP86/DN** calculations were performed using the SPARTAN 5.0[5] suite of programs on an Indy™ Silicon Graphics Instruments (SGI) workstation. This computer, stationed at Trent University, utilized a 150 MHz MIPS R4400 Ver. 5.00 central processing unit (CPU) and had 96 MB of memory.

These calculations were compared with calculations from other researchers and were supported with DFT calculations performed using other methods. Other DFT methods which were used for this work were utilizing the BP86 with an augmented Gaussian double-ζ split-valence basis set with polarization functions added to all atoms, DZVP. These calculations were performed at the University of Montreal using the DeMon suite of programs.[17] The computer used was a Challenger SGI workstation with eight 100 MHz IP19 processors and an MIPS R4400 Ver. 4.00 CPU with 500 MB of memory. Similarly, DFT calculations utilizing the BP86 method and the two hybrid methods, B3LYP and B3PW91, were used in

conjunction with the Gaussian 6-31G*, 6-311G** and 6-311+G** basis sets in order to verify the BP86/DN** calculations. In these hybrid methods, B3 is the three-parameter exchange functional by Becke[18] which combines Becke's exchange functional and HF exchange. The corrections due to correlation are provided by the gradient-corrected correlation functionals of Lee, Yang and Parr[19] (LYP) and of Perdew and Wang[20] (PW91). These calculations were done using the GAUSSIAN 94W suite of programs[21] on a 200 MHz Pentium I personal computer with 32 MB of Ram.

2.3 References to Chapter 2

1. McMahon, H.O.; Gifford, W.E. Adv. Cryogenic Engineering 1960, 5, 354.
2. Szczepanski, J.; Roser, D.; Personette, W.; Eyring, M.; Pellow, R.; Vala, M. *J. Phys. Chem.* **1992**, *96*, 7876.
3. Zhang, X.K. Ph.D. Thesis, Queen's University, Kingston, Ontario, 1993.
4. Shusterman, A. Professor of Chemistry, Reed College, Portland, OR, personal communication, September 20th, 1998.
5. Spartan Version 5.0, Wavefunction, Inc., 18401 Von Karman Avenue, Suite 370, Irvine, CA 92612 USA.
6. Huang, W. Director of Support, Wavefunction Inc., personal communication, September 10, 1998.
7. Pilar F. *Elementary Quantum Chemistry 2nd Edition*, **1990**, McGraw-Hill Inc., Toronto.
8. Simons, J.; Nichols, J. *Quantum Mechanics in Chemistry*, **1997**, Oxford University Press, New York.
9. Ziegler, T. *Chem. Rev.* **1991**, *91*, 651.
10. Bartolotti, L.J.; Flurchick, K., *An Introduction to Density Functional Theory*, Chapter 4 in Lipkowitz, K.B.; Boyd, D.B., *Reviews in Computational Chemistry*, Vol. 7., **1996**, VCH Publishers, New York.
11. Baerends, E.J.; Gritsenko, O.V. *J. Phys. Chem.* **1992**, *101*, 5383.
12. See the many works by Branco Jursic for example, Jursic, B.S. *Chem. Phys. Lett.* **1998**, *284*, 281 and references therein.
13. Curtiss, L.A.; Redfern, P.C.; Raghavachari, K.; Pople, J.A. *J. Chem. Phys.* **1998**, *109*, 42.
14. Becke, A.D. *Phys. Rev.* **1988**, *A38*, 3098.
15. Perdew, J.P. *Phys. Rev.* **1986**, *B33*, 8822.

16. Hehre, W.J.; Lou L. Ed. *A Guide to Density Functional Calculations in SPARTAN*, **1997**, Wavefunction Inc., Irvine.

17. a) St-Amant, A.; Salahub, D.R., *Chem. Phys Lett.* **1990**, *169*, 387. b) St-Amant, A., Ph.D. Thesis, University of Montreal, Montreal, Quebec, 1992. c) deMon-KS version 3.4, Casida, M.E.; Daul, C.; Goursot, A.; Koester, A.; Pettersson, L.; Proynov, E.; St-Amant, A.; Salahub, D.R.; Duarte, H.; Godbout, D.; Guan, J.; Jamorski, C.; Leboeuf, M.; Malkin, V.; Malkina, O.; Sim, F.; Vela F., deMon Software, 1996.

18. Becke A.D. *J. Chem. Phys.* **1993** *98*, 5648.

19. Lee, C.; Yang, W.; Parr, R.G. *Phys. Rev.* **1988**, *B37*, 785.

20. Perdew, J. P.; Wang, Y. *Phys. Rev.* **1992**, *B45*, 13244.

21. Gaussian 94, Revision E.1, Frisch, M.J.; Trucks, G.W.; Schlegel, H.B.; Gill, P.M.W.; Johnson, B.G.; Robb, M.A.; Cheeseman, J.R.; Keith, T.; Petersson, G.A.; Montgomery, J.A.; Raghavachari, K.; Al-Laham, M.A.; Zakrzewski, V.G.; Ortiz, J.V.; Foresman, J.B.; Cioslowski, J.; Stefanov, B.B.; Nanayakkara, A.; Challacombe, M.; Peng, C.Y.; Ayala, P.Y.; Chen, W.; Wong, M.W.; Andres, J.L.; Replogle, E.S.; Gomperts, R.; Martin, R.L.; Fox, D.J.; Binkley, J.S.; Defrees, D.J.; Baker, J.; Stewart, J.P.; Head-Gordon, M.; Gonzalez, C.; Pople, J.A., Gaussian Inc., Pittsburgh PA, 1995.

Chapter 3

A Matrix-Isolation FTIR Spectroscopic Study of the Products of Gas-Phase Electron Bombardment of Rare Gases Doped With Dichloromethane or Oxalyl Chloride

3.1 Scope of Chapter 3

The purpose of this chapter is to attempt to give an understanding of the processes occurring during electron bombardment matrix-isolation experiments. For example, as discussed in chapter 1, some cations (such as the methanol radical cation) were not observed in argon matrices by electron spin resonance spectroscopy while they were observed in neon matrices. This discrepancy between matrix host material is observed despite submitting the samples to the

same ionization conditions before matrix isolation. Electron bombardment and subsequent matrix isolation (EBMI) of oxalyl chloride, $(COCl)_2$, diluted in argon or krypton similarly results in no features assignable to ionic species in the infrared spectrum. However, in the infrared spectrum recorded after a period of EBMI of dichloromethane diluted in argon, both cationic and anionic species as well as neutrals are observed. In this chapter, possible reasons as to "why some ions and not others" will be presented. Also, the processes of ionization (i.e. Penning or charge exchange), quenching and neutralization will be discussed in this chapter. The importance of photochemical processes which may be induced by high-energy fluorescence from excited rare-gas atoms will also be discussed.

3.2 Experimental Section

The apparatus employed in these electron bombardment matrix-isolation studies is described in detail in chapter 2. Briefly, the Ar/precursor mixture, where precursor was either oxalyl chloride or dichloromethane, was typically 400/1 by mole fraction. This mixture crossed perpendicular to a ~300 eV electron beam directly above the 15 K CsI substrate, after which it was immediately condensed. After EBMI for a period of time specified below, infrared spectra were recorded at 1 cm^{-1} resolution and were compared with spectra recorded under the same circumstances except with the electron beam turned off.

3.3 Dichloromethane

3.3.1 Introduction

The chemistry of the dichloromethane radical cation has received some attention in the past and is introduced here. The 70 eV electron impact (EI) mass spectrum of dichloromethane[1] shows peaks associated with the molecular ion $CH_2Cl_2^{+\bullet}$ (60), $CHCl_2^+$ (10), $CCl_2^{+\bullet}$ (2), $Cl_2^{+\bullet}$ (0.1), CH_2Cl^+ (100) and $HCl^{+\bullet}$ (10) where the relative intensities are in parentheses. Make note that the base peak is due to CH_2Cl^+.

From the mass-analysed ion kinetic energy spectra of $CH_2Br_2^{+\bullet}$ and $CH_2I_2^{+\bullet}$ it was determined that there was a considerable release of kinetic energy on collision-induced dissociation of $CH_2Br_2^{+\bullet}$ (317 meV) and $CH_2I_2^{+\bullet}$ (788 meV) to form $Br_2^{+\bullet}$ and $I_2^{+\bullet}$, respectively, and where the kinetic energy releases (KER) are in parentheses.[1,2] The large KER's rules out simple bond cleavage and are consistent with a rearrangement of the molecular ion before decomposition rather than decomposing via a concerted mechanism. The isomeric ion was proposed to have the structure $CH_2X\text{-}X^{+\bullet}$ (X=halogen) with a divalent chlorine atom. In experiments with $CH_2Cl_2^{+\bullet}$, the peak at *m/z* 70 ($Cl_2^{+\bullet}$) was too weak to obtain reliable kinetic energy release data and this is consistent with the fact that the energy requirement for loss of CH_2 from $CH_2Cl_2^{+\bullet}$ to form the dichlorine radical cation is higher than that for the decomposition reaction of the bromo- and iodo-dihalomethane cations.[1,2]

In chemical ionization (CI) experiments of Zhang,[3] the dichloromethane radical cation was prepared by submitting a 1 in 400 mixture of dichloromethane in

Ar at a pressure of 10^{-5} torr to 50 eV electron bombardment (much like in the EBMI experiments). The mass scan revealed peaks due to the molecular ion $CH_2Cl_2^{+\bullet}$ (65), $CHCl_2^+$ (2.7), CH_2Cl^+ (base peak, 100) and $CHCl^{+\bullet}$ (8.2) where, again, the relative intensities are in parentheses. The absence of *m/z* 70 can be explained on thermodynamic grounds, that there is simply not enough energy on charge exchange with $Ar^{+\bullet}$ to produce $Cl_2^{+\bullet}$. On the other hand, it is interesting to note that there was no $CCl_2^{+\bullet}$ observed at *m/z* 82 even though it is accessible thermodynamically and it was observed in other mass spectrometric experiments.[1]

Zhang found that a major product of EBMI experiments of dihalomethanes doped in argon[3] were the isodihalomethanes, CH_2Cl-Cl, the neutral counterpart of the cation with a divalent chlorine atom. It was concluded from Zhang's work that Penning ionization and resonant emission from excited states of argon may be significant contributors to the formation of these species, a point which will be scrutinized in this chapter.

These divalent halide species have also been formed by vacuum UV photolysis of dihalomethane-containing argon matrices.[4] A careful analysis of the observed and calculated infrared spectra revealed that the isodihalomethanes are best described by the following resonance structures,

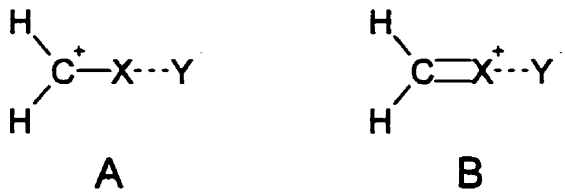

The calculated spectra predict more intense C-H stretching vibrations than regular

dichloromethane which are certainly most likely due to a more polar molecule. Structure A is also important because the CH_2 wagging vibration occurs at substantially higher energy in the isodihalomethanes than in CH_2Cl which suggests a stiffer C-Cl bond and partial double bond character in the former.

In this section the results of EBMI experiments performed on mixtures of dichloromethane in argon, krypton or xenon will be discussed.

3.3.2 Results

3.3.2.1 CH_2Cl_2 or CD_2Cl_2 in Argon

The infrared spectrum obtained after exposing a 1 in 400 mixture of CH_2Cl_2 in Ar to electron bombardment and subsequent matrix isolation for 8 h at a gas flow rate of 1.6 sccm (standard cubic centimetres per minute) showed that about 38% of the precursor was destroyed when compared to the infrared spectrum recorded with the electron beam off. As well, numerous new features were observed (see Table 1 for a summary of assigned bands). When the ratio of CH_2Cl_2 to Ar was changed to 1 in 600, the destruction of precursor increased to 46%. Products due to fragmentation of CH_2Cl_2 were relatively more abundant in the 1 in 600 experiment, while those which can be considered as isomerization products and molecular ions of the precursor were relatively less abundant. It is assumed at this point that the increase in relative intensity of fragmentation products and decrease in intensity of intact molecular products results from the decrease in concentration of the precursor which acts as a quenching agent. The effect of quenching is also observed in the methanol experiments (chapter 4) and is discussed in much more

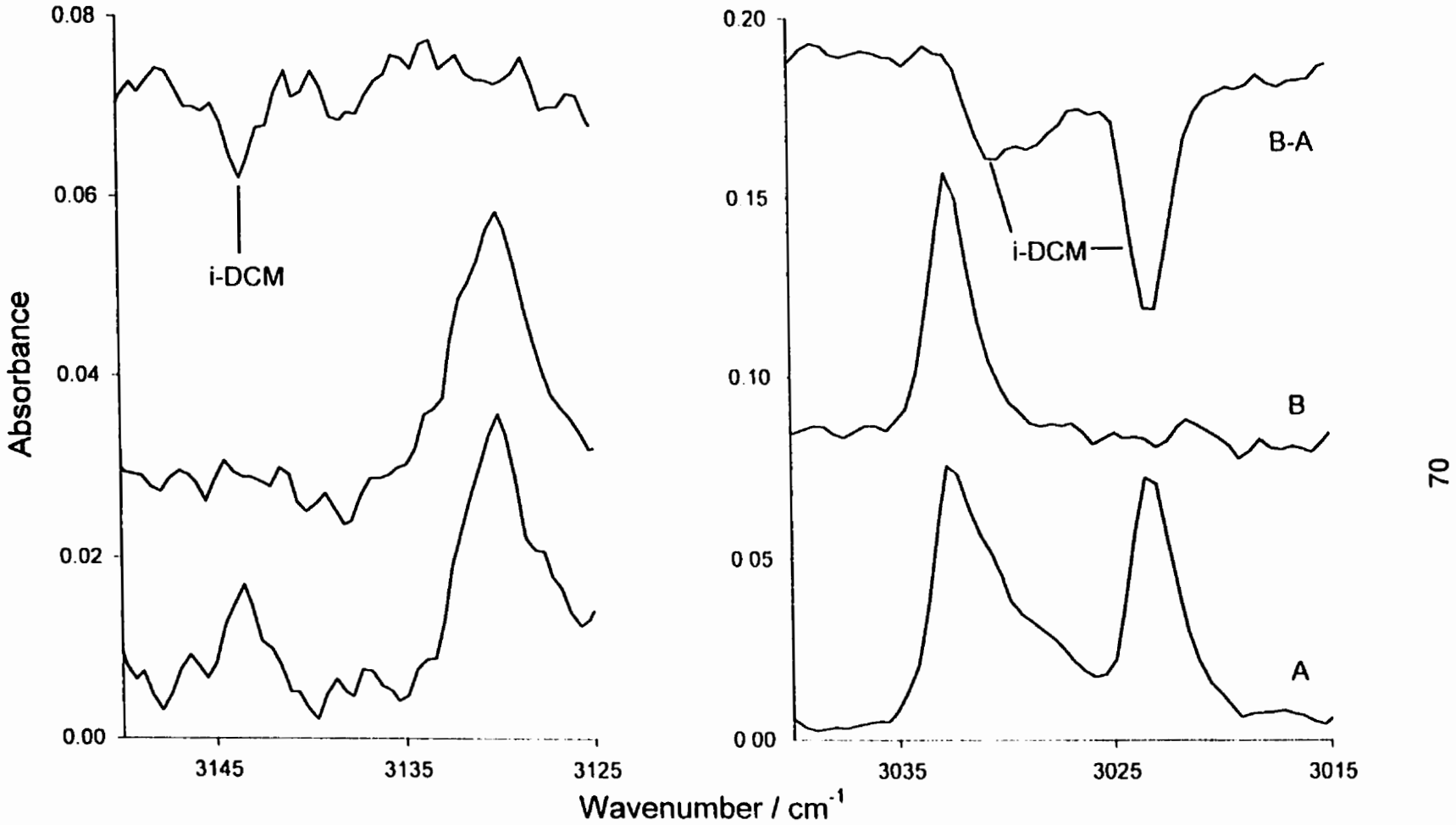

Figure 3.1. Portions of the FT-infrared spectra recorded A) after 8 h EBMI of a 1 in 400 mixture of CH_2Cl_2 in Ar and B) following 5 min irradiation with red light (>550 nm). The top trace (B-A) is the difference spectrum obtained by subtracting the EBMI spectrum (A) from the irradiation spectrum. i-DCM denotes isodichloromethane.

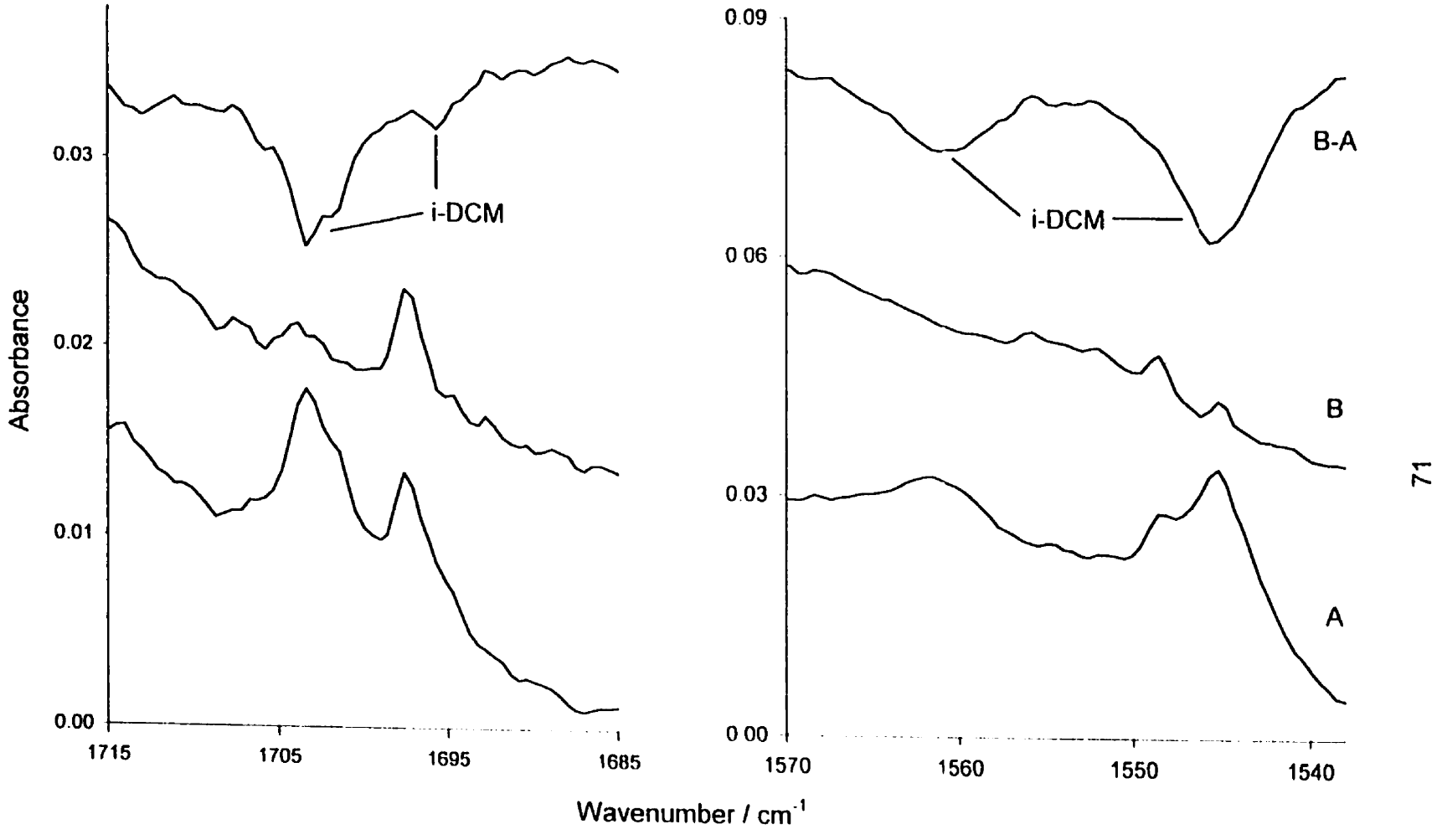

Figure 3.1. (continued)

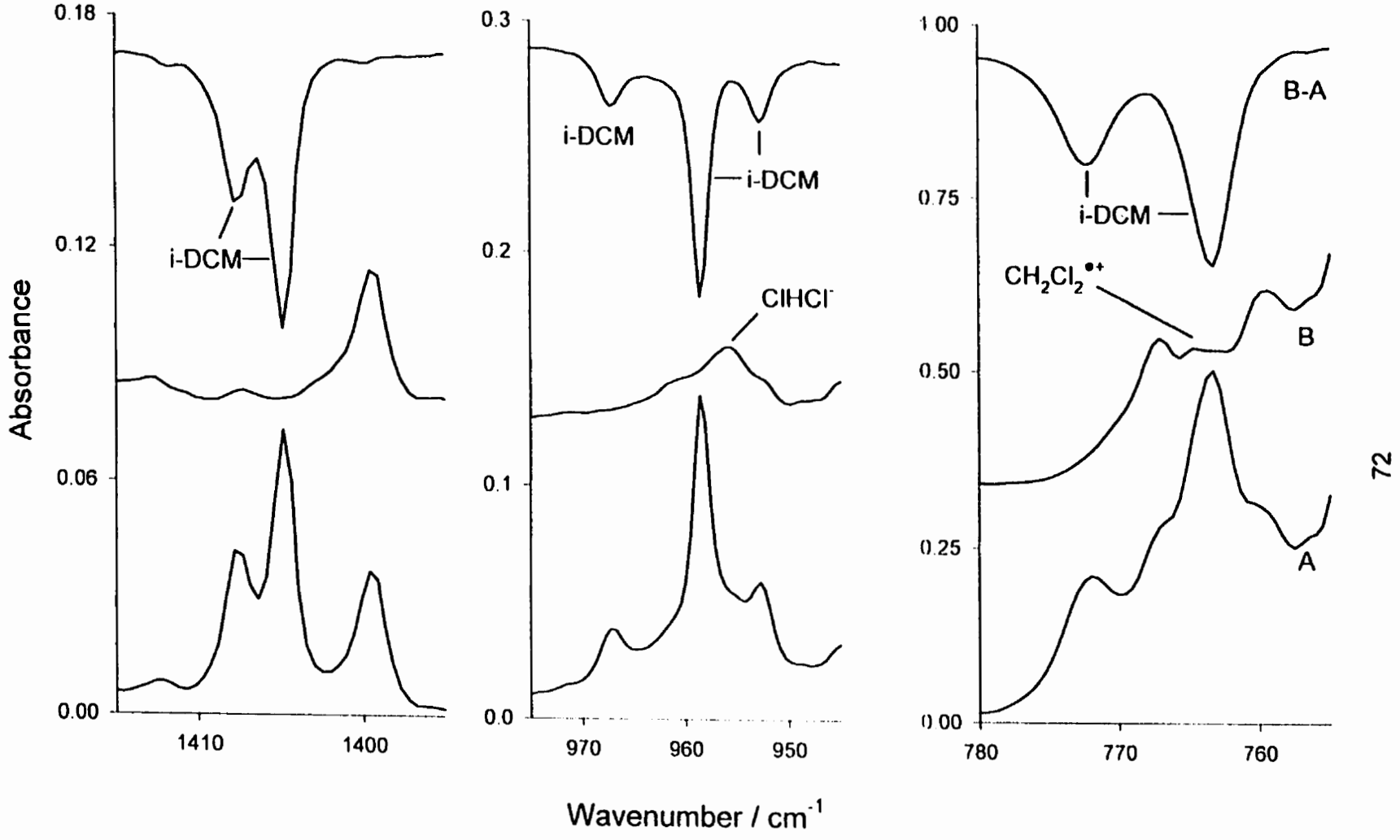

Figure 3.1. (continued)

detail in section 3.4.

Among the more intense new features were ones in excellent agreement with those previously assigned to isodichloromethane CH_2Cl-Cl by Maier *et al.*[4] All of these features decreased in intensity on exposure of the matrix to irradiation with wavelength greater than 550 nm for 5 min as can be seen in Fig. 3.1 (see also Table 3.1). Similarly, when CD_2Cl_2 was used in place of its H-isotopomer, CD_2Cl-Cl was observed and displayed the same behaviour upon exposure to red light filtered from the Xenon arc lamp. After irradiation with red light in both the CH_2Cl_2 and CD_2Cl_2 experiments, only a slight increase in intensity of the precursor bands was observed which may correspond to some back isomerization of isodichloromethane to dichloromethane.

A triplet at 1195.4, 1192.7 and 1190.1 cm^{-1} is assigned to $CCl_2^{+\bullet}$ in excellent agreement with previous studies,[5] however, after irradiation for approximately 1 h with 550 nm filter an intensity decrease was observed within this triplet. The maximum decrease was centred at 1193.2 cm^{-1}. The remaining triplet had a 9:6:1 intensity ratio and did not show additional sensitivity on irradiation with light as low as 200 nm. The band at 1193.2 cm^{-1} agrees very well with that previously assigned to the parent ion $CH_2Cl_2^{+\bullet}$.[6]

In the CD_2Cl_2 experiments, the same triplet due to $CCl_2^{+\bullet}$ is observed along with a higher energy absorption at 1197.0 cm^{-1}. The disappearance of this high energy band and a decrease in intensity at 1195.1 cm^{-1} after 1 h irradiation with the 550 nm cut-off filter revealed the 9:6:1 intensity ratio of the 1195.3, 1192.7 and 1190.1 cm^{-1} bands associated with $CCl_2^{+\bullet}$. The absence of intensity depletion at

Table 3.1. FT-Infrared observed species following electron bombardment and subsequent matrix isolation of 1 in 400 CH_2Cl_2 (or CD_2Cl_2) in Ar, Kr and Xe.

Identity	CH_2Cl_2 in Ar / cm^{-1}	CH_2Cl_2 in Kr / cm^{-1}	CH_2Cl_2 in Xe / cm^{-1}	Identity	CD_2Cl_2 in Ar / cm^{-1}	CD_2Cl_2 in Kr / cm^{-1}	CD_2Cl_2 in Xe / cm^{-1}
CH_2Cl-Cl	3143.6			**CD_2Cl-Cl**			
	3030.5				2226.1		
	3023.3	3019.2			2220.6	2220.0	2212.1
	1703.2						
	1695.7						
	1561.2				1224.3		
	1545.1	1566.1			1211.8		
	1407.7	1405.2	1402.1		1086.8	1088.4	1081.7
	1404.9				1083.5	1084.6	
	967.1				891.3		
	958.4	965.0			886.0	888.9	
	952.6				879.7	881.7	
					874.8		
	772.3	775.4	776.6		610.2	612.4	613.2
	763.4				603.5		
$CH_2Cl_2^{+\bullet}$	1193.2						
	764.5						
$CHCl_2^{+}$	3032.5						
	1290.9	1282.5					
	1050.0						
	1048.0						
	1044.6	1037.7					
	1041.8	1034.9					
	1039.0						
	845.3						
	841.3						
	837.9						
$CHCl_2^{\bullet}$	1224.8	1221.5					
	1218.6						
	901.4						
	898.0	NR					
	897.1	895.8					
	894.2	893.5					
$CCl_2^{+\bullet}$	1195.4	1196.9		**$CCl_2^{+\bullet}$**	1195.3	1196.6	
	1192.7	1194.0			1192.7	1194.2	
	1190.1	1190.4			1190.1	1190.2	

Table 3.1. Continued

Identity	CH_2Cl_2 in Ar / cm^{-1}	CH_2Cl_2 in Kr / cm^{-1}	CH_2Cl_2 in Xe / cm^{-1}	Identity	CD_2Cl_2 in Ar / cm^{-1}	CD_2Cl_2 in Kr / cm^{-1}	CH_2Cl_2 in Xe / cm^{-1}
CCl_2	NR	755.1		CCl_2	746.2	755.5	
		740.8				741.2	
	719.7				NR		
	717.5						
$CH_2Cl^•$	1389.9			$CD_2Cl^•$	1046.3		
	825.9	826.5	829.3		788.1	790.5	792.5
	820.4	820.4	823.6		781.5	784.4	786.4
	396.1	395.2	388.6				
	395.1	392.2					
$HCCl^{+•}$	1077.9						
	1070.4						
HCCl	1200.8	1200.6					
	815.1	816.8					
$HCl_2^·$	955.8			$DCl_2^·$	463.5	438.2	
	696.4	664.1					
$CCl^•$	870.5	866.2	859.9	$CCl^•$	870.2	866.2	859.9
	864.7	860.2	853.4		864.7	859.9	853.4
HCl	2869.1						
Rg_2H^+			1063.9	Rg_2D^+			
			953.9			938.3	752.4
		1009.1	843.6			771.8	635.3
	NR	854.0	731.9		644.0	607.2	517.2

NR=not resolvable due to interference from precursor

1193.2 cm^{-1} indicates that this absorption, which had overlapped the $CCl_2^{+\bullet}$ absorption at 1192.7 cm^{-1} in the CH_2Cl_2 experiment has been shifted upon deuteration. A band is observed at 897.4 cm^{-1} in the CD_2Cl_2 experiment, which loses intensity on irradiation with red light and is assigned to the parent cation which is presumably shifted from 1193.2 cm^{-1} in the CH_2Cl_2 experiment. Assignments could not be made for the 1190.7 or the 1195.1 cm^{-1} features but according to their intensity ratios they may be due to chlorinated species.

Upon destruction of the features associated with isodihalomethane, a feature at 955.8 cm^{-1} was observed. This band is assigned to the $\nu_1 + \nu_3$ combination band of the bichloride anion $ClHCl^-$.[7] The ν_3 absorption was also observed at 696.4 cm^{-1}. The corresponding ν_3 band of $ClDCl^-$ was observed in the deuterium experiments.

The bands assigned to $CH_2Cl^{\bullet}$ [8,9] were not affected by irradiation using any of the filters but did increase slightly upon exposure to the full output from the xenon arc lamp. Those assigned to $CHCl_2^+$ [6] approximately doubled in intensity upon exposure to 30 minutes of >300 nm light. Bands previously assigned[6] to $CDCl_2^+$ were also observed in the CD_2Cl_2 experiments. Features could not be assigned with any certainty to the deuterated counterpart[10,11] of the neutral species $CHCl_2^{\bullet}$.

In the CH_2Cl_2 experiments, two sets of features, one appearing at 2881.8 and 3107.7 cm^{-1} and the other appearing at 2903.2 and 3129.9 cm^{-1}, were observed. The first set lost intensity after 30 min irradiation with >300 nm light and were completely destroyed upon irradiation with the full output from the lamp. Irradiation had only a very small effect on the second set of features in that they increased only slightly in intensity. In the CD_2Cl_2 experiments, a set of features corresponding

to the first set, described above, were observed at 2129.1 and 2061.3 cm^{-1} which displayed the same behaviour on irradiation with the 300 nm cut-off and the full lamp, decreasing in intensity on both exposures. These bands have all been previously assigned to the complex $(CH_2Cl^+)Cl^\bullet$ or its deuterated isotopomer.[6]

Bands corresponding to $CCl^\bullet$,[12] were also observed in both the CH_2Cl_2 and CD_2Cl_2 experiments. Bands assigned to HCCl[13] and the corresponding cation were observed, however, the deuterated isotopomers were not identified in the CD_2Cl_2 experiments.

In the CD_2Cl_2 experiments, an intense band at 644.0 cm^{-1} corresponding to Ar_2D^+ was observed but no Ar_2H^+ was observed in the CH_2Cl_2 experiments even though it was expected, especially since the deuterium isotopomer was so intense.

3.3.2.2 CH_2Cl_2 or CD_2Cl_2 in Krypton or Xenon

In Table 3.1 are listed the new features observed after EBMI of 1 in 400 mixtures of CH_2Cl_2 or CD_2Cl_2 in krypton. Some of the bands corresponding to the isodichloromethane features were observed, but with less intensity than in the argon experiments. These bands displayed the same behaviour as those in the argon experiments, being unstable to exposure with light >550nm.

As is shown in Table 3.1, it was possible to assign features to all of the same species as were observed in the argon experiments except for $HCCl^{+\bullet}$ and HCl.

Both Kr_2H^+ and Kr_2D^+ were present in sufficient abundance to observe the $\nu_1 + \nu_3$ combination bands also. The bands due to the deuterium isotopomers were much more intense than those due to Kr_2H^+. Kr_2H^+ had an absorbance of about

0.03 while Kr_2D^+ had an absorbance of about 0.2.

As in the argon experiments, a set of features were observed at 3128.9 and 2912.2 cm^{-1} when CH_2Cl_2 was the precursor. These bands correspond well with one of the sets of features assigned above to $(CH_2Cl^+)Cl^•$, however, these bands were unstable to exposure with >300 and >200 nm radiation and no growth of features were observed. No features due to the deuterated complex were identified.

Due to their behaviour on exposure of the matrix to irradiation with red light it was possible to assign a number of bands to both isotopomers of isodichloromethane in a Xe matrix. The only other bands identifiable in the xenon experiments were those corresponding to $CH_2Cl^•$, $CCl^•$ and Xe_2H^+ (Xe_2D^+ when CD_2Cl_2 was the precursor). The bands associated with Xe_2D^+ were observed to be approximately ten times more intense than those due to the hydrogen isotopomer.

3.3.2.3 EBMI of Pure Rare Gases Above Dichloromethane-Doped Matrices

Isomerization of dihalomethanes by vacuum-UV (V-UV) light is a well-known process. Given that electron bombardment of rare gases might give rise to V-UV emission, the contribution of such V-UV irradiation to the isomerization process under the present ionization conditions was investigated.

An argon matrix was prepared, without the electron beam on, as above for 8 h at a gas flow rate of 1.6 sccm which contained 1 part dichloromethane in 400 and an infrared spectrum of the resulting matrix was recorded. Following electron bombardment of pure krypton, originating from a separate bulb, directly above the

Ar/dichloromethane matrix, a second infrared spectrum was obtained and showed no difference, i.e. no products or destruction of dichloromethane was observed. The same null result was observed when pure argon was submitted to electron bombardment above a krypton matrix containing 1 part dichloromethane in 400. These results show conclusively that irradiation by resonant emission from excited rare-gas atoms is not significant in the destruction of dichloromethane or production of isodichloromethane.

When pure argon was ionized directly above a 1/400 dichloromethane/argon matrix, interestingly, a small amount of isodichloromethane was observed. The intensities of the 772.3 and 763.4 cm^{-1} absorptions of isodichloromethane were less than 3% of the same features observed by conventional EBMI of dichloromethane/Ar mixtures as described in section 3.3.2.1 above. No other absorptions were observed. The small amount of isodichloromethane observed is likely due to argon cations impinging on the dichloromethane-doped matrix. The charge is easily transferred to an argon host atom where dichloromethane may be ionized and subsequently isomerizes. The ion may then neutralized by recombination with a low energy electron or by some other process (*vide infra*). The insignificant destruction of dichloromethane precursor is evidence that the condensed phase chemistry is not very important.

3.3.3 Discussion

3.3.3.1 Ionization Processes

The results of the present study offer some interesting insights into the processes which accompany ionization of dihalomethanes, and again illustrate the general utility of matrix-isolation techniques in complementing gas-phase ion-chemistry studies. Various ionic fragment products such as $CHCl_2^+$ and $CCl_2^{+\bullet}$ are observed, as expected from mass spectrometric studies. In addition, several neutral products such as $CHCl_2^\bullet$ and CCl_2 are observed, which are typically not observed in conventional mass spectrometry, and whose presence has largely been inferred in previous mass spectrometric work.

In experiments by Zhang, where both CH_2Cl_2 and CH_2Br_2 were used as precursors and diluted in the same argon mixture, no features were observed which were attributable to the mixed isodihalomethane species,[3] even though they are well characterized products of CH_2ClBr V-UV photolysis[4] and electron bombardment matrix isolation.[3] The absence of halogen scrambling in the electron bombardment of mixtures of dichloro- and dibromomethane clearly shows that the isomerization process is intramolecular. Such observations are incompatible with a mechanism involving dissociation of a halogen atom from the parent ion, followed by recombination with a CH_2X fragment, either neutral or cationic. The conclusion from Zhang's work is that the formation of the isodihalomethanes is via isomerization, either of the cationic form $CH_2X_2^+$ or of the neutral form CH_2X_2. Isomerization of the latter would require significant energy input, either from excitation due to direct electron impact, or following electron-cation recombination. In the rest of this

section, it is argued that the most likely route to neutral isodihalomethane formation is via electron recombination with the cation having the isomerized $(CH_2X^+)X$ form, following isolation of the latter in the matrix solid. A similar process has been proposed for the isomerization of acetone to 1-propen-2-ol.[14]

The experimental observation that the isodichloromethane absorptions arose in experiments involving electron bombardment of Ar as well as in Kr and Xe suggests that the formation of the dichloromethane cation via a charge-exchange collision between the rare-gas cation and dichloromethane is a pre-requisite for the formation of neutral isodichloromethane. The direct photoisomerization of the neutral molecule by resonant emission from the rare gases is not a contributor as was found in the experiments utilizing resonance emission from Ar* (Section 3.3.2.3).

There has been some discussion as to whether the products observed in these EBMI experiments are actually due to isomerization or decomposition of an electronically-excited neutral precursor. This excited neutral could be the product of collisions between metastable rare-gas atoms Rg* and the ground-state neutral precursor, especially since these species have long lifetimes (~1 sec) in the gas phase.[15] The fact that many ions are observed in the dichloromethane experiments indicates that ion chemistry is an important contributor in these experiments. Furthermore, the fact that the current, measured at the anode, increases by two orders of magnitude when the gas flow begins suggests that ionization is occurring. Rare-gas cations formed by electron impact have much longer lifetimes, in fact infinite lifetimes, in the absence of a molecule with a lower ionization potential than

that of the rare-gas. Similarly, the observation of some isomeric species such as 1-propen-2-ol[14] and various isotopomers of decomposition products of CD_3OH discussed in Chapter 4 are best explained by neutral-base catalysed hydrogen shifts of the corresponding radical cation (see chapter 6 for more details).

Further evidence that the observed chemistry occurs on an ionic potential energy surface can be obtained by comparing the results of the EBMI experiments conducted with each of the three diluent rare-gas systems. The magnitude of the ionization potential of CH_2Cl_2 (11.32 eV) lies between the excitation energies of the first excited-states of neutral Ar, (11.83 and 11.63 eV), and those of neutral Kr (10.64 and 10.03 eV). Collisions with neutral Ar metastables would result in ionization of dichloromethane, however, collisions with Kr or Xe metastables would not produce ions. Since similar products are observed after EBMI of Ar/CH_2Cl_2, Kr/CH_2Cl_2 or Xe/CH_2Cl_2 it can only be concluded that the chemistry observed results from charge-exchange collisions between Rg^+ and CH_2Cl_2. Although excited neutral chemistry cannot be directly ruled out, it is safe to say that, on the basis of the indirect evidence provided above, the initial step in the process is consistent only with charge-transfer ionization of the neutral precursor.

The presence of excess rare gases in the gas mixtures, statistically makes the CE reaction of CH_2Cl_2 with Rg^+ the most likely process. Following ionization of CH_2Cl_2 by this route, the accessible decomposition pathways are limited by the difference between the ionization energy (IE) of CH_2Cl_2 and the Rg^+ cation-electron recombination energy. In Figure 3.2 are displayed the relevant thermochemical relationships for the CE reaction of the rare-gas cations and dichloromethane. It is

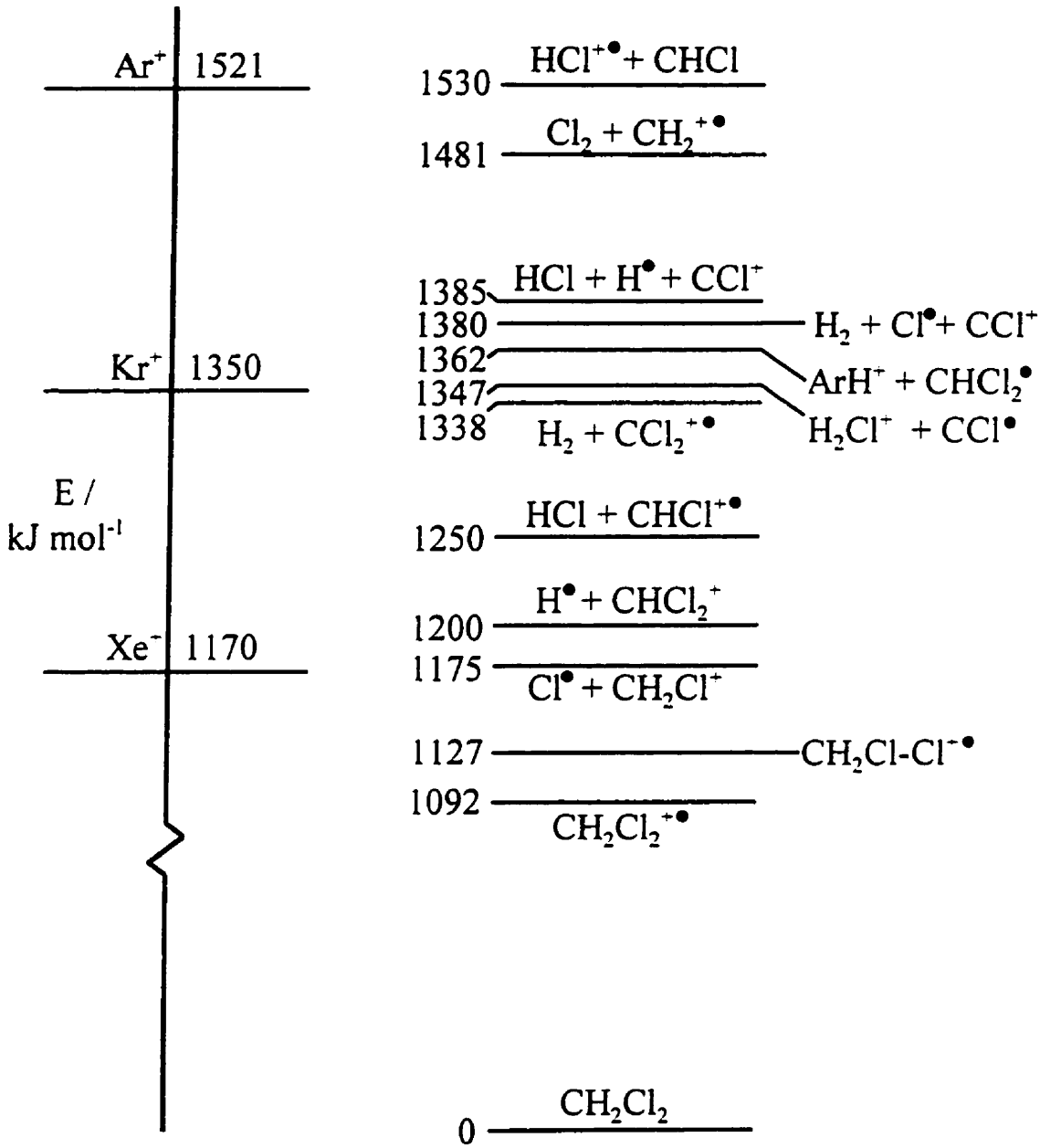

Figure 3.2. Energy level diagram showing many possible decomposition routes for the dichloromethane radical cation. Also shown is the available energy for unimolecular reaction following charge exchange between dichloromethane and Ar^+, Kr^+ or Xe^+. See text for discussion. Thermochemical data from reference 25.

clear that with Ar^+ as charge-exchange agent most of the decomposition pathways of $CH_2Cl_2^+$ are accessible. Even more importantly, the products observed after EBMI of the Kr/dichloromethane and Xe/dichloromethane mixtures, for the most part, correlate with what is expected if the initial step to the observed products is charge exchange with the rare-gas cation as is evident by comparing Figure 3.2 and Table 3.1. There are, however, a few exceptions that should be considered.

For example, the presence of HCCl in the krypton experiments can only be explained if one considers neutralization of $HCCl^+$ but, as expected, it is not observed in the xenon experiments. Similarly CH_2Cl is not expected in any of the experiments but evidence for its presence is observed in all three rare-gas systems. The cation is expected since it is the major product observed in mass spectrometry experiments. The observed neutral may be a product of CH_2Cl^+ or $(CH_2Cl^+)Cl$ neutralization in the matrix. The absence of spectral features assignable to the cation is puzzling but its infrared spectrum has never been observed in matrix experiments or in the gas-phase. Considering that this cation is a major product of dichloromethane radical cation decomposition, its absence is presumably due to it having infrared absorptions that are extremely weak or that neutralization of this species in rare-gas matrices is very efficient.

The presence of CCl in all three cases is difficult to explain except that the possibility of some direct electron impact ionization of dichloromethane could be expected. In the case of 300 eV electron impact ionization the CCl fragment would surely be expected.

It would also be expected that isomerization following charge exchange with

Ar^+ would leave the newly-formed isomer with an abundance of energy such that it would rapidly decompose. After charge exchange with Ar^+, collisions between the newly-formed molecular ion and precursor would effectively quench internal energy or it may be that ions are quenched in a liquid-like phase just above the matrix surface. The former hypothesis is supported by the observation that when the amount of precursor in the initial gas mixture was decreased there is a relative increase in fragmentation products and a relative decrease in isodichloromethane and greater decomposition of the precursor. Quenching is discussed further below in section 3.4 with respect to the oxalyl chloride experiments.

It should be noted that most of the bands due to isodichloromethane observed in argon and reported in Table 3.1 are due to site splitting. The absence of many of these bands in the krypton experiments may not be due to less product, but that there are simply not as many differing sites in the krypton matrix. This may also be the case for xenon, but the bands for isodichloromethane are considerably less intense than for those due to isodichloromethane in argon or krypton.

3.3.3.2 Neutral Isodichloromethane

Isomerization of dichloromethane cations to the isodichloromethane form requires a subsequent neutralization step to allow for the observation of the neutral isodihalomethane. It is reasonable to propose that the neutralization step should occur following isolation of the isomerized cation in the solid matrix. This is reasonable since the energy which would be associated with electron cation recombination the gas phase would be close in magnitude to the ionization energy of CH_2Cl_2. The barrier to back isomerization or decomposition of neutral

isodichloromethane is not likely to be nearly as large as this, such that gas-phase neutralization would be expected to result in rapid and highly-exothermic dissociation of the newly-born neutral molecule. Neutralization in the matrix solid would give the greatest probability of effective electron-cation recombination and stabilization of neutrals formed in this way. Such a series of steps, ionization-isomerization-isolation-neutralization-stabilization, has also been proposed for the isomerization of acetone to 1-propen-2-ol.[14]

3.3.3.3 Barrier to $CH_2Cl_2^{+\bullet}$ to $CH_2ClCl^{+\bullet}$ Isomerization

The position of the $CH_2Cl\text{-}Cl^+$ ion in the energy level diagram shown in Fig. 3.2 and the fact that isodichloromethane is observed in xenon, allows one to put an upper limit on the barrier for $CH_2Cl_2^{+\bullet}$ to $CH_2ClCl^{+\bullet}$ isomerization of about 78 kJ mol^{-1}. This barrier has not been determined experimentally and theoretical attempts to estimate its magnitude[16] have so far been unsuccessful.

3.4 Oxalyl Chloride[A]

3.4.1 Introduction

The chemistry of the oxalyl chloride radical cation, $(COCl)_2^{+\bullet}$, has received very little attention in the past despite the wide use of the neutral in applications such as manufacturing pharmaceuticals, antioxidants, agrochemical intermediates and photographic chemicals.[17] In their attempts to generate neutral ethylenedione OCCO in neutralization-reionization (NR) experiments, Chen and Holmes[18] report

---

[A] Section 3.4 is a modified version of the manuscript published as T.D. Fridgen and J. Mark Parnis, J. Phys. Chem., 1997, 101, 5117.

that of all precursors studied, $(COCl)_2$ yields the largest amounts of $OCCO^{+\bullet}$ on electron impact. Although their efforts did not result in a survivor ion peak at *m/z* 56 in the O_2/Xe NR mass spectrum, the kinetic energy released, based on the breadth of the *m/z* 28 peak, due to $CO^{+\bullet}$, was considered to be evidence of dissociation of internally-excited neutral OCCO. Similarly, the presence of $C_2O^{+\bullet}$, $CO_2^{+\bullet}$, $C_2^{+\bullet}$ in the NR mass spectrum was interpreted to be the result of fragmentation of wholly-dissociative $OCCO^{+\bullet}$ ions produced from vertical ionization of neutral OCCO having a lifetime greater than the approximately 1 μs required to traverse the distance between the neutralization and reionization cells. The electron impact mass spectrum of $(COCl)_2$ also includes features due to $ClCO^+$, $CO^{+\bullet}$, Cl^+, $CO_2^{+\bullet}$, and due to small amounts of $Cl_2CO^{+\bullet}$, $C_2O_2Cl^+$ and the molecular ion.[19]

The results of EBMI on mixtures of oxalyl chloride diluted in Ar, Kr, N_2 and CO as well as mixed diluents will be discussed in this section.

3.4.2 Results

3.4.2.1 EBMI of Oxalyl Chloride in Argon and Krypton

Electron bombardment of Ar and Kr gas mixtures containing one part of $(COCl)_2$ in 200, 400 or 800 all resulted in its efficient decomposition as is evident by comparison of the infrared spectrum of oxalyl chloride in Ar[20] to spectra taken after EBMI. The first part of the spectrum in Figure 3.3 shows the carbonyl stretching region and it is obvious that very little $(COCl)_2$ is left after EBMI of 1 part $(COCl)_2$ in 400 parts Ar. As well, after EBMI many new bands appeared compared with the

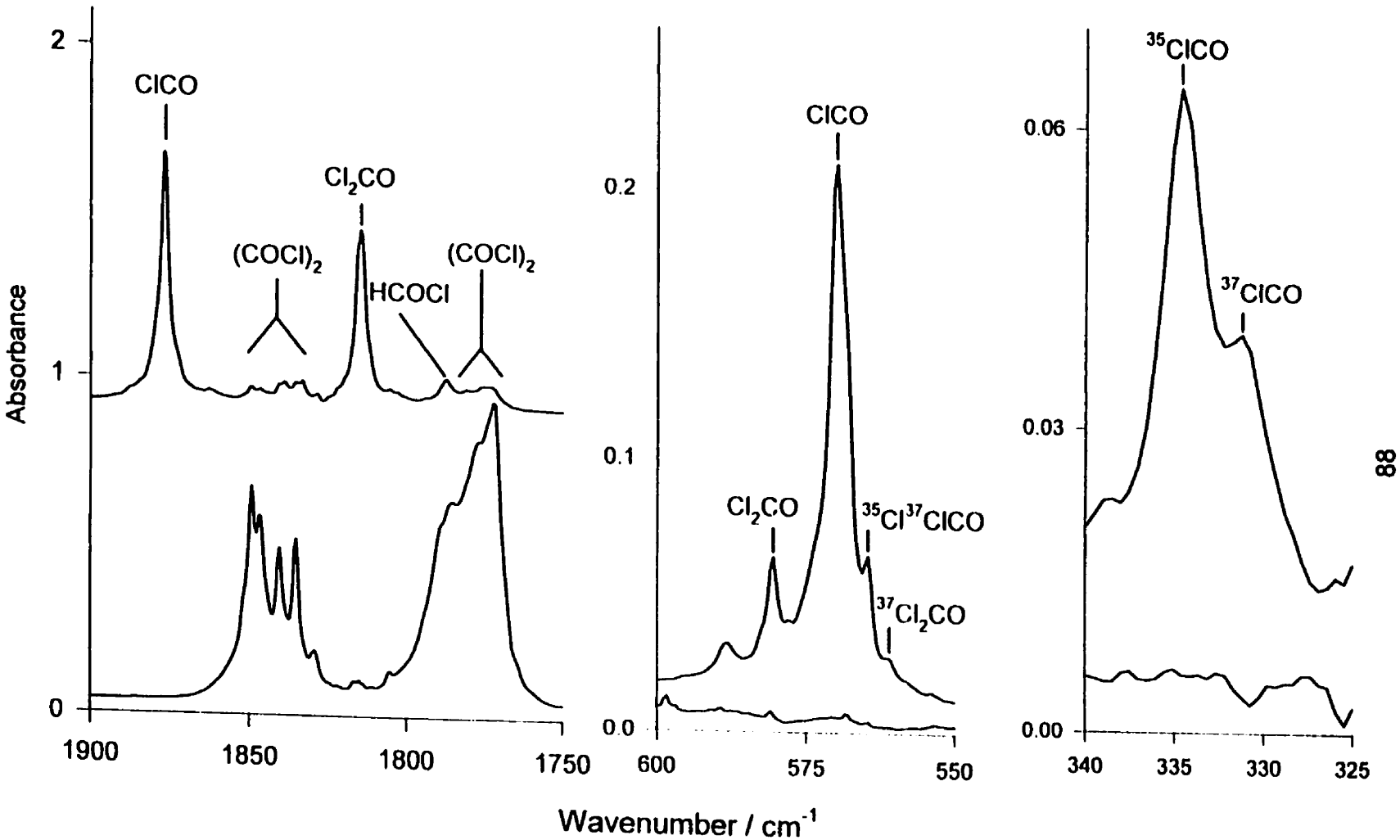

Figure 3.3. FTIR spectra of product regions after 3 h of EBMI of a 1 in 400 mixture of oxalyl chloride in Ar (top traces) and simple deposition of the same mixture for 3 h (bottom traces).

spectrum of the same gas mixture without electron bombardment. Table 3.2 summarizes the new features appearing after 20 h of EBMI of the 400/1 Ar/$(COCl)_2$ gas mixture.

The bands corresponding to the three isotopomers of phosgene[20a] (Cl_2CO) were stable to irradiation with visible and ultraviolet light as well as to annealing. Features assigned to the carbonyl chloride radical[21] (ClCO•) were stable to irradiation but slowly decreased in intensity on annealing at 35 K. The Cl_2CO and CO band intensity increased slightly during this annealing. The same effects were observed in solid krypton. It was observed that six minutes of annealing at 45 K was more than sufficient to eliminate all absorptions corresponding to ClCO• in Kr while Cl_2CO bands did not increase significantly in intensity. This effect of annealing on ClCO• absorptions has been observed previously.[22]

A very weak feature assignable to CCl• [23] was observed only in the Ar system. Nothing assignable to CCl_2[23] was observed, possibly due to spectral interference by the $(COCl)_2$ features. An enormous increase in carbon monoxide was observed; so much so, that after EBMI of $(COCl)_2$ the spectral features due its ^{13}C isotopomer[24] were observed with significant intensity.

It should also be noted that once the gas flow began the increase in the electron current rose again by over two orders of magnitude and remained high during electron bombardment of these rare-gas/$(COCl)_2$ mixtures as has been observed for all EBMI experiments. Again, this is evidence that ionizing processes are occurring during the electron bombardment process. It should also be noted that although ionization processes are occurring, the infrared spectra recorded

Table 3.2. New absorptions observed after 20 h of EBMI of a 1 in 400 mixture of oxalyl chloride in Ar.

observed band / cm^{-1}	intensity[a]	literature value[b]	assignment
2869.6	m	2870.	HCl
2814.6	m		
2802.3	sh		
2662.8	vw		
2482.0	vw	2483.	ν_1 HCO•
2259.0	sh		
2248.5	m		
2221.5	vw		
2178.3	sh		
2153.3	sh		
2148.8	sh	2148.8	carbon monoxide, ^{12}C
2138.4	vvs	2138.0	carbon monoxide, ^{12}C
2105.7	vw	2101.4	carbon monoxide, ^{13}C
2090.7	m	2091.7	carbon monoxide, ^{13}C
2049.4	vw		
2039.2	vvw		
1876.4	vs	1876.7	ν_3 ClCO•
1863.0	sh	1863.	ν_3 HCO•
1839.2	sh	1840.61	$\nu_2 + \nu_5 + \nu_6$ $^{35}Cl_2CO$
1833.7	sh	1834.71	$\nu_2 + \nu_5 + \nu_6$ $^{35}Cl^{37}ClCO$
1829.1	sh	1829.51	$\nu_2 + \nu_5 + \nu_6$ $^{37}Cl_2CO$
1814.4	vs	1814.	ν_1 Cl_2CO
1787.4	m	1784.	ν_2 HCOCl
1650.9	m	1650.98	$2\nu_5$ Cl_2CO
1398.0	vw	1399.12	$\nu_2 + \nu_5$ $^{35}Cl_2CO$

Table 3.2. Cont'd.

observed band / cm^{-1}	intensity[a]	literature value[b]	assignment
1393.6	sh	1394.63	$\nu_2 + \nu_5$ $^{35}Cl^{37}ClCO$
1388.7	sh	1390.02	$\nu_2 + \nu_5$ $^{37}Cl_2CO$
1305.0	vw	1307.	ν_2 $HCO^{\bullet}$
1240.0	vvw		
1160.2	vw	1160.65	$2\nu_4$ Cl_2CO
1185.7	w	1087.	ν_2 $HCO^{\bullet}$
1059.8	vvw		
1041.8	vvw		
1023.0	sh		
1018.0	vvw		
1009.7	w	1010.08	$\nu_2 + \nu_6$ $^{35}Cl_2CO$
1003.5	vw	1004.02	$\nu_2 + \nu_6$ $^{35}Cl^{37}ClCO$
997.7	vvw	997.97	$\nu_2 + \nu_6$ $^{37}Cl_2CO$
955.4	vw		
898.0	vw		
878.7	vvw		
869.7	vvw		
837.3	vvs		
810.2	w	837.36	ν_5 Cl_2CO
736.6	vw	809.81	$\nu_3 + \nu_6$ Cl_2CO
721.1	vw	739.	ν_4 HCOCl
696.0	m		
658.6	sh		
588.4	w		
580.6	m	580.	ν_4 Cl_2CO
569.9	vs	570.1	ν_1 $ClCO^{\bullet}$

Table 3.2. Cont'd

observed band / cm^{-1}	intensity[a]	literature value[b]	assignment
		568.29	ν_2 $^{35}Cl_2CO$
564.8	sh	564.75	ν_2 $^{35}Cl^{37}ClCO$
561.4	sh	561.12	ν_2 $^{37}Cl_2CO$
527.1	vw		
468.2	vw		
460.5	vw	458.	ν_5 HCOCl
334.5	m	334.6	ν_2 $^{35}ClCO^{\bullet}$
331.4	sh	330.9	ν_2 $^{37}ClCO^{\bullet}$

a: Intensity refers to peak hight as follows; vvs = above 1.75, vs = 1 to 1.74, s = 0.5 to 0.99, m = 0.1 to 0.49, w = 0.05 to 0.09, vw = 0.01 to 0.049, and vvw = less than 0.01 absorbance units, sh = shoulder.

b: See text for references.

following electron bombardment and subsequent matrix isolation of the rare-gas/oxalyl chloride mixtures do not result in identification of any bands which could be associated with ions. Since oxalyl chloride reacts with water, no bands were observed in the H_2O-bending region which could be used to assess the presence of ions in the matrix as discussed in chapter 1 (section 1.2.3.4).

3.4.2.2 N_2 and CO Doping Experiments

When N_2 and CO were used in place of the noble gas it was found that few products were observed and features corresponding to the precursor, $(COCl)_2$, were most abundant. In fact, the spectrum recorded without the electron beam on and the spectrum recorded after EBMI were virtually identical using pure N_2 or CO as the diluent and matrix support gas. This observation suggested that the diatomic molecules were acting as quenching agents, removing the excess internal energy deposited into $(COCl)_2^{+\bullet}$ during the ionization process, and stabilizing it with respect to unimolecular dissociation. It was, therefore, decided to explore the effect of adding varying amounts of N_2 or CO to the gas mixture, keeping the concentration of $(COCl)_2$ fixed.

For the Kr system, values of A_{ClCO}, A_{Cl2CO}, and $A_{(COCl)2}$ are plotted against % N_2 in Figure 3.5 and spectra in the carbonyl stretch region are shown for various values of % N_2 in Figure 3.4. As is evident from these two figures, bands corresponding to $(COCl)_2$, Cl_2CO and $ClCO^\bullet$ *all* initially increase with increasing amounts of N_2, at N_2 levels below about 18%. Features due to $ClCO^\bullet$ then begin decreasing in intensity, while amounts of Cl_2CO continue to increase until the level of N_2 reaches between 60% and 70%. $(COCl)_2$ features continuously increase in

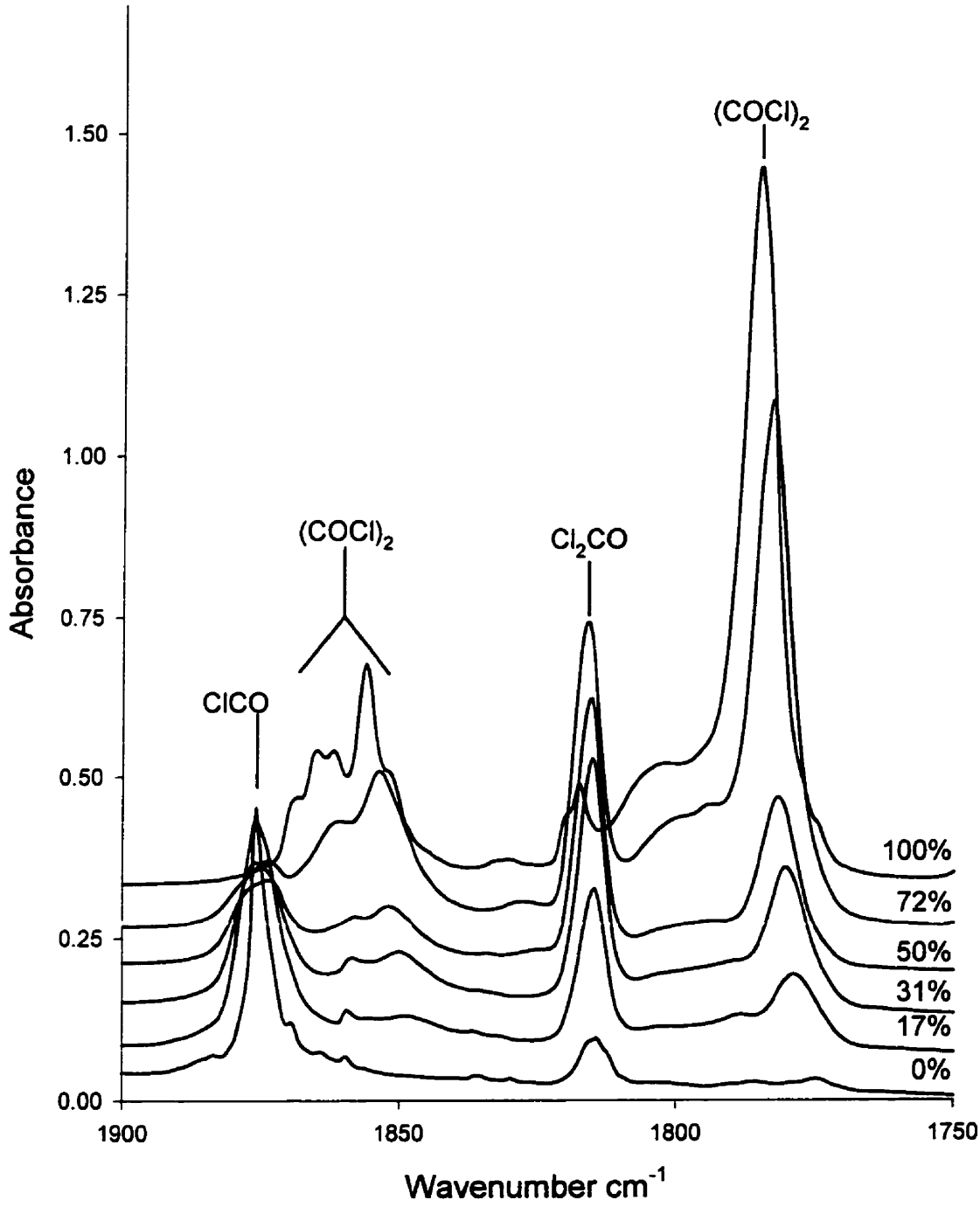

Figure 3.4. FT-infrared spectra in the region of C=O stretching modes taken after 3 h of EBMI of 1 part in 400 oxalyl chloride in a N_2/Kr mixture at different concentrations (mol %) of N_2 indicated to the right of each trace.

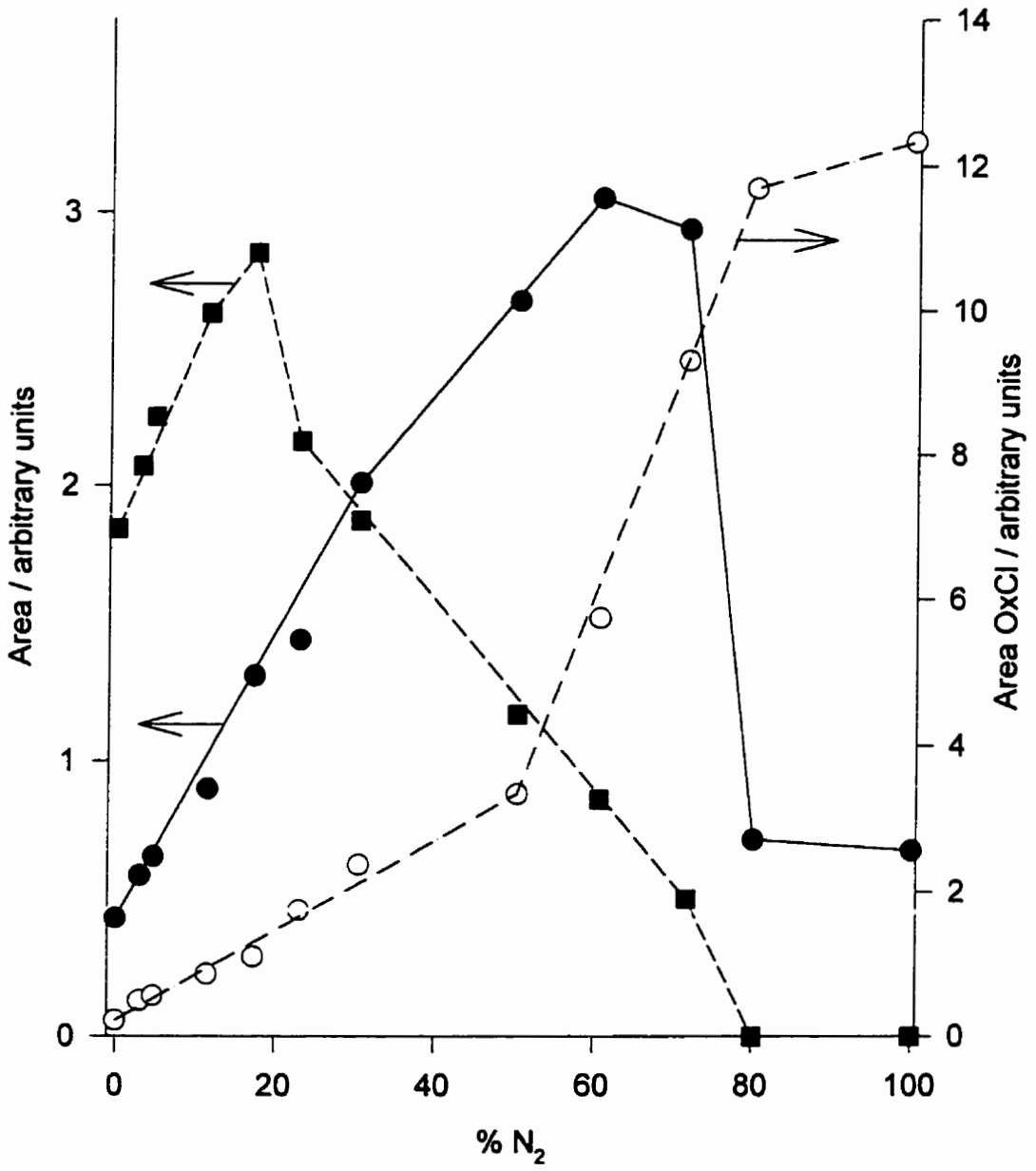

Figure 3.5. Plots of the areas under the C=O stretching mode of phosgene (●, left axis), carbonyl chloride radical (■, left axis) and oxalyl chloride (○, right axis) versus mol % N_2 in Kr; the lines are included to guide the eye.

ntensity with increased N_2. It should also be noted that the area under the CO feature drops continuously with increased N_2 composition, such that its area in pure N_2 is only about 12% of the area found in pure Kr.

It may be argued that the phosgene features increase faster in intensity since N_2 is becoming more and more important as the charge exchange agent which has a substantially higher electron affinity (EA<15.576 eV) than Kr, one that is actually similar to Ar, and has better quenching properties. This argument can be ruled out by considering that a similar trend in A_{ClCO}/A_{Cl2CO} is observed using CO (IP=14.01 eV), which has a similar IP to Kr, instead of N_2. As well, on a statistical basis, it can be argued that $Kr^{+\bullet}$ is still the major charge transfer agent up to quite high concentrations of N_2. This argument is based on the fact that $Kr^{+\bullet}$ has a lower EA than the IP of N_2 and cannot transfer its charge to N_2. Correspondingly, $N_2^{+\bullet}$ has a higher EA than the IP of Kr; if N_2 is ionized in the initial electron impact step, it can transfer its charge to Kr. This would not be true for Ar in place of Kr since the IP and, therefore, the electron affinity, of Ar is higher than N_2. For this reason, the experiments of varying N_2 concentration were performed in Kr rather than Ar.

It is proposed, then, that N_2 efficiently quenches *all* the internally-excited primary decomposition products in the gas phase; $Cl_2CO^{+\bullet}$, $ClCO^+$ and $ClCO^\bullet$. It is obvious as well, that N_2 also quenches the newly formed $(COCl)_2^{+\bullet *}$. The quenched species are then isolated in the matrix where the ions are subsequently neutralized.

3.4.3 Discussion

3.4.3.1 EBMI of Oxalyl Chloride in Argon and Krypton

The products observed from the decomposition of the oxalyl chloride radical cation are not totally unexpected. Nevertheless, the mechanisms for their generation are worthy some discussion. The simplest and most probable mechanism for ClCO$^{\bullet}$ formation is the cleavage of the C-C bond in $(COCl)_2$ $^{+\bullet}$to form ClCO$^{\bullet}$ and the carbonyl chloride cation ($ClCO^+$). Thermodynamically, this is not the most favoured process,[25] however, the barrier for cleavage of a very weak C-C bond may be low enough to make this process the one with the lowest activation energy requirement. C-C cleavage of $(COCl)_2^{+\bullet *}$ still leaves the products with much energy and, since the barrier for ClCO$^{\bullet}$ decomposition is very low[26] 29 kJ mol^{-1} (0.30 eV), neutral ClCO$^{\bullet *}$ is not able to survive long enough to reach the growing matrix as is the cation which is known to have a high barrier to decomposition.[20] The large amount of ClCO$^{\bullet}$ observed after EBMI of $(COCl)_2$/Ar and $(COCl)_2$/Kr mixtures, therefore, provides further indirect evidence that ion chemistry is being observed. Furthermore, this is confirmation that neutralization occurs near or in the matrix since gas-phase neutralization of $ClCO^+$ would likely result in its rapid decomposition.

In the electron impact mass spectrum of $(COCl)_2$,[20] the most prominent feature is at m/z 63 corresponding to $ClCO^+$. There is only a very small signal due to the phosgene radical cation ($Cl_2CO^{+\bullet}$) at m/z 98. In the present experiments employing charge exchange ionization with $Ar^{+\bullet}$, one of the major products observed in the matrix is Cl_2CO. Cl_2CO can be formed directly as a neutral by

extrusion of $CO^{+\bullet}$ from $(COCl)_2^{+\bullet}$ (eq. 3.1), but extrusion of neutral CO is much more thermodynamically favoured (eq. 3.2). The product that retains the positive charge in unimolecular decompositions of cations is the product with the lower IP[27] and since the $IP(Cl_2CO)<IP(CO)$,[28,29] the more favourable process will be the one producing $Cl_2CO^{+\bullet}$ and neutral CO.

$$(COCl)_2 \rightarrow CO^{+\bullet} + Cl_2CO \quad \Delta_r H = 298\,kJ\,mol^{-1} \qquad \textbf{(3.1)}$$

$$(COCl)_2 \rightarrow CO + Cl_2CO^{+\bullet} \quad \Delta_r H = 47\,kJ\,mol^{-1} \qquad \textbf{(3.2)}$$

Reactions 3.1 and 3.2 are both endothermic, however, addition of the 4.47 eV (431 kJ mol^{-1}) transferred to $(COCl)_2^{+\bullet}$ by ionizing with $Ar^{+\bullet}$ makes both processes quite exothermic. Intuitively, one would expect a significant barrier for the concerted extrusion of CO from $(COCl)_2^{+\bullet}$, forming $Cl_2CO^{+\bullet}$. Using $Ar^{+\bullet}$ as the charge exchange agent would facilitate overcoming this barrier. It may be concluded that by using charge exchange with $Ar^{+\bullet}$, $Cl_2CO^{+\bullet}$ is formed by concerted extrusion of CO.

Another possibility for the formation of $Cl_2CO^{+\bullet}$ from $(COCl)_2^{+\bullet}$ exists which does not include a concerted extrusion of CO but a stepwise reaction where Cl is transferred to a carbonyl oxygen followed by cleavage of the C-C bond to form CO and rearrangement of the resulting cation to form the phosgene radical cation or loss of a chlorine atom to form the carbonyl chloride cation. This is summarized in

the following scheme,

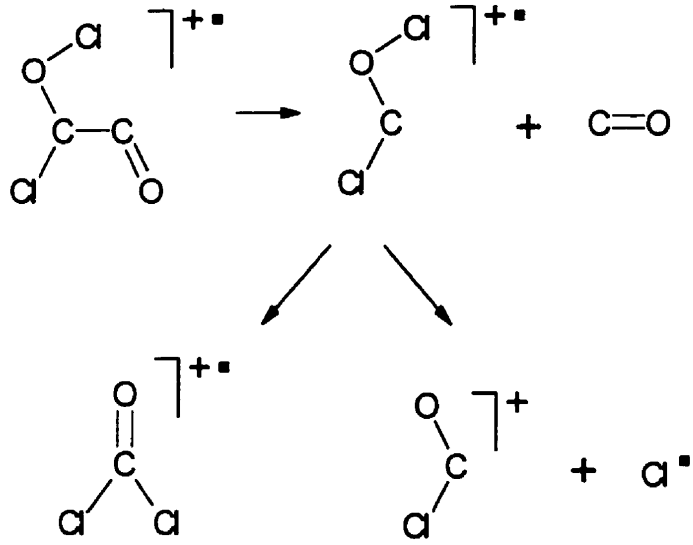

This scheme is expected to have a lower energy requirement for formation of phosgene radical cation than the concerted extrusion of CO mechanism.

The resulting cations are then isolated in the matrix where they are neutralized. The large peak at m/z 28 in the EI mass spectrum[20] may, in part, be due to extrusion of $CO^{+\bullet}$, but is more likely due to decomposition of $ClCO^{+\bullet}$.

Both Cl_2CO and $ClCO^{\bullet}$ can also be produced as neutrals in the matrix or in the gas-phase by recombination of a chlorine atom with $ClCO^{\bullet}$ and CO, respectively. The reaction between $Cl^{\bullet}$ and CO is known to be exothermic and barrierless.[22,26] These mechanisms are unlikely in the present experiments due to the very low concentration of non-rare-gas species that are expected to be present in the gas phase. Recombination in the matrix is not an important process due to the low concentration of reactants and extremely limited diffusion of $Cl^{\bullet}$ atoms in an

Ar matrix below 20 K.[30]

No bands in the infrared spectrum were assignable to ethylenedione (OCCO) on comparison with calculated infrared spectra.[31] Its absence is not totally unexpected when considering the energetics of its formation. On charge exchange with $Ar^{+\bullet}$, the energy available for ionization and reaction of $(COCl)_2$ is 15.76 eV (electron affinity of $Ar^{+\bullet}$). This energy lies on the threshold of the appearance energy of $OCCO^{+\bullet}$ from $(COCl)_2$, found by Chen and Holmes to be 15.7 ± 0.1 eV.[18] It should, however, be possible under other conditions to generate OCCO since its lowest spin-allowed dissociation limit is 310 kJ above the minimum corresponding to OCCO in its triplet state.[31] Changing the matrix gas and, therefore, the charge-exchange agent to neon (IP=21.56 eV) would more than satisfy the energetics of formation of $OCCO^{+\bullet}$. This ion could then be trapped in the matrix and neutralized for spectroscopic characterization. A complication may be that $OCCO^{+\bullet}$ would be formed from $(COCl)_2$ and $Ne^{+\bullet}$ having too much internal energy to survive the time between formation and isolation in the matrix. This problem may be solved by doping the gas mixture with a quenching gas (effects of which are discussed in detail below) to remove the excess energy from $OCCO^{+\bullet}$ in the gas-phase.

Bands were assigned to three hydrogen-containing species: $HCO^{\bullet}$,[32] HCl,[23] and HCOCl.[33] It is assumed that these products are formed by reaction of water and oxalyl chloride in the premixed gas sample or during electron bombardment of the products this reaction.

In the Kr system, $Kr^{+\bullet}$ is the charge exchange agent and only transfers 14.00 eV into $(COCl)_2$, of which 11.29 eV are used in ionizing oxalyl chloride leaving 2.71

eV (261 kJ mol^{-1}) for unimolecular reaction. There is less energy available, therefore, for decomposition compared to the Ar system. The products of decomposition are similar to those observed in the Ar system but, their relative yields differ and $CCl^{\bullet}$ was not observed. It should also be mentioned that extrusion of $CO^{+\bullet}$ to form neutral Cl_2CO is slightly endothermic for the Kr system. Therefore, Cl_2CO could only be produced as a radical cation from $(COCl)_2^{+\bullet}$ using $Kr^{+\bullet}$ as charge exchange agent as in eq. 3.2 above.

The intensity of the ν_1 band of $ClCO^{\bullet}$ dropped by a factor of two while the ν_1 band of Cl_2CO saw a 6-fold decrease in intensity in going from the Ar to the Kr system (compare Fig. 3.3 and Fig. 3.5). This may be explained by considering that the barrier for concerted extrusion of CO by the $(COCl)_2$ radical cation, forming $Cl_2CO^{+\bullet}$ is the process with the higher activation energy requirement. Since this parent ion is formed with less internal energy in the charge-exchange reaction between the neutral precursor and $Kr^{+\bullet}$ than with $Ar^{+\bullet}$ it is expected that much less $Cl_2CO^{+\bullet}$ would be produced in the krypton system.

3.4.3.2 Quenching by N_2 and CO

It is evident from the results that more $Cl_2CO^{+\bullet}$ is produced with some N_2 present than is observed as neutral Cl_2CO in the matrix in the absence of N_2 Energetic phosgene radical cation $Cl_2CO^{+\bullet *}$ formed as in eq. 3.3 may, therefore, decompose further before being trapped in the matrix in the absence of N_2. The products for this secondary decomposition are $ClCO^{+}$ and chlorine atom (eq. 3.4).

$$(COCl)_2^{+\bullet} \rightarrow CO + Cl_2CO^{+\bullet} \quad \textbf{(3.3)}$$

$$Cl_2CO^{+\bullet} \rightarrow Cl^{\bullet} + ClCO^{+} \quad \textbf{(3.4)}$$

These results suggest that a second mechanism for formation of $ClCO^+$ in the gas phase exists besides simple C-C cleavage of the oxalyl chloride radical cation; secondary decomposition of internally hot $Cl_2CO^{+\bullet}$ (eq. 3.4).

The fact that the amount of $ClCO^{\bullet}$ levels off and starts to decrease at about 18% N_2 is a result of the two separate processes for its production being suppressed by N_2 quenching as in eqs. 3.5 and 3.6.

$$Cl_2CO^{+\bullet} + N_2 \rightarrow Cl_2CO^{+\bullet} + N_2 \quad \textbf{(3.5)}$$

$$(COCl)_2^{+\bullet} + N_2 \rightarrow (COCl)_2^{+\bullet} + N_2 \quad \textbf{(3.6)}$$

The amount of Cl_2CO observed increases due to eq. 3.5, until higher levels of N_2 and then eq. 3.6 becomes more important also cutting off the source of $Cl_2CO^{+\bullet}$.

Doping in the Ar system was not performed since N_2 or CO would be ionized in a collision with $Ar^{+\bullet}$ due to their lower IP (as discussed above). It is expected that if a quenching agent could be found with a higher IP than Ar similar results would be attained as just described for Kr.

It should be noted that adding only a very small amount of N_2 (0.25%) to both $(COCl)_2$/Ar and $(COCl)_2$/Kr gas mixtures and subjecting the mixture to EBMI resulted in no observable difference in the EBMI infrared spectrum compared to when N_2 was absent. Kenty,[34] and much earlier Worthing and Rudy,[35] observed that when small amounts of N_2 were present (< 0.2%) in a gaseous mixture of Ar or Kr which was passed through a discharge, the emissions due to Ar or Kr were quenched. They concluded that the lower metastable levels of Ar and Kr were efficiently quenched in the presence of these small amounts of N_2. If these metastable states of the rare gas were causing Penning ionization of $(COCl)_2$, a difference in the ratios of *some* products would be expected due to a lower amount of internal energy being deposited into $(COCl)_2^{+\bullet}$ compared to charge exchange. This is further evidence that Penning ionization is not an important process in these EBMI experiments as was concluded above in section 3.3.3.1.

3.4.3.3 Comments on the mass spectra of Oxalyl Cloride

These quenching studies, using various diluent/dopant gases, answer some questions pertaining to the mass spectrum of $(COCl)_2$. Why, in electron impact ionization mass-spectrometric experiments, is $Cl_2CO^{+\bullet}$ only observed in minute quantities? The explanation comes from the fact that $Cl_2CO^{+\bullet}$ is expected to have excess vibrational energy on formation and decomposes such that it is not detected in significant abundance. The fact that we observe Cl_2CO in such good abundance in our experiments, even without N_2 present, is that some of the initially internally-hot $Cl_2CO^{+\bullet}$ formed may be quenched by the bath of Ar and Kr in the gas phase. It is proposed that by adding a quenching gas, such as N_2, or even Ar or Kr, in the

source for EI experiments, a greater intensity of $Cl_2CO^{+\bullet}$ and the molecular ion will be observed along with a lower abundance in the $ClCO^+$ signal. As well, it is proposed that a metastable ion peak would probably be observed corresponding to $Cl_2CO^{+\bullet}$ in a metastable ion spectrum of $(COCl)_2^{+\bullet}$.

It has been suggested that the only reason for observed differences in the relative intensities of peaks in mass spectra obtained when the ionization process is changed from EI to CE is simply the difference in internal energies of the ions formed by the two processes.[36,37] The internal energy acquired by a newly-formed ion in a CE reaction is specific (for example 15.76 eV - IP(of reactant for) CE with $Ar^{+\bullet}$), but ionization by EI gives ions with a large range of internal energies. This may in fact give differing intensities in mass spectra but the fact that the charge-exchange agent may also be a quenching agent, to our knowledge, has not been discussed as having an effect on product ratios. The differing degrees of fragmentation is not only a result of the ionization process, but also a result of more of the primary (and to lessening degrees secondary, tertiary, etc) decomposition products being quenched by what is essentially a bath of quenching gas in the source. Adding a quenching gas is not a new concept, however, since mass spectrometrists often use N_2 in the ion source to stabilize metastables. It is now suggested that CE ionization has the same effect of stabilizing metastables in the source since the CE agent is also likely to have quenching capabilities.

3.5 Why Some Ions and Not Others?

Presented in Table 3.3 are the adiabatic electron affinities of the various

cations which may be expected from the decomposition of the dichloromethane,oxalyl chloride and methanol radical cations (for the latter see chapter 4). It was noted in chapter 1 that Knight *et al.*[38] have observed that they were unsuccessful in isolating cations if there was less than ~5 eV difference between the ionization potential of the matrix substrate atom and the electron affinity of the cation in question. Utilizing the observed 5 eV difference, ions with an electron affinity greater than ~10.8 eV (IP(Ar) = 15.76 eV) are not expected to be observed in an argon matrix, but those with electron affinities less than ~10.8 eV would be expected. On this basis, those ions which are expected to be observed in the argon matrix are so noted in the last column of Table 3.3. In the second last column, whether or not these cations were observed in the experiments reported in this chapter and chapter 4 are similarly noted.

At this point, before discussing the exceptions indicated in Table 3.3 it may be quite beneficial to provide an explanation for it. Consider the charge-exchange reaction between an isolated cation C^+ and the argon matrix, denoted Ar_n,

$$C^+ + Ar_n \rightarrow C + Ar_n^+ \qquad (3.7)$$

The enthalpy change for this reaction can be written in terms of the heats of formation of the species,

$$\Delta_r H = [\Delta_f H(C) - \Delta_f H(C^+)] + [\Delta_f H(Ar_n^+) - \Delta_f H(Ar_n)]. \qquad (3.8)$$

The terms inside the first set of brackets equal the negative of the adiabatic

Table 3.3. Ions which may be expected on decomposition of oxalyl chloride radical cation, dichloromethane radical cation and the methanol radical cation.

Ion	EA_a / eV[a]	observed	expected
$CO^{+\bullet}$	14.01	✗	✗
$Cl_2CO^{+\bullet}$	11.4	✗	✗
$(COCl)_2^{+\bullet}$	10.91	✗	✗
$H_2CO^{+\bullet}$	10.87	✗	✗
$CH_3OH^{+\bullet}$	10.85	✗	✗
$CCl_2^{+\bullet}$	10.36	✔	✔
$HCCl^{+\bullet}$	9.84	✔	✔
$CHCl_2^{+}$	8.1	✔	✔

a) Reference 25.

electron affinity of the cation $Ea_a(C^+)$ (the adiabatic electron gain energy) and those inside the second set of brackets equate to the adiabatic ionization potential of the solid argon matrix $IP_a(Ar_n)$. Equation 3.8 can, therefore, be re-written

$$\Delta H = IP_a(Ar_n) - EA_a(C^{\cdot}). \qquad \textbf{(3.9)}$$

For the charge-transfer reaction denoted by eq. 3.7 to be thermodynamically possible and recognizing that only cations with adiabatic electron affinities of roughly 10.8 eV are observed the ionization potential of the host argon matrix would need to be roughly 10.8 eV. In fact, the onset of the photoemission from solid argon is 13.9 eV.[39] The charge-exchange reaction (eq 3.7) would still be endothermic by approximately 3.1 eV for cations with electron affinities of about 10.8 eV. However, do note, that the matrix in which the cations are embedded is not composed of pure argon, but is doped with various organic neutrals, anions and cations with (except for the latter) lower ionization potentials than argon atoms. The effect of these dopants would be to decrease the effective ionization potential of the matrix or to decrease $IP(Ar_n)$ such that cations with electron affinities of ~10.8 eV (rather than 13.9 eV) may be neutralized in the matrix. The effect of dopants on band gaps and photelectron emissions of rare-gas solids has been studied in detail. Doping argon solids with 1% Kr or 0.3% Xe results in a decrease of the photoemission onset to 12.2 eV and 10.2 eV, respectively.[40,41] Similarly, a matrix doped with small amounts of benzene was shown to begin emitting electrons when photons corresponding to 8.4 eV radiated on the solid.[40] Thus, it easily seen how high electron affinity cations

may not be easily stabilized in rare-gas solids such as argon due to charge-exchange with the matrix.

The cations which are not observed to conform to the discussion above are highlighted in Table 3.3. $CH_2Cl_2^{+\bullet}$ is not expected since it has a fairly large electron affinity. The bands assigned to this cation may in fact be mis-assigned. CH_2Cl^+, HCO^+ and CH_2OH^+ are expected but are not observed. The only firm spectroscopic characterization of the formyl cation comes from NMR[42] and ESR spectra.[38] A very broad and extremely weak infrared absorption has been assigned to the formyl cation[42] at about 2100 cm^{-1} but the species cannot be described as a free cation since it was observed under approximately 28 atm of CO and the strongest known superacid, HF-SbF_5. Similarly elusive in the infrared has been CH_2Cl^+ despite numerous attempts under ionizing conditions and despite it being the lowest energy decomposition product of the dichloromethane radical cation. It can only be concluded, therefore, that these species are present, but in quantities which are not observable by the relatively insensitive infrared spectroscopy.

3.6 Conclusions

The EBMI experiments performed on mixtures of oxalyl chloride or dichloromethane in rare gases have resulted in some interesting chemistry as well as the characterization of the processes occurring during and following electron bombardment and similarly during matrix isolation of the resultant.

To summarize the processes believed to be occurring during EBMI experiments, the initial step is electron bombardment of the rare gas to form the

rare-gas radical cation $Rg^{+\bullet}$. A charge transfer reaction between Rg and the organic dopant (i.e. dichloromethane or oxalyl chloride) produces an internally hot organic radical cation $C^{+\bullet *}$. This cation can decompose by various routes or isomerize depending upon the amount of internal energy (*) deposited into the cation during the charge-exchange step. This amount of energy depends upon the electron affinity of the rare-gas cation and the ionization potential of the organic. Following decomposition or isomerization, the products may have sufficient energy to undergo further secondary decomposition reactions. It has been shown that the addition of N_2 acts to stabilize the parent cation and products by quenching their internal energies. Evidence has also been given which shows that even the excess precursor (or possibly products) can act as quenching agents. Following the gas-phase reactions, the products are condensed into a cryogenic matrix where they are finally quenched and isolated from further reaction. Cations with electron affinities above about 10.8 eV are not expected to be observed but are neutralized in the matrix. Evidence is also provided that rules out the process of Penning ionization and processes involving absorption of resonant emission from excited states of the rare-gas neutrals.

The electron bombardment and matrix isolation technique is quite unique in that all products of decomposition may be potentially probed simultaneously by spectroscopic means. The technique may find use in the isolation and spectroscopic characterization of some important molecules which have eluded direct observation to date. These include molecules such as OCCO,[18,31] oxirene,[43] and the tautomers of formamide[44] and N-methyl formamide. [44] All have been

observed in NRMS experiments and all are proposed to be obtainable through the corresponding radical cations. The correct choice of precursors, charge exchange agent, and quenching agent may result in the matrix isolation and direct observation of these very important and interesting molecules.

3.6 References to Chapter 3

1. Bortolini, O.; Maccioni, A.M.; Seraglia, R.; Traldi, P. *Org. Mass Spectrom.* **1990**, *25*, 247.
2. Bortolini, O.; Hamdan, M.; Traldi, P. *Rapid Comm. Mass Spectrom.* **1992**, *6*, 71.
3. Zhang, X.K., Ph.D. Thesis, Queen's University, Kingston, Ontario, 1993.
4. Maier, G.; Reisenauer, H.P.; Hu, J.; Schaad, L.J.; Hess, B.A.Jr. *J. Am. Chem. Soc.* **1990**, *112*, 5117.
5. a) Andrews, L.; Keelan, B.W. *J. Am. Chem. Soc.* **1979**, *101*, 3500. b) Keelan, B.W.; Andrews, L. *J. Phys. Chem.* **1979**, *83*, 2488.
6. Kelsall, B.J.; Andrews, L. *J. Mol. Spectra* **1983**, *97*, 362.
7. Rasanen, M.; Seetula, J.A.; Kunttu, H.M. *J. Chem. Phys.* **1993**, *98*, 3914.
8. Andrews, L; Prochaska, T.; Ault, B.S *J. Am. Chem. Soc.* **1979**, *101*, 9.
9. Carver, T. G.; Andrews, L. *J. Chem. Phys.* **1969**, *50*, 4235.
10. Rogers, E.E.; Abramowitz, S.; Jacox, M.E.; Milligan, D.E. *J. Chem. Phys.* **1970**, *52*, 2198.
11. Jacox, M.E.; Milligan, D.E. *J. Chem. Phys.* **1971**, *54*, 3935.
12. Jacox, M. E.; Milligan, D. E. *J. Chem. Phys.* **1970**, *53*, 2688.
13. Jacox, M. E.; Milligan, D. E. *J. Chem. Phys.* **1967**, *47*, 1626.
14. Zhang, X.K.; Parnis, J.M.; Lewars, E.G.; March, R.E. *Can. J. Chem.* **1997**, *75*, 276.
15. Jacox, M.E. *Rev. Chem. Intermed.* **1978**, *2*, 1.
16. Lewars, E.G. *J. Mol. Struct.* **1998**, *425*, 207.
17. Jackson, A; Angon, G. *Chem. Brit.* **1993**, *29*, 1046.
18. Chen, H.; Holmes, J.L. *Int. J. Mass Spectrom. Ion Processes* **1994**, *133*, 111.
19. Chen. H., M.Sc. Thesis, University of Ottawa, Ottawa, Ontario, 1992.

20. a) Mincu, I.; Allouche, A.; Cossu, M.; Aycard, J. P.; Pourcin, J. *Spectrochim. Acta.*, **1995**, *51A*, 349. b) Hisatsune, I. C.; Heicklen, J. *Can. J. Spectrosc.*, **1973**, *18*, 77.

21. Schnöckel, H.; Eberlein, R. A.; Plitt, H. S. *J. Chem. Phys.*, **1992**, *97*, 4.

22. Jacox, M. E.; Milligan, D. E. *J. Chem. Phys.*, **1965**, *43*, 866.

23. Davidovics, G.; Monnier, M.; Schroeder, W.; Verlaque, P.; Pourcin, J.; Bodot, H. *J. Mol. Struct.* **1989**, *197*, 213.

24. a) Charles, S. W.; Lee, K. O. *Trans. Faraday Soc.*, **1965**, *61*, 614. b) Leroi, G. E.; Ewing, G. E.; Pimentel, G. C. *J. Chem. Phys.* **1964**, *40*, 2298.

25. Unless otherwise stated, all thermochemical data are taken from Lias, S. G.; Bartess, J. E.; Liebman, J. F.; Holmes, J. L.; Levin, R. D.; Mallard, W. *J. Phys. Chem. Ref. Data*, **1988**, *17*, Supp. 1.

26. Nicovich, J. M.; Kreutter, K. D.; Wine, P. H. *J. Chem. Phys.* **1990**, *92*, 3539.

27. Stevenson, D. P. *Discuss. Faraday. Soc.* **1951**, *10*, 35.

28. Katrib, A.; Debies, T. P.; Colton, R. J.; Lee, T. H.; Rabalais, J. *W. Chem. Phys. Lett.* **1973**, *22*, 196.

29. Thomas, R. K.; Thompson, H. *Proc. Roy. Soc. Lond.* **1972**, *A327*, 13.

30. Milligan, D.E.; Jacox, M.E. *J. Chem. Phys.* **1967**, *47*, 278.

31. Raine, G. P.; Schaefer, H. F.; Haddon, R. C. *J. Am. Chem. Soc.* **1993**, *105*, 194.

32. Milligan, D. E.; Jacox, M. E. *J. Chem. Phys.* **1969**, *51*, 277.

33. Jacox, M. E.; Milligan, D. E. *J. Chem. Phys.* **1970**, *53*, 2688.

34. Kenty, C. *Phys. Rev.* **1962**, *126*, 1235.

35. Worthing, A. G.; Rudy, R. *Phys. Rev.* **1924**, *23*, 767.

36. Porter, J. C.; Beynon, J. H.; Ast, T. *Org. Mass Spectrom.* **1981**, *16*,101.

37. Melton, C. E. *J. Chem. Phys.*, **1960**, *33*, 647.

38. a) Knight, L.B. Jr. *Acc. Chem. Res.* **1996**, *19*, 313. b) Knight, L.B. Jr.; Kerr, K.; Villanueva, M.; McKinley, A.J.; Feller, D. *J. Chem. Phys.* **1992**, *97*, 5363.

39. Schwentner, N.; Himpsel, F.J.; Saile, V.;Skibowski, M.; Steinmann, W.; Koch, E.-E. *Phys. Rev. Lett.* **1975**, *34*, 528.

40. Ophir, Z.; Raz, B.; Jortner, J.; Saile, V.; Schwentner, N.; Koch, E.-E.; Skibowski, M.; Steinmann, W. *J. Chem. Phys*, **1975**, *62*, 650.

41. Schwentner, N.; Koch, E.-E.; Jortner, J., *Electronic Excitations in Condensed Rare Gases (Chapter 3)*, **1985**, Springer-Verlag, Berlin.

42. de Rege, P.J.F.; Gladysz, J.A.; Horváth, I.T. *Science* **1997**, *276*, 776.

43. a) Vacek G.; Galbraith, J. M.; Yamaguchi, Y.; Schaefer, H. F.; Nobes, R. H.; Scott, A. P.; Radom, L. *J. Phys. Chem.* **1994**, *98*, 8660. b) Hop, C. E. C. A.; Holmes, J. L.; Terlouw, J. K. *J. Am. Chem. Soc.* **1989**, *111*, 441. c) Bouma, W. J.; Gill, P. M. W.; Radom, L. *Org. Mass. Spectrom.* **1984**, *19*, 610.

44. a) McGibbon, G. A.; Burgers, P. C.; Terlouw, J. K. *Int. J. Mass. Spectrom. Ion Processes.* **1994**, *136*, 191. b) Hop, C. E. C. A.; Chen, H.; Ruttink, P. J. A.; Holmes, J. L. *Org. Mass Spectrom.* **1991**, *26*, 679.

Chapter 4

Electron Bombardment Matrix Isolation of Rg/Rg'/Methanol Mixtures (Rg= Ar, Kr, Xe): FTIR Characterization of the Proton-Bound Dimers Kr_2H^+, Xe_2H^+, $(ArHKr)^+$ and $(ArHXe)^+$ in Ar Matrices and $(KrHXe)^+$ and Xe_2H^+ in Kr Matrices[A]

4.1 Introduction

Proton-bound rare-gas dimers, Rg_2H^+ where Rg=Ar, Kr, or Xe are fundamental species in rare-gas matrices and as such have been the subject of extensive experimental investigations for quite some time in the gas phase by mass spectrometric techniques[1,2,3,4] and in the condensed phase by FTIR coupled with matrix isolation.[5,6,7,8,9] These ions have also received much attention from theoreticians and predictions of their thermodynamic properties, geometric

---

[A] This chapter is a modified version of the manuscript published as T.D. Fridgen and J. Mark Parnis, *J. Chem. Phys*, **1998**, *109*, 2155.

structures, and vibrational wavenumbers have been made at various levels of *ab initio* theory[4,10,11,12,13] and with DFT methods. [14,15] As well, attempts to explain the thermal instability of these species in rare-gas matrices have been made.[12]

The first spectroscopic evidence for Rg_2H^+ species came in 1972 when Bondeybey and Pimentel[5] passed rare-gas/hydrogen mixtures through a glow discharge and immediately condensed the discharge gas on a CsI window at 15 K. The IR spectra revealed features at 905 cm^{-1}, 852 cm^{-1}, 644 cm^{-1}, or 607 cm^{-1} when the rare-gas/hydrogen mixture was Ar/H_2, Kr/H_2, Ar/D_2, or Kr/D_2, respectively. These absorptions were assigned to H (or D) 'atoms' trapped in octahedral hole O_h interstitial sites in the solid rare gas. Later, Milligan and Jacox[6] reassigned the features to the ionic species Rg_nH^+ but were unable to determine the number of rare-gas atoms in the species. The assignment to an ionic species was confirmed by Wight *et al.*[7] who observed these features only when photons of sufficient energy to produce protons impinged upon an argon matrix containing hydrogen atoms.

In 1992, Kunttu *et al.*[8] provided compelling evidence that the Rg_nH^+ cations, produced by irradiating HX-doped rare-gas matrices (X=halogen), were linear centrosymmetric triatomic species, Rg_2H^+. This conclusion was reached after observing the $v_3 + nv_1$ combination band progression in the vibrational spectrum of Xe_2H^+. This progression matched qualitatively those originating from the isoelectronic bihalide anion I_2H^-.[16] Furthermore, Kunttu *et al.*[8] noted a general parallel between the combination band progressions observed for all X_2H^- ions[16,17] (X=Cl, Br, I) and those observed for all Rg_2H^+ species.[9,12] Reports from mass-spectrometric studies have suggested that gas-phase reactions with Ar_2^+, Ne_2^+ or

He_2^+ with H_2 most probably results in the asymmetric structure $RgRgH^+$, but that the gas-phase reaction between ArH^+ and Ar in a three-body collision likely produces the more stable symmetric cation. However, no concrete evidence of this has been provided.[3,4] Theoretical papers pertaining to these species confirm the assignment of the observed infrared absorptions in rare-gas matrices to the linear centrosymmetric triatomic cations. More recently, Kunttu and Seetula[9] performed in-depth studies of the thermal decay kinetics of Ar_2H^+, Kr_2H^+ and Xe_2H^+ in Ar, Kr and Xe matrices, respectively. By plotting the area under the dimer bands against time, they succeeded in determining that the decay of these bands is second order. Second-order rate constants in units of s^{-1} absorbance^{-1} were obtained. The observed second-order decay is presumably due to the fact that the rare-gas cations are being neutralized in the matrix which requires the presence of a neutralization agent.

None of the studies cited above have reported experimental observation of mixed rare gas species $(RgHRg')^+$ where $Rg \neq Rg'$, despite *ab initio* and DFT calculations[14,15] which predict these mixed rare-gas cations to be stable species. Similarly, there are no reports of the spectra of the pure rare-gas cations (Rg_2H^+) in a matrix composed of a different rare gas (for example Kr_2H^+ in an argon matrix). Reported in this chapter are the matrix infrared spectra of Kr_2H^+, Kr_2D^+, Xe_2H^+, Xe_2D^+, in predominantly argon environments as well as Xe_2H^+ and Xe_2D^+ in primarily krypton environments. Also reported are the matrix infrared spectra of the mixed rare-gas cations, $(ArHKr)^+$ and $(ArHXe)^+$ isolated in a predominantly argon matrix and $(KrHXe)^+$ isolated in a predominantly krypton matrix. The observed infrared

spectra are also compared to results of DFT calculations from chapter 5.[15] The most probable routes to formation of these species from electron bombardment and subsequent matrix isolation of Rg/Rg'/methanol mixtures are also discussed.

4.2 Experimental Details

The electron bombardment matrix isolation (EBMI) technique has been described in detail in chapter 2; a brief summary is given here. An electron beam emanated from a thoriated tungsten filament and was accelerated through 300 V towards an anode doubling as a Faraday plate to monitor the electron current. Methanol vapor (or other precursor where specified) was diluted in rare-gases in the mole ratio of 1 part in 400. This mixture was condensed on the 15 K CsI substrate at a flow rate of 1.00 sccm. Just prior to condensation, the gas mixture crossed the electron beam at 90°. The entire apparatus was kept at 10^{-7} torr using a diffusion pump charged with Si-based oil. Typical deposition times were 3 h unless otherwise noted. By temperature measurements made immediately after the deposition was completed, it was estimated that the temperature during deposition was 17-18 K. After this period of EBMI, an FT-IR spectrum was recorded and compared with a spectrum taken under the same conditions except with the electron source turned off. The matrix could be heated to specified temperatures in order increase the energy of the matrix isolated species and to allow diffusion of species throughout the matrix in order to aid in spectroscopic characterization.

Methanol (CD_3OD, 99.95+ atom % D; CD_3OH, 99 atom % D; HPLC Grade CH_3OH; and $^{13}CH_3OH$, 99 atom % ^{13}C - all purchased from Aldrich) and CD Cl_2

(99.6 atom % D) were degassed by a series of freeze-pump-thaw cycles before use. Prepurified argon, research-grade krypton, and research-grade xenon were purchased from Matheson Canada or Praxair and used without further purification.

4.3 Results and Discussion

4.3.1 EBMI of Methanol Diluted in Ar, Kr or Xe

FT-IR spectra recorded after EBMI of 1 in 400 CH_3OH diluted in either pure Ar, Kr or Xe showed that 2/3 to 3/4 of the methanol precursor was destroyed, based upon changes in the intensities of the CH stretching mode (3666 cm^{-1}) or COH bending mode (864 cm^{-1}) of methanol. New features were observed following EBMI and assigned to the neutral decomposition products CO, HCO, H_2CO, and H_2COH as is seen in Figure 4.1a. These assignments were confirmed by performing the same experiments with CD_3OD or $^{13}CH_3OH$ as the precursor (see Fig. 4.1b and 4.1c respectively). When the precursor was CD_3OH, similar results were also obtained but it should be noted that various isotopomers of the hydrogenic species were present. This scrambling may reflect one or more hydrogen-shift isomerization processes prior to the decomposition or reaction of the molecular cation or its fragments. The products identified in the CD_3OH experiments were (including isotompomers) HCO, DCO, HDCO, D_2CO, D_2COH and D_2COD. The fact that no bands assignable to the organic cations can be ascribed to the inability of these doped-argon matrices to trap ions. The inability of some matrices to trap high electron-affinity ions is discussed in detail in chapter 3 (section 3.5).

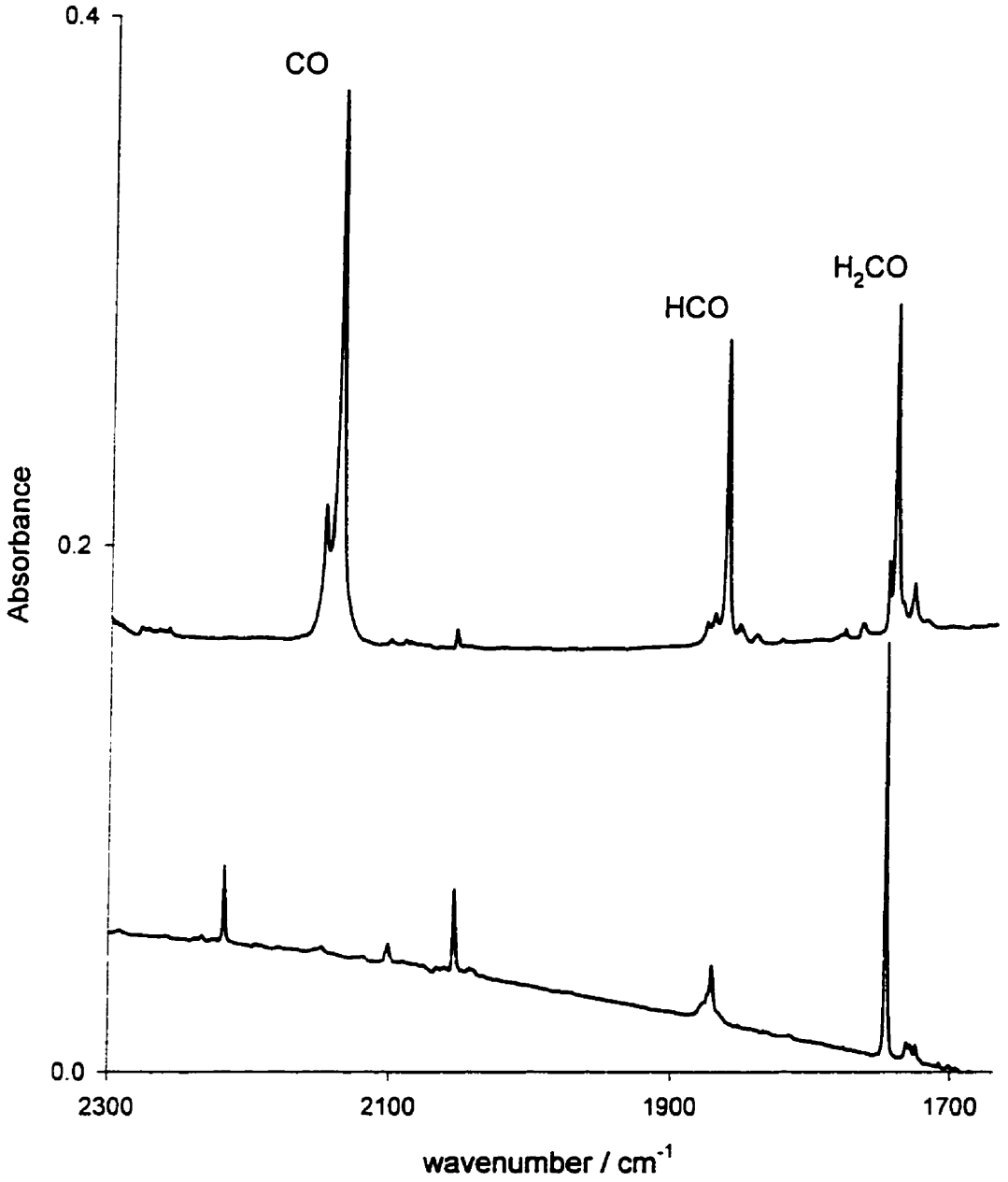

Figure 4.1a). Portion of the infrared spectra taken after 3 h of straight deposition (bottom trace) and after 3 h of gas-phase electron bombardment and subsequent matrix isolation of a 1/400 CH_3OH/Ar mixture.

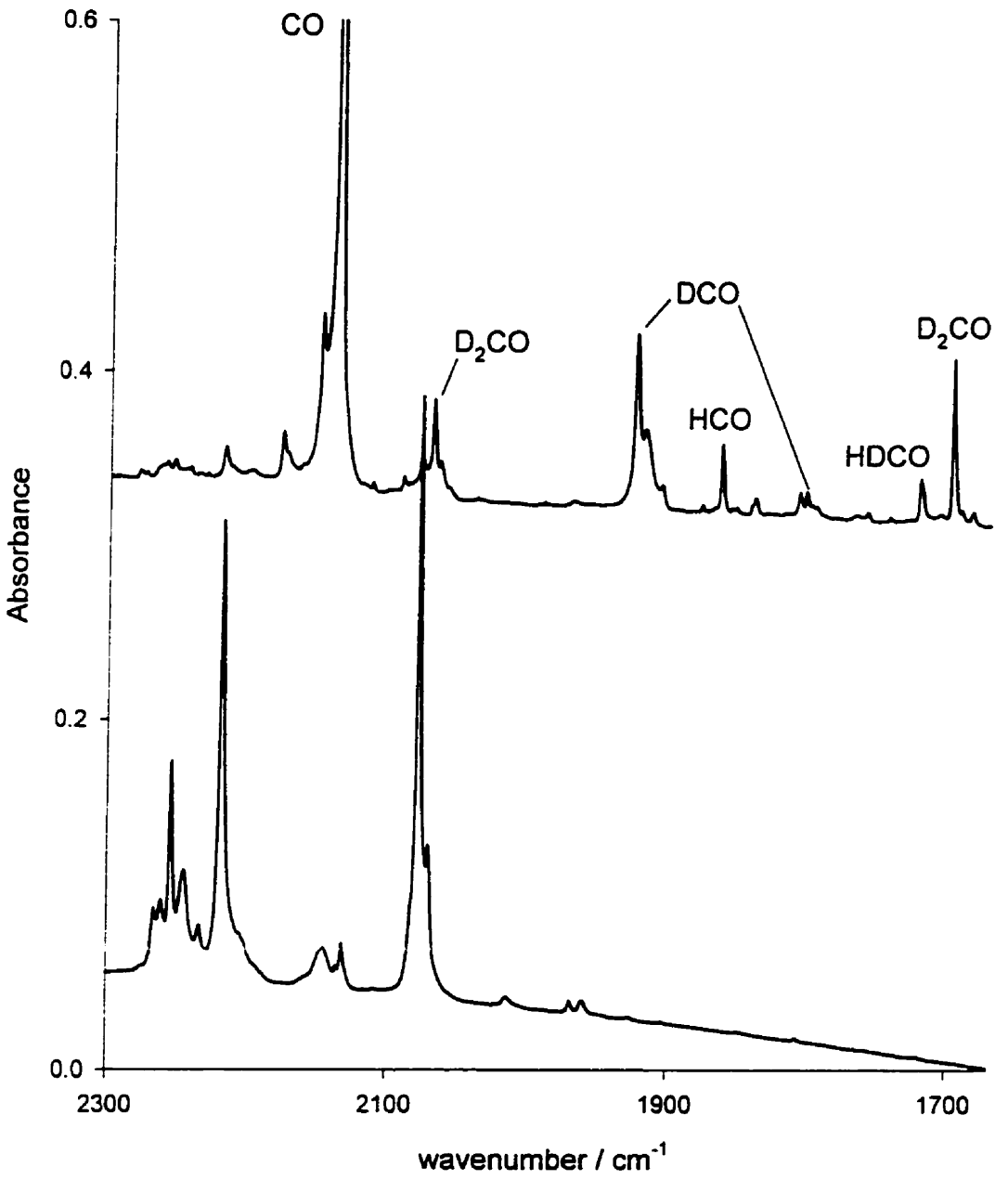

Figure 4.1b). Portion of the infrared spectra taken after 3 h of straight deposition (bottom trace) and after 3 h of gas-phase electron bombardment and subsequent matrix isolation of a 1/400 CD_3OD/Ar mixture.

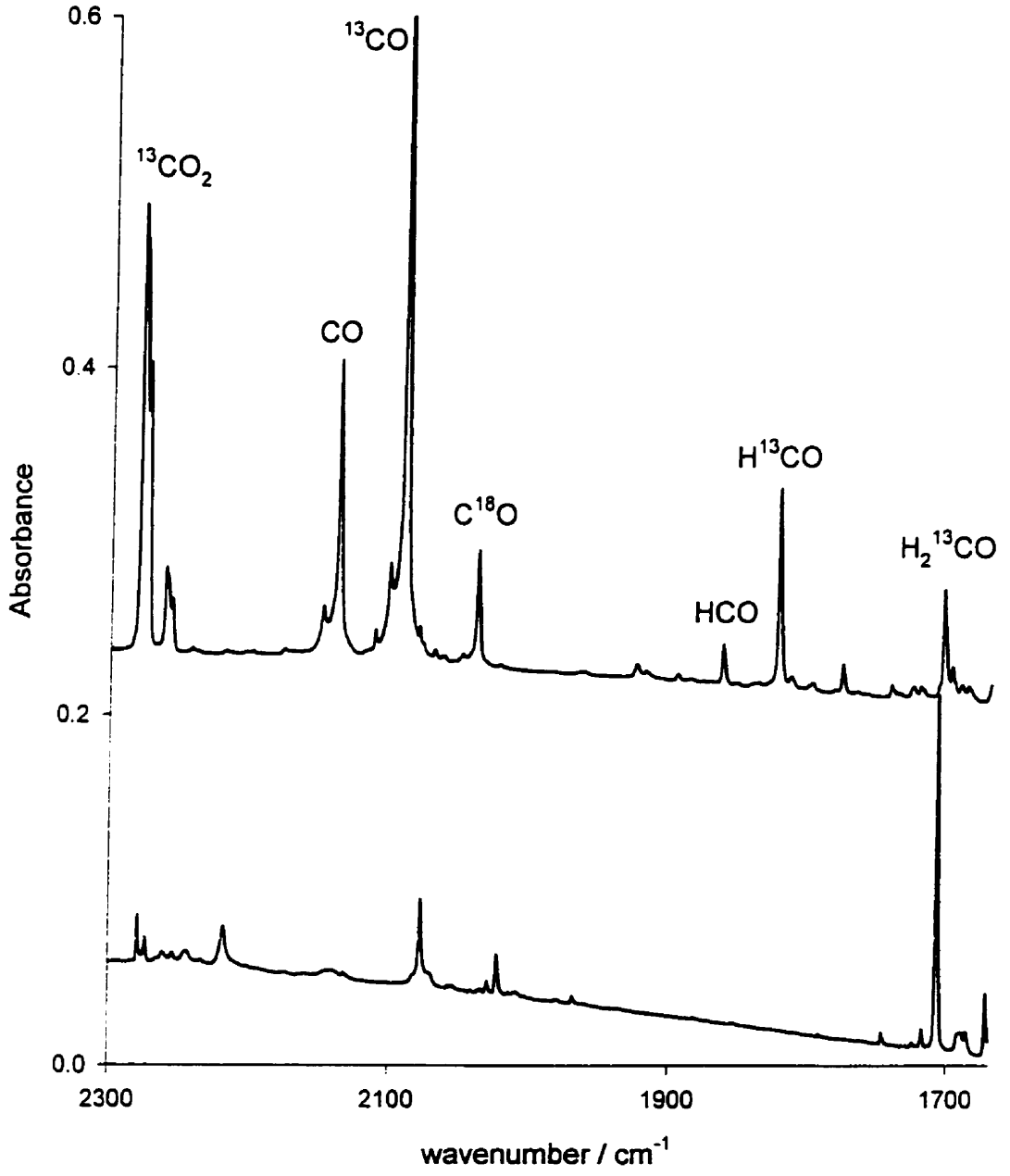

Figure 4.1c). Portion of the infrared spectra taken after 3 h of straight deposition (bottom trace) and after 3 h of gas-phase electron bombardment and subsequent matrix isolation of a 1/400 $^{13}CH_3OH$/Ar mixture.

The only ions which were identified in these experiments were the well-known Ar_2H^+, Kr_2H^+, Xe_2H^+ and their deuterium analogues. When the precursor was CD_3OH the infrared spectrum revealed features associated with both isotopomers except for the krypton case where Kr_2H^+ could not be identified due to spectral interference from a strongly-absorbing precursor band. The $\nu_3 + n\nu_1$ combination band progressions were also observed for these species and were in excellent agreement with previously-reported assignments.[9]

EBMI experiments conducted in which the methanol concentration was varied from 0.1 % to 0.125, 0.25 or 0.5 % in Ar revealed that, on increasing the methanol concentration, the fraction of methanol destroyed decreased quite dramatically over this range as is seen in Figure 4.2. This observation can be explained in terms of quenching as was discussed in chapter 3. The newly-formed methanol radical cation has associated with it an abundance of energy, from the ionization process, which enables its decomposition. Methanol itself can act as a quenching agent to soak up some of this excess internal energy. Therefore, increasing the amount of methanol precursor in the gas mixture effectively increases the amount of quenching agent and decreases the fraction of methanol destroyed.

4.3.2 EBMI of Methanol Diluted in Ar/Kr, Ar/Xe or Kr/Xe Mixtures

In the following sections, results of EBMI experiments in which methanol (or other precursor where noted) was diluted with a mixture of rare gases will be discussed. In the following discussion, Rg'/Rg is the mole ratio of the heavier rare-

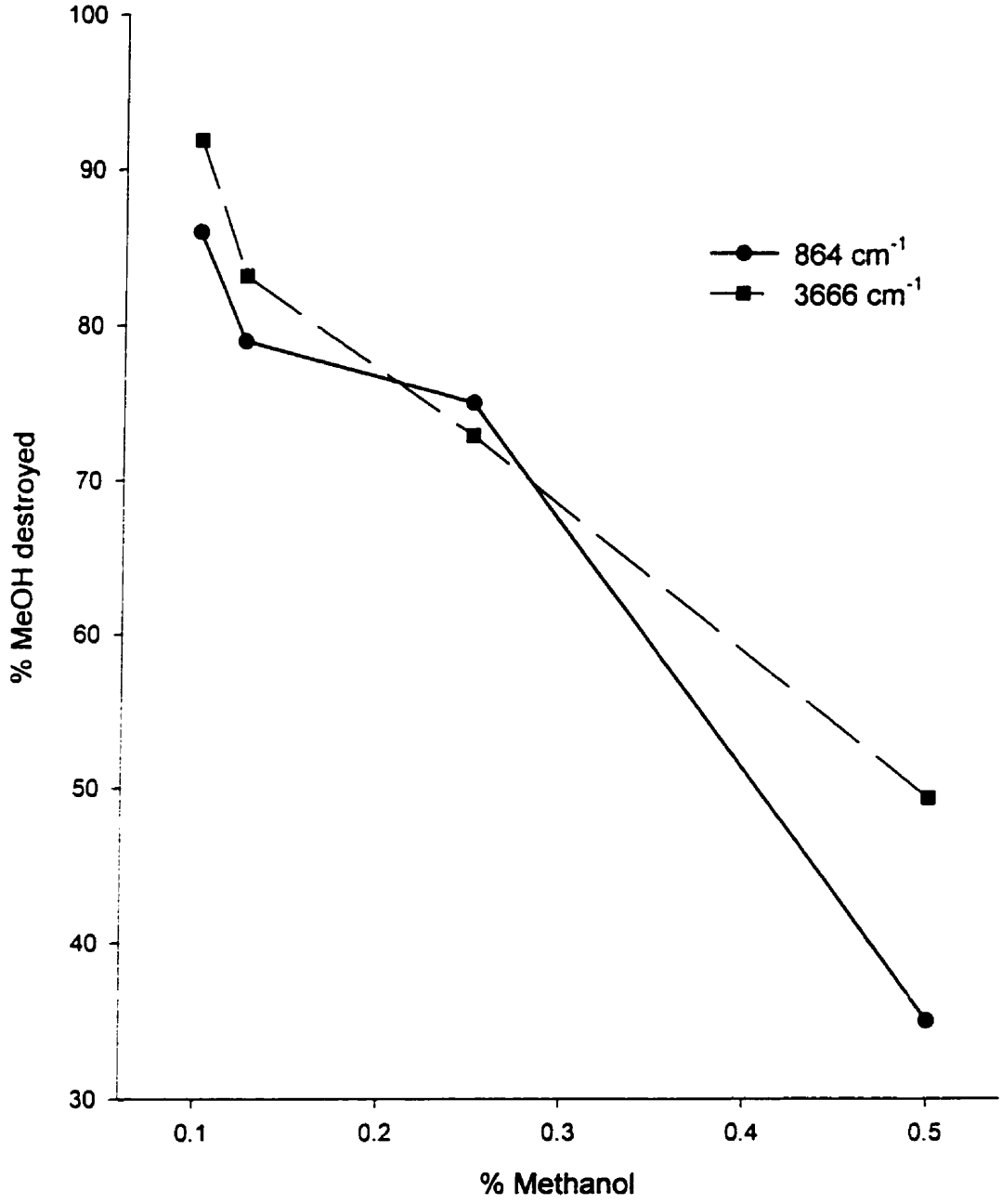

Figure 4.2. Plot of the % of methanol destroyed versus the % methanol in the original methanol/argon gas mixture. The % methanol destroyed was calculated by dividing the area under the absorption features (OH stretch ■ or COH bend ●) after gas-phase electron bombardment and subsequent matrix isolation by the area under the same feature after straight deposition.

gas Rg' in the original gas mixture.

4.3.2.1 Krypton/Argon Experiments

After EBMI of methanol diluted in a mixture of argon and krypton where the ratio Kr/Ar was as low as 0.004 (1 part in 250), a new feature in the infrared spectrum was observed at 885.3 cm^{-1}. This is between the wavenumbers at which Ar_2H^+ and Kr_2H^+ are observed in argon and krypton matrices, respectively. This band increased in intensity as Kr/Ar ratio was increased with concurrent depletion of the Ar_2H^+ feature. At a Kr/Ar ratio of 0.053, the Ar_2H^+ feature had fully vanished as shown in Fig. 4.3. The intensity of the new feature reached a maximum at a Kr/Ar ratio of 0.100 and was not observed after the Kr/Ar ratio reached 0.40. In similar experiments when CD_3OD was used as the precursor instead of CH_3OH, a new absorption at 628.7 cm^{-1} was observed. Similar to the CH_3OH experiments, this feature is observed at a wavenumber between those assigned to Ar_2D^+ and Kr_2D^+. In annealing experiments, these new features at 885.3 cm^{-1} and 628.7 cm^{-1}, in the hydrogen and deuterium experiments, respectively, decreased in intensity over time, displaying behaviour similar to those assigned to Ar_2H^+ and Kr_2H^+ and their deuterated isotopomers.

None of these new features were observed when Ar/Kr mixtures were submitted to EBMI without any precursor and must, therefore, be due to a molecule or ion containing one or more of H, C, or O. It is certain from the D-isotopomer results that the new feature is due to a species containing H since the ν_H/ν_D ratio is 1.408, very close to the ν_H/ν_D ratios of Ar_2H^+/Ar_2D^+ and Kr_2H^+/Kr_2D^+ of 1.404 and 1.407, respectively. The same new feature at 885.3 cm^{-1} was observed when

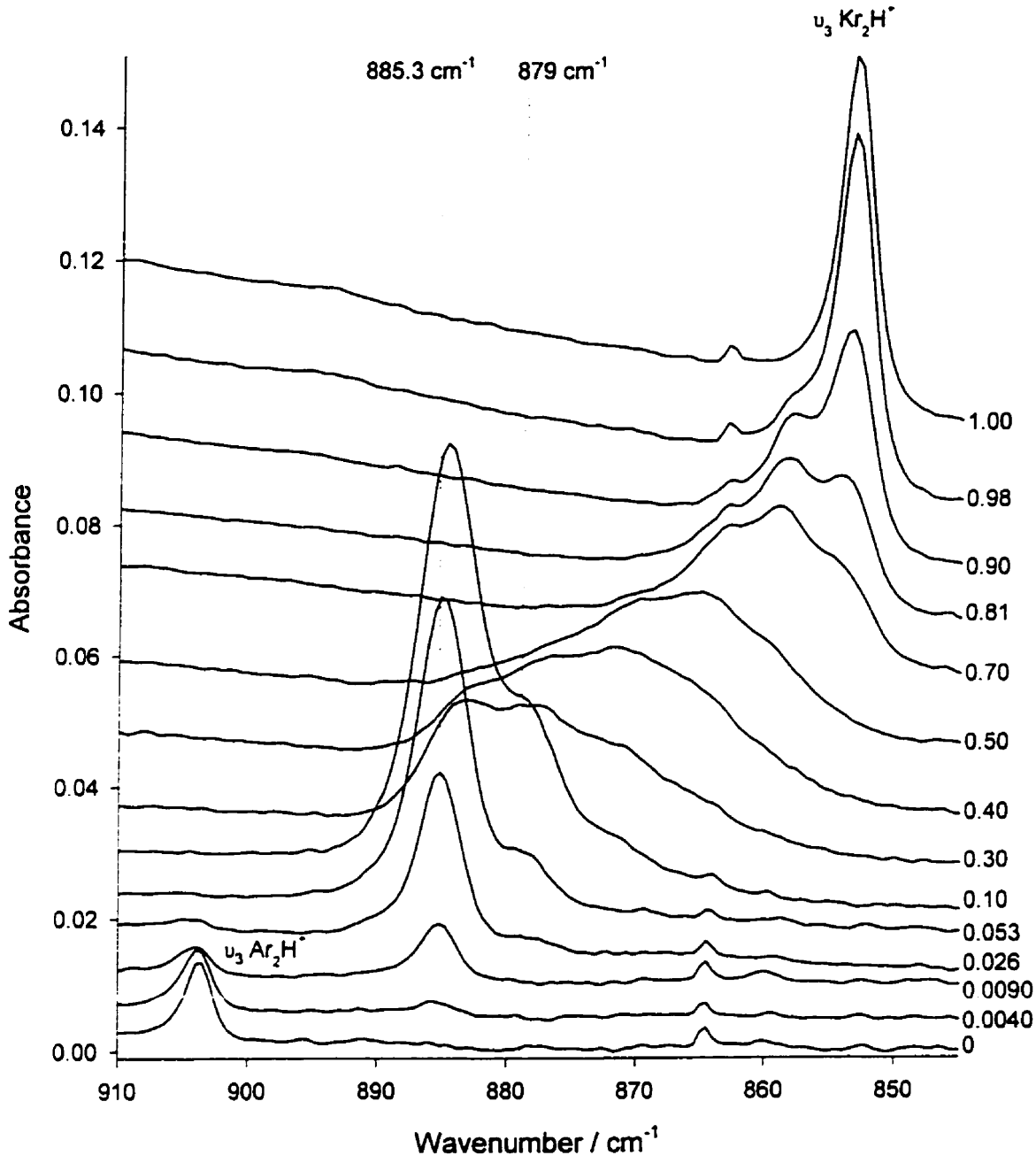

Figure 4.3. Portion of the FT-infrared spectra in the region of the antisymmetric stretches of Ar_2H^+ and Kr_2H^+ recorded after 3 h of EBMI of methanol vapour diluted in krypton/argon mixtures. The bands at 885.3 cm^{-1} and 879 cm^{-1} which are assigned to $(ArHKr)^+$ and Kr_2H^+, respectively, isolated in predominantly argon environments are noted with wavenumber markers. The values to the right of each trace are the Kr/Ar ratios of the diluent gas.

$^{13}CH_3OH$ was used as the precursor showing no ^{13}C isotopic shift. It is not expected, therefore, that the species responsible for the new features contains carbon. Previous studies[18] on the EBMI of CD_2Cl_2 have also yielded absorptions due to Ar_2D^+, and it has subsequently been verified that use of CD_2Cl_2 as a precursor yielded a 629.2 cm^{-1} absorption when the diluent gas had a Kr/Ar ratio of 0.10. It is therefore confirmed, as well, that the new feature is not due to an oxygen-containing species.

The results which have been presented so far suggest strongly that the carrier of the 885.3 cm^{-1} band is a proton-bound rare-gas dimer and the band at 628.7 cm^{-1} is due to its deuterated isotopomer. As well, at least one of these rare-gas atoms is likely to be Kr, since there is such a pronounced shift in wavenumber from the observed Ar_2H^+ absorbance at very low Kr/Ar ratio. The new feature at 885.3 cm^{-1} present at a Kr/Ar ratio between 0.004 and 0.40 has associated with it a red-shifted shoulder at about 879 cm^{-1} when the Kr/Ar ratio is greater than 0.10. A corresponding shoulder is observed at 625 cm^{-1} in the deuterium isotope experiments. It is evident from Fig. 4.3 that the main band at 885.3 cm^{-1} decreases in intensity as the Kr/Ar ratio increases beyond 0.10, with the shoulder band broadening and shifting significantly to the red, ultimately sharpening and dominating the spectrum at very high levels of Kr. The shifting of this shoulder feature correlates with increasing concentrations of Kr in the matrix, likely reflecting increasing degrees of stabilization of the absorber by the increasingly-polarizable matrix environment.

The features at 885.3 cm^{-1} and 879 cm^{-1} can be distinguished by their

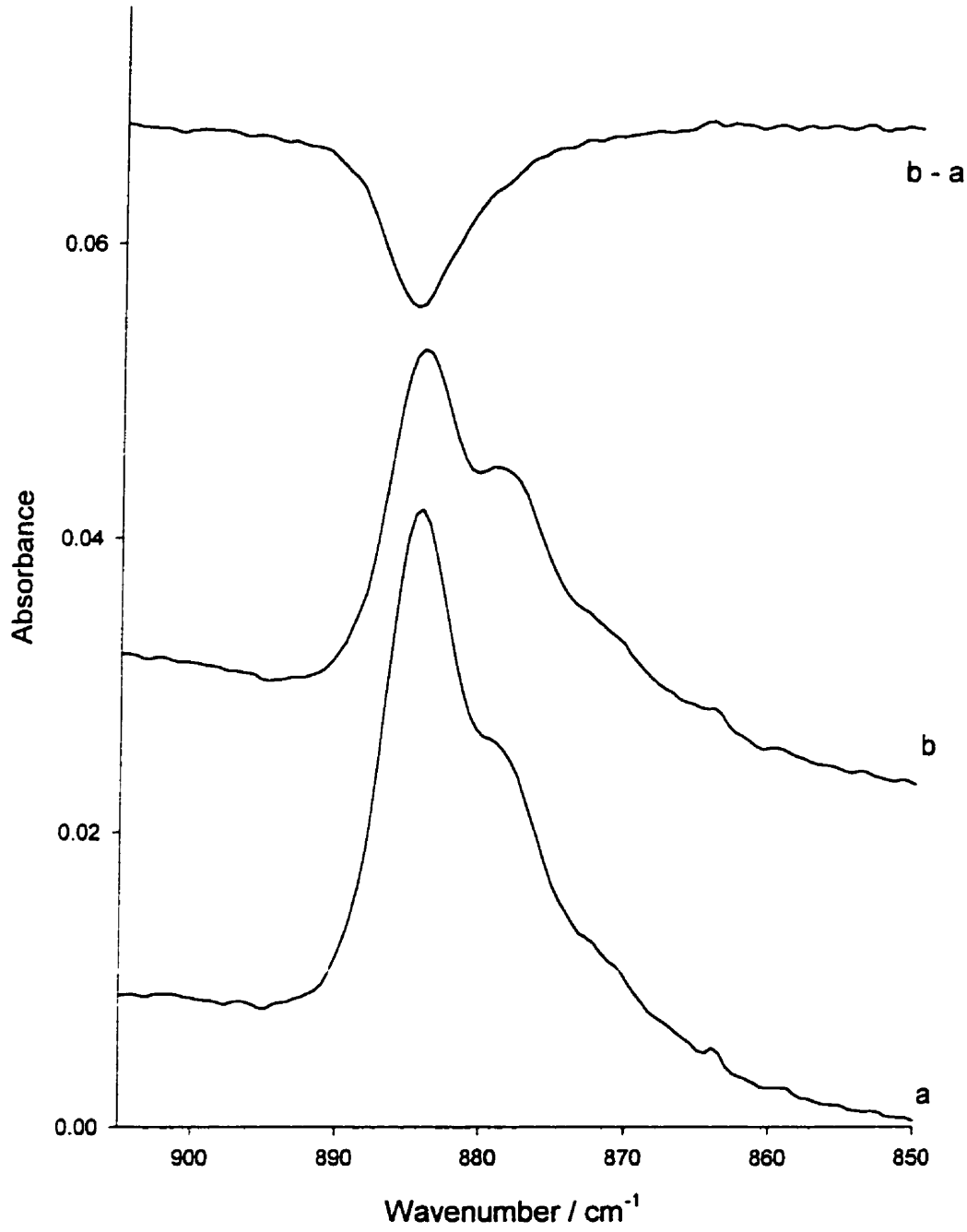

Figure 4.4. Portion of the FTIR spectrum taken (a) after 3 h EBMI of CH_3OH diluted in Ar and Kr, Kr/Ar=0.20 b) and after 11 h annealing at 20 K. The top trace is the difference spectrum, b) - a).

behaviour during annealing, as illustrated in Fig. 4.4 for a matrix containing CH_3OH diluted in a mixture of argon and krypton with a Kr/Ar ratio of 0.20 after EBMI. A preferential disappearance of the main feature at 885.3 cm^{-1} is clearly seen, with no loss of the 879 cm^{-1} shoulder. If both features were due to the same carrier (i.e. Kr_2H^+) in slightly different matrix environments, it would be expected that both would be subject to the same extent of decay on annealing, or that decay of the less stable site would result in growth of the ion in the more stable site as discussed in Chapter 1. The absence of growth of the 879 cm^{-1} feature on loss of that at 885.3 cm^{-1} appears to rule out isomer or site interconversion as a mechanism for loss of the latter. Similarly, thermal annealing of matrices in which both Ar_2H^+ and the 885.3 cm^{-1} were present show Ar_2H^+ to be more sensitive than the absorber responsible for the new feature.

The likely mechanism for thermal bleaching of these species involves thermally-induced diffusion of the proton or hole and subsequent neutralization following recombination with a suitable anionic species or electron trap within the solid matrix, as was initially proposed by Kunttu and Seetula.[9] In this context, one would conclude that the carrier of 885.3 cm^{-1} band has a higher hole or proton affinity than Ar_2H^+ and a lower hole or proton affinity than the carrier of the 879 cm^{-1} shoulder. Recognizing that two krypton atoms would have a higher affinity for an electron hole or proton than an argon/krypton pair, it would be expected that the hole or proton would be more deeply bound on Kr_2 than ArKr. The feature at 885.3 cm^{-1} is, therefore, assigned to the mixed rare-gas species $(ArHKr)^+$ and the shoulder at 879 cm^{-1} to Kr_2H^+, both in an essentially pure argon environment. These

assignments are consistent with and in general agreement with the previously-reported observation of the increasing stability of Rg_2H^+ species with the mass of Rg.[9] The observed shifting, broadening and ultimate sharpening of the 879 cm^{-1} feature can then be understood as being due to Kr_2H^+ in an increasingly polarizable environment as the level of Kr increases, with a concomitant shift in the absorption wavenumber associated with increased stabilization of the ion in the matrix cage.

These assignments are also supported by the calculated vibrational wavenumbers reported in the next chapter.[15] The calculated (and scaled) wavenumbers from that work are presented in Table 4.1 with the argon-matrix observed values. The scaling factor 0.7414 was obtained by dividing the observed wavenumber of the antisymmetric stretch by the calculated value. The scaled values for Ar_2H^+, $(ArHKr)^+$ and Kr_2H^+ predict that their ν_3 fundamentals all fall within 28 cm^{-1}. More importantly, there is quite good agreement between the argon-matrix scaled and the argon-matrix observed wavenumbers supporting the assignments made above to the 885.3 cm^{-1} and 879 cm^{-1} bands.

4.3.2.2 Xenon/Argon Experiments

In Fig. 4.5 are shown the results of experiments where mixtures of CH_3OH diluted in argon and xenon are submitted to EBMI. At very low Xe/Ar ratios two new features grow in with maxima in intensities at 828.1 cm^{-1} and 952.5 cm^{-1} with concurrent depletion of the Ar_2H^+ feature. These relatively sharp bands are not observed above a Xe/Ar ratio of 0.049 but instead very broad bands centred at 796 cm^{-1} and 910 cm^{-1} are observed. These broad features increase considerably in intensity up to approximately a Xe/Ar ratio of 0.50 then decrease and broaden

Table 4.1. Comparison between calculated wavenumbers and observed wavenumbers for Ar_2H^+, $ArHKr^+$, Kr_2H^+ and their deuterated isotopomers in predominantly argon matrices.

Species	Scaled[a] ω_3 / cm^{-1}	Observed ν_3 / cm^{-1}	$\omega_3 - \nu_3$ / cm^{-1}
Ar_2H^+	903.8	903.8	0
$ArHKr^+$	891.9	885.3	6.6
Kr_2H^+	876.3	879.0	-2.7
Ar_2D^+	642.8	643.7	-0.9
$ArDKr^+$	633.9	628.7	6.2
Kr_2D^+	622.0	625.0	-3.0

a: Calculated values of ν_3 from reference 15 were scaled by 0.7414 as discussed in the text.

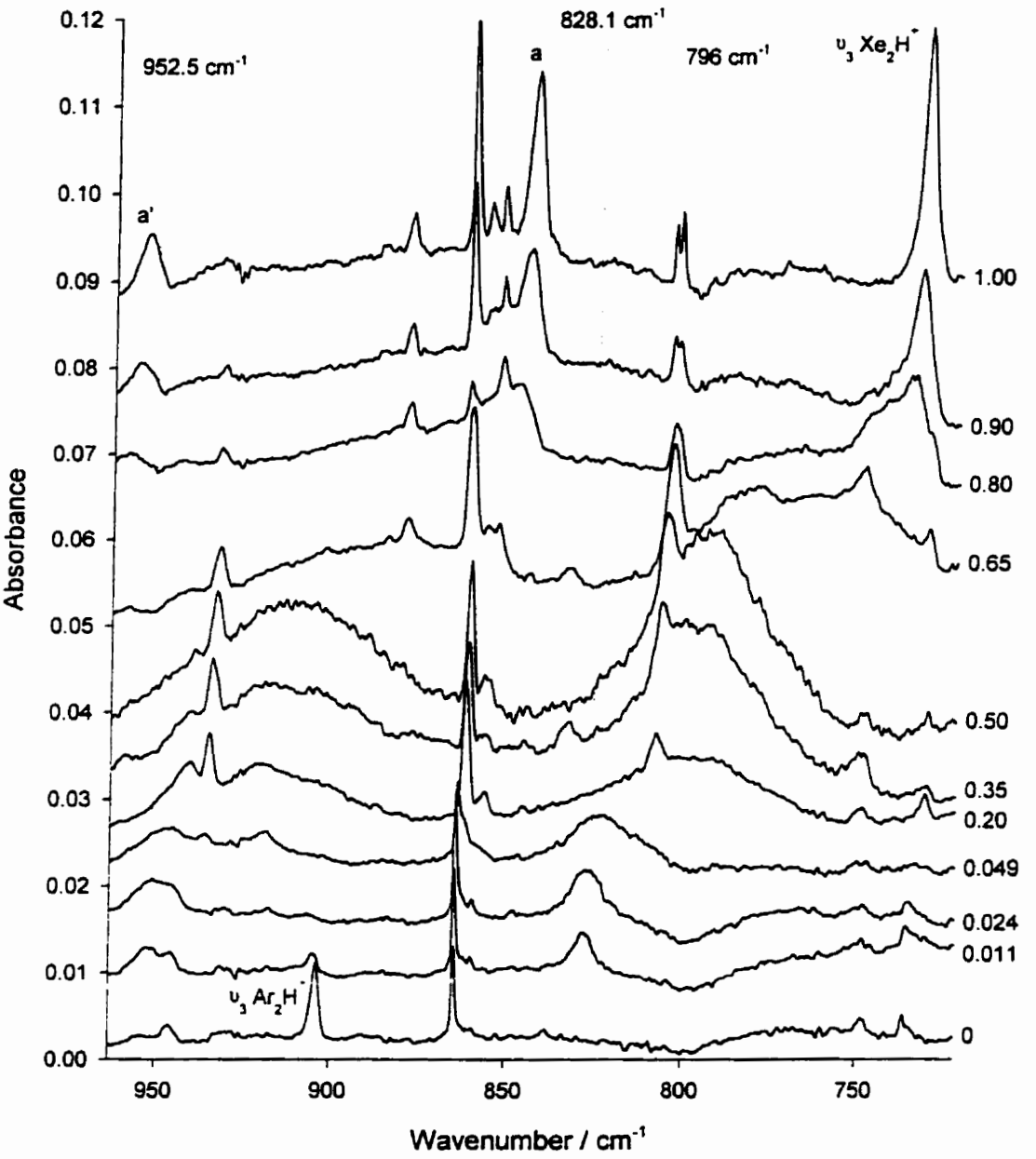

Figure 4.5. Portion of the FT-infrared spectra in the region 710 to 960 cm^{-1} recorded after 3h of EBMI of methanol vapour diluted in xenon/argon mixtures. The bands at 828.1 and 952 cm^{-1} are assigned to $(ArHXe)^+$ and at 796 cm^{-1} to Xe_2H^+ isolated in predominantly argon environments and are noted with wavenumber markers. The values to the right of each trace are the Xe/Ar ratios of the diluent gas. The bands marked a and a' have been previously assigned to combination bands of Xe_2H^+.

further with a concurrent shift in wavenumber. Increasing the Xe/Ar ratio past 0.80 results in sharpening of these features which converge at the previously assigned v_3 fundamental and $v_3 + v_1$ combination of Xe_2H^+.[8] Unfortunately, there are no acceptable calculated wavenumbers with which to compare these observed wavenumbers. Based on comparison of the behaviour of the new features in this system with the Ar/Kr system discussed in detail above, the 828.1 cm^{-1} band is assigned to the antisymmetric stretch (v_3) of the mixed rare-gas species $(ArHXe)^+$ isolated in a predominantly argon matrix. The 952.5 cm^{-1} feature is 124.4 cm^{-1} higher in energy than the v_3 band and is assigned to the $v_3 + v_1$ combination band of $(ArHXe)^+$. Also shown in the top trace of Fig. 4.5 is the v_3 band and the $v_3 + v_1$ (a) and $v_3 + 2\ v_1$ (a') combination bands of Xe_2H^+ which are separated, respectively, by 112 cm^{-1} and 110.6 cm^{-1}. The broad bands centred at 796 cm^{-1} and 910 cm^{-1} when the Xe/Ar ratio was greater than 0.20, separated by 114 cm^{-1}, are assigned to v_3 and $v_3 + v_1$ of Xe_2H^+ isolated in a predominantly argon environment.

4.3.2.3 Xenon/Krypton/Argon Experiments

When a 1 in 400 mixture of CH_3OH in Ar was doped with both Kr and Xe (where the Kr/Ar and Xe/Ar ratios were both less than 0.02) and was submitted to EBMI, the infrared spectra recorded subsequently revealed bands at 950.4 cm^{-1}, 828.3 cm^{-1}, *and* 885.2 cm^{-1} as are shown in Figure 4.6. These bands are the same ones as those seen in the above experiments and assigned to $(ArHKr)^+$ and $(ArHXe)^+$.

If the 885.3 cm^{-1} feature in the Kr/Ar experiments and the 952.5 cm^{-1} and 828

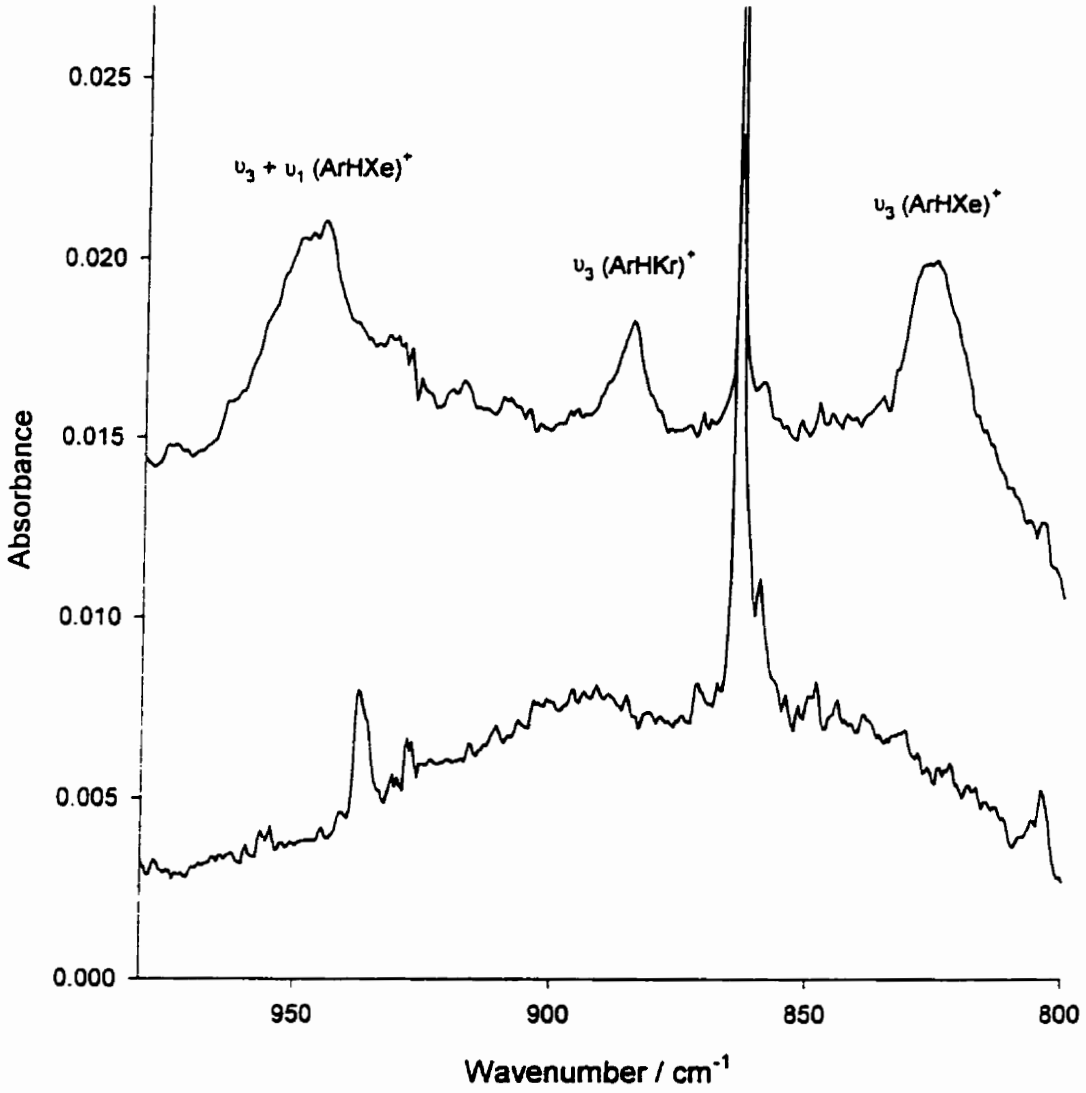

Figure 4.6. Portion of the FT-infrared spectra in the region 800 to 980 cm^{-1} recorded after 3 h EBMI (top trace) and upon straight deposition (bottom trace) of a 1 in 400 mixture of methanol vapor diluted in argon and 2 % each of krypton and xenon.

cm^{-1} features in the Ar/Xe experiments were due to simply Kr_2H^+ and Xe_2H^+, respectively, in predominantly argon environments, it would have to be concluded that krypton and xenon are extremely efficient in scavenging the charge centres or that the protons (or holes) are very mobile in the cryogenic rare-gas matrices and always migrate to two-krypton or two-xenon-atom sites even at a very low concentration of the heavier rare gas. Similarly, if the new bands assigned to $(KrHXe)^+$ in the experiments where krypton was doped with xenon (discussed in the next subsection) were simply due to Xe_2H^+ in a krypton environment, then xenon would also have to be a much more efficient charge scavenger than krypton or, again, the proton (hole) would have to always find a two-xenon-atom site. In addition, these processes would have to occur either in the gas phase or during condensation since it has been shown above that the carriers of the infrared features in question are quite stable to thermal annealing.

The results of the Xe/Kr/Ar experiments presented above are conclusive evidence that these scavenging processes are not occurring to any large extent since we would not have expected to see the 885.3 cm^{-1} $(ArHKr)^+$ band which is, without question, due to a krypton-containing species. This follows since efficient hole or proton scavenging by Xe would make formation of any Ar- or Kr-containing proton-bound rare-gas dimers highly improbable. The fact that it is observed in good yield in the presence of xenon demonstrates that the heavier rare-gas atom does not displace the lighter rare-gas atoms to any significant extent. This in consistent with findings that there is a significant barrier to hole or proton mobility once trapped by a Rg_2 site. The results of the Xe/Kr/Ar experiments are only

consistent with the assignments of the 885.3 cm^{-1} feature to $(ArHKr)^+$ and the 952.5 and 828.1 cm^{-1} features to $(ArHXe)^+$.

4.3.2.4 Xenon/Krypton Experiments

In Fig. 4.7 are shown the results of EBMI experiments of CH_3OH diluted in krypton and increasing amounts of xenon. Similar to the results above, new features at 781.7 and 900.3 cm^{-1} grow in at very low levels of xenon. These features disappear at higher Xe/Kr ratios and broad bands grow in at 765 cm^{-1} and 875 cm^{-1}. By comparison with the systems discussed above the former pair of bands are assigned to the v_3 and $v_3 + v_1$ fundamental and combination band of $(KrHXe)^+$ while the second pair are assigned to the same fundamental and combination band of Xe_2H^+ isolated in a predominantly Kr environment. Similar experiments with CD_3OD as the precursor yielded bands at 553.0 cm^{-1} and 538.1 cm^{-1} which are assigned to $(KrDXe)^+$ and Xe_2D^+, respectively, in predominantly krypton solids.

4.3.3 Mechanistic Considerations

Since the rare-gas atom Rg is in great excess in these EBMI experiments, the first step in the formation of Rg_2H^+ species is electron impact ionization of Rg. Charge transfer between $Rg^{\bullet+}$ and methanol would leave a methanol radical cation in a highly excited state (reaction 4.1), with the energy of excitation equal to the difference between the electron affinity (EA) of $Rg^{\bullet+}$ and the ionization potential (IP) of methanol (i.e. 473.7 kJ mol^{-1} for ionization with $Ar^{\bullet+}$),

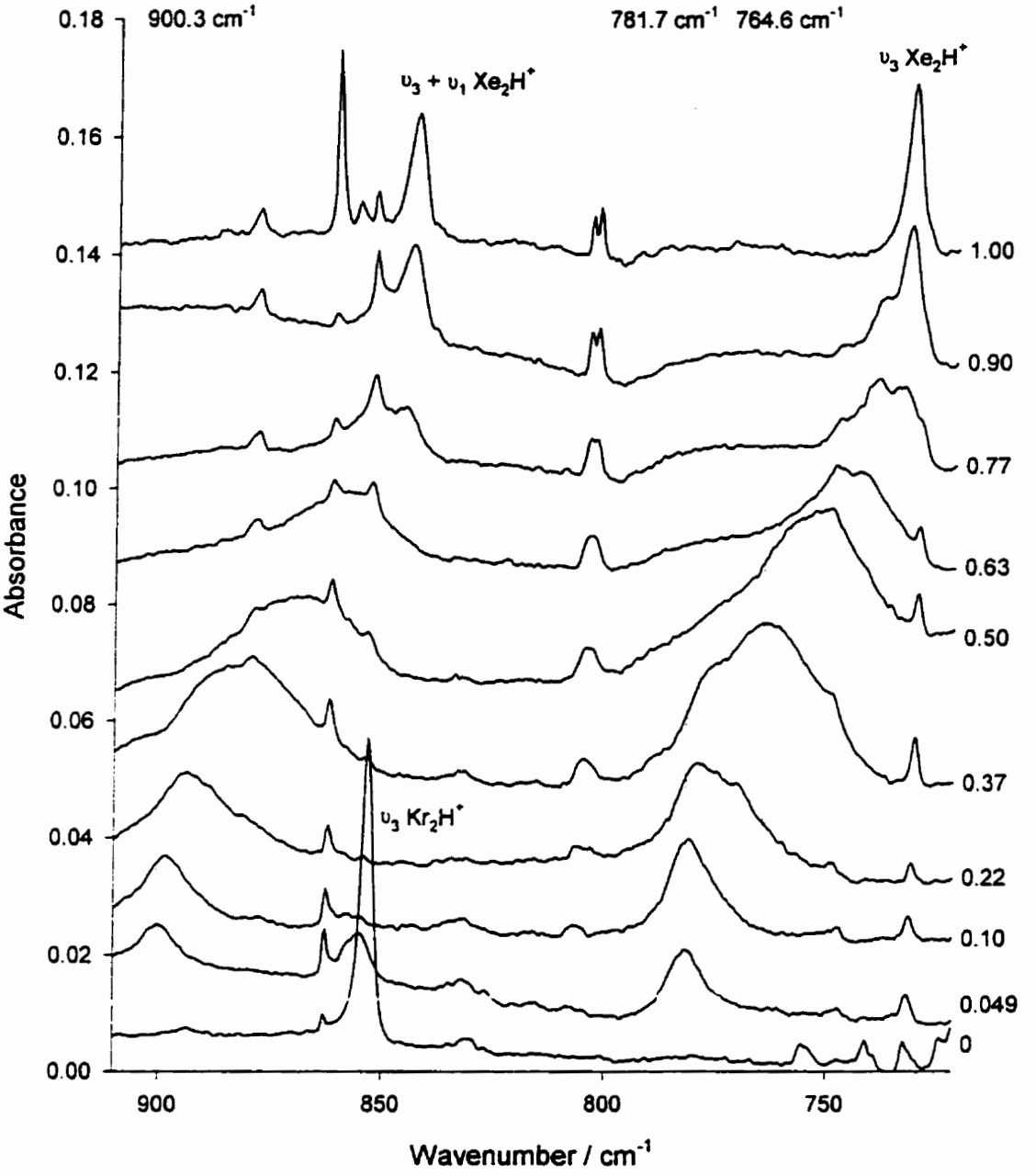

Figure 4.7. Portion of the FT-infrared spectra in the region 710 to 910 cm^{-1} recorded after 3 h of EBMI of methanol vapour diluted in xenon/krypton mixtures. The bands at 781.7 and 900.3 cm^{-1} are assigned to $(KrHXe)^+$ and at 764.6 cm^{-1} to Xe_2H^+ isolated in predominantly argon environments and are noted with wavenumber markers. The values to the right of each trace are the ratios Kr/Ar of the diluent gas.

$$Rg^{\bullet\cdot} + CH_3OH \rightarrow Rg + CH_3OH^{\bullet\cdot *}, \qquad \textbf{(4.1)}$$

where the * denotes an internally excited species.

The distonic isomer of the methanol radical cation ($CH_2OH_2^{\bullet+}$) has been shown in the past to be slightly preferred thermodynamically over the methanol radical cation. Furthermore, it has been observed experimentally that neutral bases such as H_2O and HF are quite effective in catalyzing the isomerization of radical cations of the form $CH_3X^{\bullet+}$ to their distonic isomers $^{\bullet}CH_2XH^{+}$.[19] It has also been shown in theory that rare-gases can act as neutral bases for proton-transport catalysis in the $CH_3OH^{\bullet+}/^{\bullet}CH_2OH_2^{+}$ isomerization (see chapter 6)[20] and in other systems such as the HCO^{+} to COH^{+} proton transfer isomerization.[21,22] Furthermore, the conclusions presented in chapter 6 suggest that any neutral base can act as a catalyst for the suggested isomerization reaction, to varying degrees depending on their proton affinities. Given the obvious presence of neutral bases in these experiments (as the carrier/support gas, precursor, or neutral products such as CO) it is assumed that the methanol radical cation can readily isomerize to its distonic isomer (reaction 4.2). The observation of both isotopomers of the Rg_2H^{+} species and the various scrambled isotopomeric by-products listed above in the EBMI experiments with CD_3OH as the precursor may be experimental evidence of this isomerization process.

$$CH_3OH^{\bullet\cdot *} + Rg \rightarrow CH_2OH_2^{\bullet\cdot *} + Rg \qquad \textbf{(4.2)}$$

Either of the excited cationic species in reaction 4.2 are known to lose an H atom given enough internal energy. If an Rg^+ cation were trapped in the matrix it would very likely form Rg_2^+, $Rg'Rg^+$ or Rg'^+_2 depending upon the concentration of Rg' in the Rg matrix and the mobility of the hole.[23] It would be expected and has been proposed before[9] that the hydrogen atom and one of these charged centres would combine to form Rg_2H^+ or $(RgHRg')^+$. Hydrogen atoms only become diffusive in Ar, Kr and Xe matrices at temperatures of approximately 20, 35 and 45 K, respectively.[24] During EBMI experiments, temperatures only as high as about 18 K are expected to be attained. If H-atom migration is responsible for the formation of these species, it can only happen in the liquid-like phase during condensation. It would, however, be more likely positive charges or holes that are mobile and responsible for formation of these rare-gas cations.

The absence of the organic cations, which would be expected on loss of hydrogen atoms from the parent cation, has been discussed earlier in chapter 3 as owing to the inadequacy of argon, krypton and xenon matrices for isolation of cations with higher electron affinities.

Another plausible mechanism for formation of Rg_2H^+ and $(RgHRg')^+$ involving loss of H^+ from the cations in reaction 4.2 is also worth considering. As previously stated, the initially-formed $CH_3OH^{\bullet+}$ or its distonic isomer have associated with them a large amount of energy from the ionization process. This energy is not sufficient, however, for either of these species to lose a proton through direct dissociative ionization. However, if an Rg-H bond is concurrently formed as the O-H is cleaved there is more than enough energy to overcome the endothermicity. Furthermore,

the energy requirement for this mechanism is simply the endothermicity since there is no significant barrier to intermolecular proton transfer.[25] It will be shown that there is likely more than enough energy to overcome the energy requirement for this concerted mechanism (reaction 4.3).

$$CH_2OH_2^{\bullet\cdot\cdot} + Rg \rightarrow (CH_2OH\cdots H\cdots Rg)^{\bullet\cdot} \rightarrow CH_2OH^{\bullet} + RgH^{\cdot} \qquad \textbf{(4.3)}$$

For example, with Ar as the Rg in reactions 4.1 and 4.3, the exothermicity of the overall reaction is 186 kJ mol^{-1} (Table 4.2). The proton abstraction reaction between $CH_3OH^{\bullet+*}$ and Rg (reaction 4.4) without isomerization also cannot be ruled out as a possible route to RgH^+ and $CH_2OH^{\bullet}$,

$$CH_3OH^{\bullet\cdot\cdot} + Rg \rightarrow (Rg\cdots H\cdots CH_2OH)^{\bullet\cdot} \rightarrow CH_2OH^{\bullet} + RgH^{\cdot}. \qquad \textbf{(4.4)}$$

In the presence of rare-gas, reactions 4.3 and 4.4 may be expected to compete with the unimolecular dissociation of $CH_3OH^{\bullet+*}$ and $CH_2OH_2^{\bullet+*}$ to form a hydrogen atom and CH_2OH^+.

Addition of reactions 4.1, 4.2 and 4.3 yields an overall reaction for the formation of the diatomic RgH^+ from methanol,

$$CH_3OH + Rg^{\bullet\cdot} \rightarrow CH_2OH^{\bullet} + RgH^{\cdot}. \qquad \textbf{(4.5)}$$

This is the case for the experiments where there is only one type of rare-gas present. If there is a mixture of two rare gases, Rg and Rg', then it is possible that one is responsible for ionization and the other forms the diatomic rare-gas-onium ion,

$$CH_3OH + Rg^{\bullet+} + Rg' \rightarrow CH_2OH^{+} + Rg + Rg'H^{\bullet}. \qquad \textbf{(4.6)}$$

When Rg≠Rg' and Rg' is the heavier rare-gas atom, reaction 4.6 is more exothermic than reaction 4.5 due to the increasing proton affinity of the heavier rare-gas atom.

In Table 4.2 are summarized the heats of reaction[26] for reaction 4.6 for various combinations of Ar and Kr. All but two of the reactions specified by reaction 4.6 and Table 4.2 are thermodynamically possible. The first, where Ar* is the ionizing agent, is highly endothermic. In fact, even loss of hydrogen atom from $CH_3OH^{\bullet+}$ following Penning ionization of CH_3OH with Ar*, would be only 14.5 kJ mol^{-1} exothermic but, Penning ionization of CH_3OH with Kr* and Xe* would be highly endothermic; it is with these arguments that Penning ionization is ruled out as a possible route to the production of the rare-gas-onium ions.

The reaction where $Xe^{\bullet+}$ is the charge exchange agent in the formation of XeH^+ is also endothermic. The fact that Xe_2H^+ is observed in the infrared spectra after EBMI of methanol/Xe mixtures suggests that simple charge transfer ionization of methanol by $Rg^{\bullet+}$ is not the only mechanism to production of these Rg_2H^+ species. Direct electron impact of methanol as a possible mechanism cannot be totally ruled out, however, it is not as likely as electron impact of Xe due to the

Table 4.2. Enthalpy changes for the reaction $CH_3OH + Rg^{\bullet+} + Rg' \rightarrow CH_2OH^{\bullet} + Rg + Rg'H^{+}$ for various Rg and Rg'.

Rg[a]	Rg'	$\Delta_r H$ / kJ mol^{-1}
Ar	Ar	-186[b]
Ar*	Ar	187
Kr	Kr	-70
Xe	Xe	40
Ar	Kr	-240
Ar	Xe	-311
Kr	Xe	-141

a: all species in this column are ions as per eq. 6 and as such are responsible for charge-exchange ionization, except for Ar* which is an excited state of the argon atom (11.9 eV) and is a Penning ionization agent. b: ref. 26.

relative amounts of these species in the original gas mixture. A second charge transfer ionization is certainly not very likely since these ions are not expected to have enough kinetic energy to overcome the coulombic repulsion of like charges. Other possibilities are that when Xe is ionized, it is also electronically excited to a metastable state of the ion or that Xe is doubly ionized. This electronically excited state of the xenon cation $Xe^{\bullet+*}$ or the doubly charged cation Xe^{++} would then be responsible for charge transfer ionization and energizing the methanol radical cation such that there is the possibility of proton abstraction by Xe to form XeH^+.

Once $Rg'H^+$ is formed, the subsequent formation of the triatomic cation through reaction with another rare-gas atom is exothermic. This would be most likely to occur during the condensation of the matrix, resulting in the formation of matrix-isolated $(RgHRg')^+$,

$$Rg'H^+ + Rg \rightarrow (RgHRg')^+. \qquad \textbf{(4.7)}$$

The mechanism presented above explains why at very low levels of Rg' (0.4 %) the mixed (RgHRg') is observed. At much higher concentrations of the heavier rare-gas there is still a possibility that $Rg'H^+$ will react with Rg but since there is so much Rg' it becomes more probable that $Rg'H^+$ will find and react with Rg' or that $(RgHRg')^+$ will react to exchange Rg' for Rg. These results are, in fact, consistent with the conclusions initially drawn by Lundell[14] after calculation of the dissociation energies for the $(RgHRg')^+$ species; that it is unlikely $(RgHRg')^+$ can be formed in mixtures containing high mole fractions of Rg' since reaction of Rg'H+ and Rg' to form Rg'_2H^+ is more exothermic.

4.4 Conclusions

Through electron bombardment of gaseous mixtures of methanol diluted in mixtures of rare gases, the mixed triatomic cations $(ArHKr)^+$, $(ArHXe)^+$, and $(KrHXe)^+$ have been isolated and spectroscopically characterized. Similarly, the antisymmetric stretching fundamental and first combination band with the symmetric stretch of Xe_2H^+ in primarily argon and krypton environments, as well as the antisymmetric stretch of Kr_2H^+ in a primarily argon environment have been observed and assigned.

Two mechanisms have been proposed for the formation of these species. The first involves dissociation of an internally-excited newly-born methanol radical cation into a hydrogen atom and CH_2OH^+. Electron holes (positive charge in the matrix), formed when argon cations are isolated in the matrix, have some mobility. When the hole reaches the matrix isolated hydrogen atom the charge is deeply bound in a "triatomic" having the structure of the proton bound dimers.

The second plausible mechanism assumes abstraction of proton from $CH_3OH^{+\bullet *}$ by a rare-gas atom in the gas phase. $Rg'H^+$ then combines with rare-gas in the matrix to form the observed proton-bound mixed rare-gas dimer.

4.5 References to Chapter 4

1. Aquilanti, V.; Galli, A.; Giardini-Guidoni, A.; Volpi, G.G. *J. Chem. Phys.* **1965**, *43*, 1967.
2. Fehsenfeld, F.C.; Schmeltekopf, A.L.; Ferguson, E.E. *J. Chem. Phys.* **1967**, *46*, 2802.
3. Adams, N.G.; Bohme, D.K.; Ferguson, E.E. *J. Chem. Phys.* **1970**, *52*, 5101.
4. Hvistendahl, G.; Saastad, O.W.; Uggerud, E. *Int. J. Mass Spectrom. Ion Processes* **1990**, *98*, 167.
5. Bondeybey, V.E.; Pimentel, G.C. *J. Chem. Phys.* **1972**, *56*, 3832.
6. Milligan D.E.; Jacox, M.E. *J. Mol. Spectrosc.* **1973**, *46*, 460.
7. Wight, C.A.; Ault, B.S.; Andrews, L. *J. Chem. Phys.* **1976**, *65*, 1244.
8. Kunttu, H. ;Seetula, J.; Räsänen, M.; Apkarian, V.A. *J. Chem. Phys.* **1992**, *96*, 5630.
9. Kunttu, H.M.; Seetula, J.A. *Chem. Phys.* **1994**, *189*, 273.
10. Potapov, S.G.; Sukhanov, L.P.; Gutsev, G.L. *Russ. J. Phys.* **1989**, *63*, 479.
11. Rosenkrantz, M.E. *Chem. Phys. Lett.* **1990**, *173*, 378.
12. Lundell, J.; Kunttu, H. *J. Phys. Chem.* **1992**, *96*, 9774.
13. Nieman, J.; Kauppi, E.; Lundell, J.; Kunttu, H. *J. Chem. Phys.* **1993**, *98*, 8698.
14. Lundell, J. *J. Mol. Struct.* **1995**, *355*, 291.
15. Published as Fridgen T.D.; Parnis, J.M. *J. Chem. Phys.* **1998**, *109*, 2162.
16. Ault, B.S. *Acc. Chem. Res.* **1982**, *15*, 103 and references therein.
17. Räsänen, M.; Seetula, J.; Kunttu, H. *J. Chem. Phys.* **1993**, *98*, 3914.
18. Fridgen, T. D.; Zhang, X. K.; Parnis, J. M.; R. E. March, manuscript in preparation.
19. Gauld J.W.; Radom, L. *J. Am. Chem. Soc.* **1997**, *119*, 9831.

20. Fridgen T.D.; Parnis, J.M. Submitted to *Int. J. Mass Spectrom. Ion Processes*, July 1998.

21. Chalk, A.J.; Radom, L. *J. Am. Chem. Soc.* **1997**, *119*, 7573.

22. Cunje, A.; Rodriquez, C. F.; Bohme, D. K.; Hopkinson, A. C. *J. Phys. Chem.* **1998**, *102*, 478.

23. Fajardo, M.E.; Apkarian, V.A. *J. Chem. Phys.* **1986**, *85*, 5660.

24. Willard, J.E. *Cryogenics* **1982**, 359.

25. Szulejko, J.E.; McMahon, T.B. *J. Am. Chem. Soc.* 1993, 115, 7839.

26. All heats of reactions were calculated from the heats of formation of the species in eq. 5. All heats of formation were taken from Lias, S. G.; Bartess, J. E.; Liebman, J. F.; Holmes, J. L.; Levin, R. D.; Mallard, W. *J. Phys. Chem. Ref. Data*, **1988**, *17*, Supp. 1.

Chapter 5

Density Functional Theory Study of the Proton-Bound Rare-Gas Dimers Rg_2H^+ and $(RgHRg')^+$ (Rg=Ar, Kr, Xe): Interpretation of Experimental Matrix Isolation Infrared Data[A]

5.1 Introduction

Proton-bound rare-gas dimers are fundamental species in rare-gas matrices and have become known in the rare-gas matrix isolation environment since the first report of their observation in 1972 by Bondybey and Pimentel.[1] Since the observation and assignment of the combination band progression $\nu_3 + n\nu_1$ of the Rg_2H^+ species (Rg=Ar,Kr, or Xe) with a compelling argument for a linear

---

[A] This chapter is a modified version of the manuscript published as T.D. Fridgen and J. Mark Parnis, *J. Chem. Phys*, **1998**, *109*, 2155.

centrosymmetric structure by Kunttu *et al.*[2] much theoretical work has been conducted on these species. Among these are *ab initio*[3,4,5,6,7,8,9] calculations of thermodynamic properties, structures and vibrational wavenumbers as well as studies attempting to explain the thermal instability of these species.[6] These studies also confirm the assignment of the observed infrared absorptions to the linear triatomic cation. Lundell has also reported results of calculations on the mixed rare-gas species $(RgHRg')^+$ (where Rg≠Rg') using both the MP2 level of theory and the Density Functional Theory (DFT).[9] Lundell's work represents the first attempt at using the DFT approach for the prediction of molecular properties, vibrational wavenumbers and dissociation energies for these ions. These BLYP/DZVP calculated geometries compare well with calculations at the MP2 level employing an effective core potential approach[6,9] for the Rg_2H^+ species, and yield calculated energies which are substantially lower than all previously-calculated results.

All previously-calculated wavenumbers are grossly inaccurate when compared with experimental results observed in low-temperature matrices. For example, the DFT calculations reported by Lundell[9] predict the antisymmetric stretching fundamentals for Ar_2H^+, Kr_2H^+ and Xe_2H^+ to occur at 987.7 cm^{-1}, 1044.7 cm^{-1} and 900.7 cm^{-1}, respectively, compared with the observed values[2,10] of 903.8, 853.2cm^{-1} and 731.4 cm^{-1}. The poor quantitative and qualitative agreement of these calculations with respect to the trend in the observed v_3 bands is reproduced by the MP2/ECP2 calculations.[9] Despite the concluding remarks from the summary of this

paper,

> "The calculated vibrational frequencies are in good agreement with experiments where experimental values are available. For the new species (the mixed rare-gas cations) the predictions will be of great help when trying to locate them either in low-temperature matrices or in the gas phase..."

the BLYP/DZVP and MP2/ECP2 calculated vibrational wavenumbers for the mixed rare-gas species are likely to be misleading with respect to the position of these bands.

The geometries of Ar_2H^+, Kr_2H^+, Xe_2H^+, $(ArHKr)^+$, $(ArHXe)^+$ and $(KrHXe)^+$ have been optimized using the Becke and Perdew functionals (BP86) combined with an augmented Gaussian (DZVP) basis set and a numerical basis set of comparable size (DN**). In section 5.3.1, the results of the calculations with respect to the ion structure and molecular properties are presented and discussed. The vibrational wavenumbers for both H and D isotopomers are discussed in section 5.3.2 and are shown to be in good *qualitative* agreement with wavenumbers observed in rare gas matrices.[2,10,11] Generally, all calculated harmonic antisymmetric stretching wavenumbers reported to date[5,6,7,8,9] for these cations are unacceptably high when compared to the v_3 bands observed in rare-gas matrices. In order to test the hypothesis expressed by Rosencranz[5] that matrix isolation of these Rg_2H^+ ions acts to greatly reduce v_3 from the gas-phase value, attempts were made to simulate argon matrix-isolated Ar_2H^+ by placing additional argon atoms

around the cation. These calculations were extended to include Kr_2H^+ and Xe_2H^+ isolated in krypton and xenon, respectively, and yielded very interesting results in that they bring the calculated wavenumbers into extremely good *quantitative* agreement with experiment as presented and discussed in section 5.3.3.

Inverse isotope dependencies on kinetic and thermodynamic parameters have been reported for several **HLH** (heavy-light-heavy) species in the past. Clary and Connor[12] calculated bond energies for YXY molecules (Y=I or Br and X=Muon, H, or D) and predict that their bond dissociation energies show an inverse isotope dependence due to a greater decrease in the zero-point energy of XH on deuterium or muon substitution compared with XHX. The calculated bond dissociation enthalpies D_0 and D_{298} for the Rg_2H^+ and $(RgHRg')^+$ are reported in section 5.3.4 and predict that the bond dissociation energies for cleavage of an Rg-H bond are greater than for the Rg-D bond for these species.

The presence of an inverse isotope behavior in the symmetric stretching mode of these species has also been reported in a recent communication on the photo-generation of Xe_2H^+.[2] In section 5.3.5, a more rigorous analysis of the vibrational data is presented and it is concluded that there is no evidence for an inverse isotope dependence in the harmonic symmetric stretch for $XeHXe^+$ and $XeDXe^+$ or the related rare-gas cations. This conclusion is supported by the calculated values for the symmetric stretching mode wavenumbers for both isotopomers of these species to be reported in this work.

5.2 Computational Details

All calculations were performed using the non-local spin density approximation employing Becke's gradient-corrected exchange functional[13] with Perdew's gradient-corrected correlation functional.[14] The corrections to the local spin density gradient were recalculated at each step in the SCF iteration (NLSDA/BP86, hereafter the NLSDA prefix is dropped and the method is referred to as BP86). The calculations were performed utilizing two distinct basis sets. The first was an augmented Gaussian double-ζ split valence basis set with polarization functions added to all atoms including H (referred to as DZVP), similar to that used by Lundell.[9] The other basis set was a numerical double-ζ split-valence basis set with polarization functions added to all atoms including H (referred to as DN**). The DN** basis set has been shown to give results comparable to those obtained using the 6-311G** Gaussian basis set used in conjunction with the same DFT functionals.[15] The calculations with the DZVP basis set were performed using the deMon[16] set of programs at the University of Montreal. The calculations using the DN** basis set were performed using the SPARTAN 5.0[17] set of programs at Trent University. The vibrational wavenumbers were calculated by numerical differentiation (central differences) of analytical gradients.

5.3 Results and Discussion

5.3.1 Molecular Constants

The optimized geometries, energies, and partial charges on each atom, calculated using the BP86 functionals and either the Gaussian DZVP or numerical DN** basis sets, are presented in Table 5.1 for Ar_2H^+, Kr_2H^+, Xe_2H^+, $(ArHKr)^+$, $(ArHXe)^+$ and $(KrHXe)^+$. These DN** results predict smaller bond distances for the Ar_2H^+ and Kr_2H^+ than the BLYP/DZVP[9] results, in line with the results at the MP2 level of theory.[9] For $(ArHKr)^+$ the BLYP/DZVP calculations reported by Lundell[9] predict a longer Ar-H bond length than the Kr-H. The opposite is predicted by the DN** and DZVP calculated bond lengths, a longer Kr-H bond, in agreement with Lundell's MP2 calculations[9] and with what would be expected based on the respective atomic radii of Ar and Kr. For the mixed species containing Xe, both the DN** and DZVP calculations predict a slightly longer Ar-H bond or Kr-H bond than the Xe-H bond distance as did the previously reported DFT results.[9] The difference in the bond lengths reported in this work is greatly reduced using the DN** basis set compared to the DZVP basis set. For example, the Ar-H and Xe-H bonds are calculated to be 1.849 and 1.756 Å, respectively, using the DZVP basis set whereas they are 1.777 and 1.739 Å, respectively, using the DN** basis set. It is anticipated that use of an even more extensive basis set will yield predictions in accordance with what might be expected

Table 5.1. Calculated molecular constants for the various homogeneous and mixed proton-bound rare-gas dimers.

Species	Method/Basis	R_{Rg-H} / Å	q_{Rg}	q_H	E / au
Ar_2H^+	BP86/DZVP	1.583	0.387	0.226	-1055.2155
	BP86/DN**	1.536	0.341	0.317	-1055.3852
Kr_2H^+	BP86/DZVP	1.693	0.410	0.180	-5507.2998
	BP86/DN**	1.698	0.315	0.370	-5508.4307
Xe_2H^+	BP86/DZVP	1.912	0.452	0.096	-14469.5558
	BP86/DN**	1.914	0.378	0.244	-14471.0946
$(ArHKr)^+$	BP86/DZVP	ArH=1.618 KrH=1.622	Ar=0.325 Kr=0.469	0.206	-3281.2644
	BP86/DN**	ArH=1.586 KrH=1.644	Ar=0.304 Kr=0.350	0.346	-3281.9082
$(ArHXe)^+$	BP86/DZVP	ArH=1.849 XeH=1.756	Ar=0.199 Kr=0.635	0.166	-7762.3963
	BP86/DN**	ArH=1.777 XeH=1.739	Ar=0.209 Xe=0.510	0.280	-7763.2431
$(KrHXe)^+$	BP86/DZVP	KrH=1.834 XeH=1.798	Kr=0.313 Xe=0.553	0.134	-9988.4293
	BP86/DN**	KrH=1.831 XeH=1.814	Kr=0.238 Xe=0.460	0.303	-9989.7641

based on the respective atomic radii *i.e.*, longer Xe-H bond lengths and shorter Ar-H or Kr-H bond lengths.

5.3.2 Vibrational Spectra

The calculated wavenumbers for the infrared absorptions of both the H and D isotopomers of the homogeneous and mixed rare-gas triatomic cations are presented in Table 5.2. The calculated bending mode (v_2) is not degenerate using DFT even though all structures are linear. The splitting in these modes is decreased significantly when using the DN** basis set. Splitting of the degenerate modes has been seen in previous DFT calculations[9] and is probably due to the central differences algorithm not using the full $D_{\infty h}$ symmetry of the species.

The wavenumbers calculated using the DN** basis set are compared with observed infrared spectral data[2,10,11] and are in excellent qualitative agreement for the first four cations and their isotopomers listed in Table 5.2 in that the calculated results predict the correct ordering of the energies of the vibrations. This is in contrast to those infrared absorptions predicted by Lundell's DFT calculations[9] and calculations employing MP2 theory,[6,9] both of which result in incorrect ordering of the wavenumbers for the antisymmetric stretching modes. A set of scaling factors may be obtained by dividing the observed wavenumbers by the corresponding calculated values yielding 0.7414, 0.7211 and 0.7120 for Ar_2H^+, Kr_2H^+ and Xe_2H^+ isolated in Ar, Kr and Xe matrices, respectively. The magnitude of these scaling factors further demonstrates the unsatisfactory quantitative agreement between the

Table 5.2. Calculated vibrational wavenumbers for the homogeneous and mixed proton-bound rare-gas dimers and their deuterated isotopomers.

	ν_1 / cm^{-1}	ν_2 / cm^{-1}	ν_2' / cm^{-1}	ν_3 / cm^{-1}
Ar_2H^+				
BP86/DZVP	303.7	644.6	647.4	1248.1
BP86/DN**	301.6	673.2	673.8	1218.9
Observed[a,b]	237			903.8
Ar_2D^+				
BP86/DN**	301.6	479.2	479.6	867.6
Observed[a]				643.7
Kr_2H^+				
BP86/DZVP	101.2	589.7	593.0	1235.5
BP86/DN**	188.9	580.7	580.7	1183.2
Observed[a,b]	155			853.2
Kr_2D^+				
BP86/DN**	188.9	412.0	412.0	838.9
Observed[a,b]	165			606.5
Xe_2H^+				
BP86/DZVP	138.4	498.6	503.9	1067.4
BP86/DN**	136.3	514.7	515.6	1027.2
Observed[a,b]	112			731.4
Xe_2D^+				
BP86/DN**	136.3	364.8	365.4	728.0
Observed[a,b]	117			516.9
$ArHKr^+$				
BP86/DZVP	229.6	575.2	598.8	1286.1
BP86/DN**	237.6	617.5	617.7	1203.4
Observed[a,b]				885.3
$ArDKr^+$				
BP86/DN**	237.6	438.8	439.0	854.8
Observed[a]				628.7

Table 5.2. (cont.d)

	v_1 / cm^{-1}	v_2 / cm^{-1}	v_2' / cm^{-1}	v_3 / cm^{-1}
$ArHXe^+$				
BP86/DZVP	133.5	325.5	441.9	1492.1
BP86/DN**	156.3	486.1	487.6	1378.2
Observed[a,b]	124.4			828.1
$ArDXe^+$				
BP86/DN**	156.1	345.27	346.3	979.2
Observed[a]				
$KrHXe^+$				
BP86/DZVP	146.3	472.6	503.1	1264.4
BP86/DN**	143.4	504.6	504.7	1227.9
Observed[a,b]	118.6			782.0
$KrDXe^+$				
BP86/DN**	143.2	357.8	357.9	871.0
Observed[a]				553.0

a: v_3 from Fridgen and Parnis, ref. 11.

b: v_1 estimated by subtracting the v_3 fundamental value from the $v_3 + v_1$ combination band, from references 11 and 10.

observed infrared spectrum in matrices and the calculated results. The decrease in scaling factors on going from Ar to Xe is likely to be attributable to increased perturbation of the ions associated with the increased polarizability of the medium in which the observed spectra were recorded. In fact, when ν_3 values for Kr_2H^+ and Xe_2H^+ in Kr and Xe matrices, respectively, are compared with ν_3 values for Kr_2H^+ and Xe_2H^+ observed in a matrix composed of a large portion of Ar, reported in the previous chapter,[11] the scaling factors increase to 0.7429 and 0.7749 presumably reflecting the diminished polarizability of argon with respect to krypton and xenon and the consequential decrease in ion perturbation which is in support of this hypothesis. A similar scaling factor is obtained for the antisymmetric stretch of $(ArHKr)^+$ isolated in argon (0.7357) and the calculated wavenumber also agrees qualitatively with the calculated value using the DN** basis set. The calculated ν_3 employing the smaller DZVP basis set gives good qualitative agreement with the observed values for the homogeneous rare-gas species but incorrect ordering for all the mixed rare-gas species. For the mixed species containing Xe, the calculated values are in poor qualitative agreement with the observed values, even with the larger DN** basis set. We suggest that poor results for the Xe-containing mixed rare-gas species are due to the inflexiblility of the DN** basis set in the same way that the DZVP basis set is not flexible enough to use as a predictive tool for any of these mixed rare-gas-containing species.

5.3.3 Towards Matrix Isolated Ar_2H^+

In this section, the results of attempts to quantitatively model the experimentally-observed matrix-isolated Rg_2H^+ wavenumbers is discussed. To begin, it was assumed that the H centre occupies an O_h interstitial site as was first deduced by Bondybey and Pimentel[1] in the earliest paper on these species. Since there is very little doubt that the absorber is the triatomic centrosymmetric cation, it is further assumed that two opposite rare-gas atoms (axial) are much closer to the hydrogen atom than the other four nearest rare-gas atoms (radial) leaving the H centre in a 'flattened O_h interstitial site'. The structure of these cations is D_{4h} as depicted in Figure 5.1 where r_r and r_a represent the radial and axial Rg-H bond distances, respectively.

In attempts to reproduce the antisymmetric stretching mode wavenumber of matrix-isolated Ar_2H^+ four argon atoms were placed in a plane containing H and perpendicular to the intermolecular axis and 2.66 Å from the H atom of the Ar_2H^+ optimized geometry from the preceding section. This initial r_r distance would be the distance from the H centre to the radial argon atom in an unperturbed solid argon matrix O_h interstitial site.[18] This geometry was frozen and the calculated v_3 was found to be reduced to 1126 cm^{-1}, approximatly 90 cm^{-1} lower than free Ar_2H^+. When the geometry of the central cation was optimized by freezing only the radial argon atoms, r_a increased from 1.526 Å to 1.592 Å resulting in a very large reduction of v_3 to 508 cm^{-1}. When the entire geometry was optimized (no frozen atoms), r_a was found to be 1.526 Å, unchanged from the calculations of the previous

section but the radial argon atoms exploded to 3.697 Å from the H centre resulting in only a 15 cm^{-1} decrease in v_3.

It was decided that an intermediate route be taken in order to demonstrate that agreement with the observed value can be obtained with a reasonable model. The radial Ar-H bond length r_r was held frozen and systematically decreased from 3.697 Å, while the Ar_2H^+ centre was free to optimize. The v_3 calculated wavenumber dropped into the region of the experimentally-observed absorption when r_r was held at 2.820 Å. At this distance, r_a optimized to 1.556 Å, and the symmetric and antisymmetric stretching wavenumbers dropped 10 % and 26 % to 271.6 cm^{-1} and 904.1 cm^{-1}, respectively, from those reported in the previous section. The results of the calculations are summarized in Table 5.3. These geometry restrictions bring both v_1 and v_3 into excellent agreement with the experimentally observed antisymmetric stretching wavenumber (903 cm^{-1}) and the symmetric stretching wavenumber derived from the $v_1 + v_3$ combination band (approximately 240 cm^{-1}). It is interesting to note that both r_a and the vibrational wavenumbers are relatively insensitive to changes in r_r in the range 2.85 Å to 2.82 Å. In this range, the calculated vibrational wavenumbers coincide closely with those observed in the matrix. Further decrease causes drastic changes in the vibrational wavenumbers listed in Table 5.3. It can also be seen from Table 5.3 that the radial argon atoms take on a considerable amount of the total charge, about 6.4 %. This donation of electron density could be the cause of the increase in the Ar-H bond length in Ar_2H^+, resulting in a decrease of the bond strength and a considerable decrease in

Table 5.3. Calculated molecular constants and vibrational wavenumbers for Ar_2H^+ optimized with four Ar atoms held in a plane containing hydrogen and at r_r Å from the hydrogen atom.

r_r / Å[a]	r_a / Å[a]	q_r	q_a	q_H	ω_1 / cm^{-1}	ω_3 / cm^{-1}
--	1.526	--	0.341	0.317	301.6	1218.9
3.697	1.526	0.004	0.338	0.309	300.4	1203.6
2.82	1.556	0.016	0.325	0.287	271.6	904.7
2.82[b]	1.555	0.011	0.320	0.285	272.7	905.6
2.66	1.592	0.021	0.318	0.281	244.4	508.4

a: The subscripts r and a refer to radial and axial Ar atoms, see Figure 5.1. b: Includes the next 8 Ar atoms held at 4.599 Å from the H centre. The partial charge associated with each of these 8 outer Ar atoms was calculated to be 0.004.

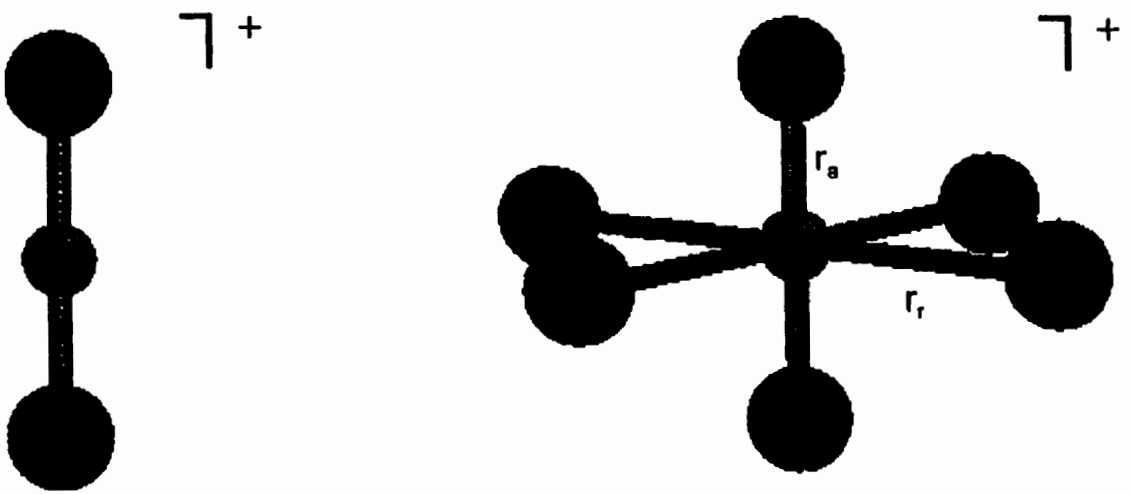

Figure 5.1. Ball-and-stick model diagrams of Ar_2H^+ and the D_{4h} structure of Ar_2H^+ surrounded by four Ar atoms.

the vibrational wavenumber from the unperturbed gas-phase ion. Although we have simply varied r_r until we obtained a good fit to the antisymmetric stretching wavenumbers, the geometries at which this fit was obtained are not at all unreasonable. We have, however, clearly shown that the presence of the radial Ar atoms has an effect on the structure and vibrational wavenumbers of the Ar_2H^+ cation and can bring them into agreement with the observed matrix values.

Similar calculations were performed on Kr_2H^+ and Xe_2H^+ surrounded by four krypton and xenon atoms, respectively. It was found that at an r_r of 3.035 Å and 3.282 Å, the r_a distance increased to 1.735 Å and 1.950 Å, respectively, for Kr_2H^+ and Xe_2H^+. The antisymmetric stretching wavenumbers for these two species dropped into agreement with the observed values, calculated at these geometries to be 854.0 cm^{-1} and 730.2 cm^{-1}, respectively, for Kr_2H^+ and Xe_2H^+. Similarly the wavenumbers for the symmetric stretch dropped to 168.5 cm^{-1} and 126.2 cm^{-1} for Kr_2H^+ and Xe_2H^+ respectively from the values reported in Table 5.2 into better agreement with the experimental values derived from ν_1 and $\nu_3 + \nu_1$ which are 155 cm^{-1} and 112 cm^{-1}, respectively.

There was very little change in the calculated bending wavenumbers and, since they are to date unobserved, are not reported in Table 5.3.

It is interesting to note that the actual r_r values for unperturbed Ar, Kr and Xe crystals are 2.655 Å, 2.820 Å and 3.065 Å, respectively. The difference between these values and the r_r found to give wavenumbers which fit the observed values are 0.165 Å, 0.215 Å and 0.217 Å, increasing over the series Ar, Kr, Xe. This is not

surprising considering the increasing size of the respective atoms. The triatomic cations would be expected to increase in the radial dimension with increasing atomic number and require a larger matrix site.

One serious criticism of these calculations may be the neglect of the next closest layer of matrix atoms. To establish the importance of these neighboring atoms, a calculation was performed where 8 argon atoms were held fixed at a distance which corresponds to an unperturbed matrix site (4.599 Å from H)[18] around the Ar_6H^+ core discussed above, where r_r=2.82 Å. The symmetry of this system was D_{4h} (Fig. 5.2) and, during the calculation, only the Ar_2H^+ centre was allowed to optimize. The Ar-H bond length in the optimized geometry of Ar_2H^+ decreased less than 0.001 Å to 1.555 Å, while the symmetric and antisymmetric wavenumbers only increased to 272.7 cm^{-1} and 905.6 cm^{-1}, respectively. The amount of the total charge not residing on the triatomic increased from 6.4 % to 7.6 %. These results show that the outer 8 argon atoms have only a small effect on the geometry and the calculated wavenumbers of the triatomic cation so that only the four frozen radial argon atoms are required for a reasonable model of these matrix-isolated cations.

It is interesting and quite worth noting that with respect to the infrared spectrum the matrix-isolated ion more closely resembles Rg_6H^+ rather than Rg_2H^+. Except for the charge, this was in fact the structure predicted by Bondybey and Pimentel in the first report concerning these species.[1] It is basically a hydrogen atom trapped in a flattened octahedral site and there is positive charge associated with the species.

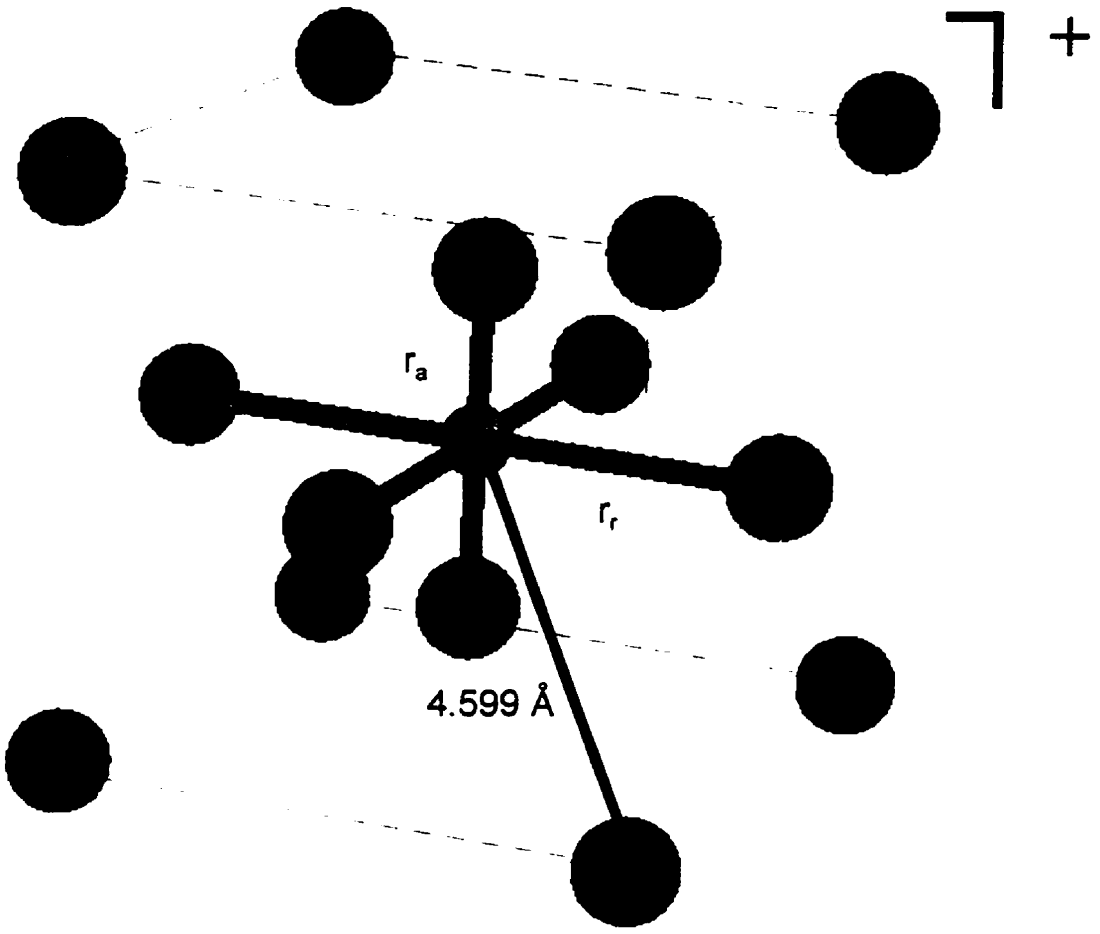

Figure 5.2. Ball-and-stick model diagram of Ar_2H^+ surrounded by the four nearest neighbour Ar atoms and the eight next-to-nearest neighbour Ar atoms.

5.3.4 Isotope Effect on Dissociation of $(RgHRg')^+$

There are no experimental thermodynamic data for any of the mixed or homogeneous (RgHRg') species. The validity of the calculated thermodynamic properties to follow in this section are therefore verified by comparing calculated proton affinities of the rare-gas atoms (which we performed using the same DFT method and DN** basis set as described above) with known experimental values.[19] Our calculated proton affinities at 298 K for Ar, Kr and Xe are 375.4 kJ mol^{-1}, 417.1 kJ mol^{-1} and 483.5 kJ mol^{-1}, respectively. The accepted 298 K experimental values are[19] 371 kJ mol^{-1}, 425 kJ mol^{-1}, and 496 kJ mol^{-1} with which our calculated values compare quite favorably.

In Table 5.4 are listed the values of the bond dissociation enthalpies associated with the loss of a rare-gas atom from the various triatomic cations and their isotopomers at 0 K and at 298 K. These all-electron DFT calculations predict that the bond dissociation energies increase upon D substitution which is opposite to what is normally expected. As noted above, this effect was also seen with IXI and BrXBr where X=Mu, H, D.[12] In these cases, though, the YXY molecule is predicted to exist on a minimum-free potential energy surface, however, the zero-point energy of the triatomic is less than the zero-point energy of the diatomic. This results in the triatomic molecule having a few vibrational levels which are lower in energy than the zero-point energy of the dissociation products (YXY is termed a *vibrationally-bound* molecule).[12] Our calculations (and prior calculations) show that all of these Rg_2H^+ and $(RgHRg')^+$ species exist as minima on the potential energy

Table 5.4. Enthalpies of reaction calculated using the BP86/DN method and basis sets for the reactions $(RgHRg')^+ \rightarrow RgH^+ + Rg'$.**

Reaction	D_0 / kJ mol^{-1}	D_{298} / kJ mol^{-1}
$Ar_2H^+ \rightarrow ArH^+ + Ar$	69.0	65.9
$Ar_2D^+ \rightarrow ArD^+ + Ar$	68.9	65.0
$Kr_2H^+ \rightarrow KrH^+ + Kr$	77.0	73.6
$Kr_2D^+ \rightarrow KrD^+ + Kr$	77.0	72.8
$Xe_2H^+ \rightarrow XeH^+ + Xe$	77.9	75.0
$Xe_2D^+ \rightarrow XeD^+ + Xe$	75.0	70.9
$(ArHKr)^+ \rightarrow ArH^+ + Kr$	94.8	93.0
$(ArDKr)^+ \rightarrow ArD^+ + Kr$	94.5	91.1
$(ArHKr)^+ \rightarrow KrH^+ + Ar$	52.7	48.7
$(ArDKr)^+ \rightarrow KrD^+ + Ar$	52.9	48.2
$(ArHXe)^+ \rightarrow ArH^+ + Xe$	137.5	135.4
$(ArDXe)^+ \rightarrow ArD^+ + Xe$	137.1	133.8
$(ArHXe)^+ \rightarrow XeH^+ + Ar$	29.3	24.5
$(ArDXe)^+ \rightarrow XeD^+ + Ar$	29.6	24.3
$(KrHXe)^+ \rightarrow KrH^+ + Xe$	115.7	112.7
$(KrDXe)^+ \rightarrow KrD^+ + Xe$	115.5	111.5
$(KrHXe)^+ \rightarrow XeH^+ + Kr$	49.6	45.5
$(KrDXe)^+ \rightarrow XeD^+ + Kr$	49.6	44.9

surface and, therefore, are bound in the classical sense rather than displaying exclusive vibrational bonding. The inverse dependence of the reaction enthalpies on D substitution results from the low energy of the symmetric stretching vibration of the triatomics. On substitution with deuterium, the zero-point energy of the diatomic decreases more than the triatomic (see Fig. 5.3), resulting in a lower enthalpy of dissociation for the Rg_2D^+ cations. As would be expected, the inverse isotope dependence of the dissociation enthalpy is amplified at higher temperature.

The higher energy dissociation of the mixed rare-gas triatomic cations also shows the inverse isotope effect for D_0 and D_{298}. The dissociation of the lighter rare gas atom from these species, however, displays a normal isotope dependence at 0 K but, a small inverse isotope dependence in their dissociation is predicted at 298 K.

The calculated dissociation energies for the lower energy dissociation of the mixed rare-gas species are in fair agreement with the BLYP/DZVP values calculated by Lundell.[9] Our calculated dissociation energies are, however, in disagreement for both the homogeneous Rg_2H^+ cations and the higher energy dissociation of the mixed species. Lundell's values are approximately 40 kJ mol^{-1} higher for all of the Rg_2H^+ species and over 100 kJ mol^{-1} greater for the higher energy dissociation of the mixed species. It is not possible at this point to say which dissociation enthalpies are more accurate without experimental figures with which to compare them.

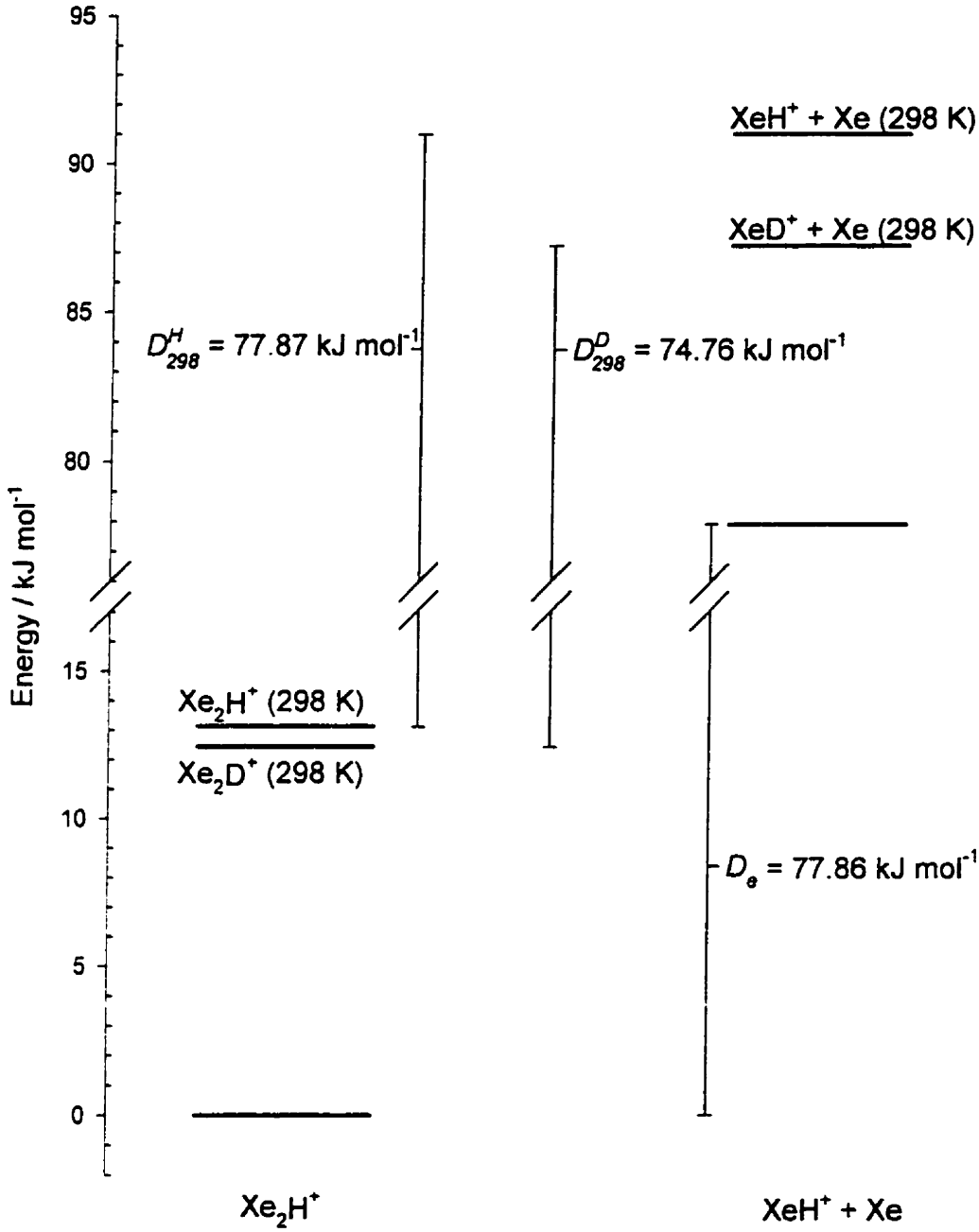

Figure 5.3. Schematic energy level diagram showing the relative energies of the reactants and products for the dissociation of Xe_2H^+ into XeH^+ and Xe without zero-point energy and including zero-point energy corrected to 298 K for both H and D isotopomers. Also shown is the dissociation energy, D_e and the dissociation energies D_{298} for the hydrogen and deuterium isotopomers.

5.3.5 A Reevaluation of the Isotope Effect in v_1

Employing an anharmonic oscillator model for a diatomic Kunttu et al.[2] have calculated the quadratic anharmonicity constants $\omega_e x_e$ to be 0.845 and 1.43 for Xe_2H^+ and Xe_2D^+, respectively. Using these values they calculate the harmonic wavenumbers ω_e for the symmetric stretch to be 113.7 cm^{-1} and 120.8 cm^{-1} for Xe_2H^+ and Xe_2D^+, respectively, showing an *inverse isotope dependence* for both $\omega_e x_e$ and ω_e. For similar heavy-light-heavy (**HLH**) molecules such as BrHBr and IHI, it has been shown theoretically that the symmetric stretch shows very little isotope dependence on the central atom. The calculations do, on the contrary, show a very small *normal isotope dependence* for these molecules.[12]

There has never been any mechanism proposed whereby an inverse isotope dependence on the harmonic wavenumbers of vibrational transitions could be expected. The calculated wavenumbers for the symmetric stretch are the same for both H and D isotopomers for each of Rg_2H^+ species. Since the model Kunttu *et al.*[2] used for the vibrational analysis is approximate and only valid for diatomic molecules, further investigation into the reported inverse isotope dependence in the symmetric stretch of these species was deemed necessary.

The general vibrational energy formula for the case where there are degenerate vibrations is[20]

$$G(v_1,v_2,v_3,\ldots) = \sum_i \omega_i\left(v_i+\frac{d_i}{2}\right) + \sum_i\sum_{k\geq i} x_{ik}\left(v_i+\frac{d_i}{2}\right)\left(v_k+\frac{d_k}{2}\right) + \sum_i\sum_{k\geq i} g_{ik}\ell_i\ell_k + \ldots \quad \textbf{(5.1)}$$

where the term on the left is the vibrational term value or vibrational energy. The ω_i are the harmonic vibrational wavenumbers in cm^{-1}, x_{ik} are the quadratic anharmonic constants ($i=k$) or the mode-to-mode coupling constants ($i \neq k$), d =1 except for the degenerate bend where d = 2, and v_i and v_k are the vibrational quantum numbers. The third summation corrects for vibration-induced angular momentum, with quantum numbers ℓ and angular momentum constants g_{ik} which are both 0 except for the degenerate mode. It should be noted that the cubic and higher-order terms (ie. x_{ikj}) have been omitted from equation 1 for simplicity.

Expanding equation (1) for G(0,0,1), G(1,0,1) and G(2,0,1), including the cubic terms, setting these values equal to 730.9 cm^{-1}, 842.8 cm^{-1}, and 953.1 cm^{-1}, respectively, (for Xe_2H^+ from reference 2) yields the following differences,

$$G(1,0,1)-G(0,0,1)=\omega_1+2x_{11}+x_{12}+\frac{3}{2}x_{13}+\frac{13}{4}x_{111}+2x_{112}+3x_{113}+x_{122}+\frac{9}{4}x_{133}+\frac{3}{2}x_{123}=111.9\,cm^{-1} \quad \textbf{(5.2)}$$

$$G(2,0,1)\ G(0,0,1)=2\omega_1+6x_{11}+2x_{12}+3x_{13}+\frac{31}{2}x_{111}+6x_{112}+9x_{113}+2x_{122}+\frac{9}{2}x_{133}+3x_{123}=222.2\,cm^{-1} \quad \textbf{(5.3)}$$

Subtracting two times equation 5.2 from equation 5.3 yields,

$$x_{11}^{H}+\frac{9}{2}x_{111}^{H}+x_{112}^{H}+\frac{3}{2}x_{113}^{H}=-0.80\,cm^{-1}, \quad \textbf{(5.4)}$$

where the superscript denotes the H isotopomer of Xe_2H^+. A similar analysis on the data for the combination band progression for Xe_2D^+ yields,

$$x_{11}^{D} + \frac{9}{2}x_{111}^{D} + x_{112}^{D} + \frac{3}{2}x_{113}^{D} = -1.45\,cm^{-1}. \qquad \textbf{(5.5)}$$

These sums obviously show inverse dependence upon the isotope but it is most likely that the mode-to-mode coupling constants which are responsible for this dependence. Furthermore, substitution of equation 5.4 into equation 5.2, (and similarly substitution equation 5.5 into an equation similar to 5.2 except in terms of the deuterium isotopomer), one gets the following equations after solving for ω_1,

$$\omega_1^{H}\,(cm^{-1}) = 113.5 - x_{12}^{H} - \frac{3}{2}x_{13}^{H} + \frac{23}{4}x_{111}^{H} - x_{122}^{H} - \frac{9}{4}x_{113}^{H} - 3\,x_{123}^{H} \qquad \textbf{(5.6)}$$

$$\omega_1^{D}\,(cm^{-1}) = 113.5 - x_{12}^{D} - \frac{3}{2}x_{13}^{D} + \frac{23}{4}x_{111}^{D} - x_{122}^{D} - \frac{9}{4}x_{113}^{D} - 3\,x_{123}^{D} \qquad \textbf{(5.7)}$$

where, again, the superscripts denote the H and D isotopomers. The simple diatomic analysis assumes that all of the anharmonic constants and mode-to-mode coupling constants in equations 5.6 and 5.7 are zero and is known to be a severe oversimplification when considering these systems, even near the bottom of the potential well.[8] It is clear that ω_1 cannot be shown to be inversely dependent upon the isotope of the central atom without further data to allow determination of the mode-to-mode coupling constants.

5.4 Conclusions

The DFT calculations of the vibrational wavenumbers for the centrosymmetric Rg_2H^+ cations presented here show correct qualitative agreement with all three of the matrix-observed v_3 bands. Similarly, the calculated antisymmetric stretch for $(ArHKr)^+$ is in good qualitative agreement with the band assigned to it following electron bombardment matrix-isolation studies. The v_3 bands assigned to the mixed species containing xenon, from the same study, are not in good qualitative agreement with the DFT-calculated wavenumbers presented here; this difference is assumed to be due to a lack in flexibility of the basis set employed. It has been shown that good quantitative agreement with the matrix-observed vibrational wavenumbers of Rg_2H^+ cations can be achieved by simulating a matrix environment in which the H centre is assumed to be trapped in a flattened octahedral interstitial matrix site. The problem of modeling matrix-isolated Rg_2H^+ cations that has plagued researchers in the past may not be the theory. The problem may be simply that the matrix-observed species is not a triatomic cation but the 7-atomic cation Rg_6H^+.

The calculations also predict an inverse isotope dependence in the dissociation of all homogeneous and mixed species. It has been shown that use of a complete vibrational energy expression in an analysis of the vibrational spectra of these species yields no conclusive evidence for the inverse isotope dependence in v_1 reported in previous studies.

5.5 References to Chapter 5

1. Bondybey, V.E.; Pimentel, G.C. *J. Chem. Phys.* **1972**, *56*, 3832.
2. Kunttu, H.; Seetula, J.; Räsänen, M. Apkarian, V.A. *J. Chem. Phys.*,**1992**, *96*, 5630.
3. Potapov, S.G.; Sukhanov, L.P.; Gutsev, G.L. *Russ. J. Phys. Chem.* **1989**, *63*, 479.
4. Hvistendahl, G.; Saastad, O.W.; Uggerud,E. *Int. J. Mass Spectrom. Ion Processes* **1990**, *98*, 167.
5. Rosenkrantz, M.E. *Chem. Phys. Lett.* **1990**, *173*, 378.
6. Lundell, J.; Kunttu, H. *J. Phys. Chem.* **1992**, *96*, 9774.
7. Nieminen, J.; Kauppi, E.; Lundell, J.; Kunttu, H. *J. Chem. Phys.* **1993**, *98*, 8698.
8. Nieminen, J.; Kauppi, E. *Chem. Phys. Lett.* **1994**, *217*, 31.
9. Lundell, J. *J. Mol. Struct.* **1995**, *355*, 291.
10. Kunttu, H.M.; Seetula, J.A. *Chem. Phys.* **1994**, *189*, 273.
11. Fridgen, T.D.; Parnis, J.M. *J. Chem. Phys.* **1998**, *109*, 1655.
12. Clary, D.C.; Connor, J.N.L. *J. Phys. Chem.* **1984**, *88*, 2758.
13. Becke, A.D. *Phys. Rev.* **1988**, *A38*, 3098.
14. Perdew, J.P. *Phys. Rev.* **1986**, *B33*, 8822.
15. Hehre, W. J.; Lou, L., Eds. *A Guide to Density Functional Calculations in SPARTAN*, **1997**, Wavefunction, Inc., Irvine.

16. a) St-Amant, A.; Salahub, D.R., *Chem. Phys Lett.* **1990**, *169*, 387. b) St-Amant, A., Ph.D. Thesis, University of Montreal, Montreal, Quebec, 1992. c) deMon-KS version 3.4, Casida, M.E.; Daul, C.; Goursot, A.; Koester, A.; Pettersson, L.; Proynov, E.; St-Amant, A.; Salahub, D.R.; Duarte, H.; Godbout, D.; Guan, J.; Jamorski, C.; Leboeuf, M.; Malkin, V.; Malkina, O.; Sim, F.; Vela F., deMon Software, 1996.

17. Spartan Version 5.0, Wavefunction, Inc., 18401 Von Karman Avenue, Suite 370, Irvine, CA 92612 USA.

18. Pollack, G.L. *Rev. Mod. Phys.* **1964**, *36*, 748.

19. Lias, S. G.; Bartess, J. E.; Liebman, J. F.; Holmes, J. L.; Levin, R. D.; Mallard, W. *J. Phys. Chem. Ref. Data*, **1988**, *17*, Supp. 1.

20. Herzberg, G. *Molecular Spectra and Molecular Structure II. Infrared and Raman Spectra,* **1996,** D. Van Nostrand Company, Inc., Toronto, p. 210.

Chapter 6

A Density Functional Theory Study of the Role of Ar, Kr, Xe, and N_2 as Catalysts in the $CH_3OH^{+\bullet}$ to $CH_2OH_2^{+\bullet}$ Isomerization Reaction[A]

6.1 Introduction

The inter- and intramolecular mobility of the proton is of fundamental importance to the gas-phase chemical reactions of cationic species containing hydrogen. Proton mobility between molecules is at the heart of proton affinity studies and has been studied extensively by various mass spectrometric techniques[1,2]. It has been demonstrated that when the proton transfer between two

---

[A] This chapter is a modified version of the manuscript to be published as T.D. Fridgen and J. Mark Parnis, Int. J. Mass Spectrom. Ion Processes, Feb. 1999.

species is exoergic, the reaction generally occurs readily[2,3] suggesting an insignificant energy barrier.

In contrast, energy barriers to intramolecular proton (or atom[4]) transfers are normally quite significant. This is best exemplified by the isomers of protonated carbon monoxide COH^+ and HCO^+ which have been individually isolated and characterized in the gas phase [5,6]. Isomerization in either direction is not observed to take place under normal experimental conditions and theory has shown there to be a very high energy barrier separating the two isomers:[7,8] 300 kJ mol^{-1} for the HCO^+ → HOC^+ isomerization and 150 kJ mol^{-1} for the reverse process. It has been demonstrated, however, that significant HOC^+ to HCO^+ isomerization occurs in the presence of H_2.[9,10] Theoretical calculations have shown that this is likely due to a catalytic reaction channel with a lower activation energy requirement involving a H_2-stabilized activated complex,[10,11]

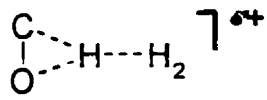

that is, H_2 acts to catalyze the isomerization. More recent theoretical studies demonstrate that many neutral species such as the rare-gases, CO, HF, and N_2, etc., may also act to lower the barrier to such isomerization reactions[12,13] which Bohme has described as proton-transport catalysis.[3]

Theorized in terms of proton-transport catalysis, two distinct mechanisms

exist for the interaction of the catalyst with the shifting proton. When the leaving site has a lower proton affinity than the catalyst, and the accepting site has a higher proton affinity than the catalyst, the proton may be transferred from the leaving site to the catalyst M forming a complex between the deprotonated precursor and MH^+. The proton is then transferred to the accepting site from MH^+, resulting in a 'forth and back' proton shift isomerization[14] (Mechanism I). The energy requirement for this process is minimal since the barrier to intermolecular proton transfer is insignificant. This mechanism has proven to be consistent with recent experimental observations. In the CO- or CO_2-catalyzed $HCN^+ \rightarrow HNC^+$ isomerization, Hansel *et al.*[15] note that at higher temperatures catalysis is not as efficient. The observed inverse temperature dependence was explained to be the consequence of a shorter lifetime of the intermediate collision complex after the initial proton transfer from HCN^+ to CO (or CO_2).

In the second mechanism (Mechanism II), the catalyst has a lower proton affinity than both the proton leaving and accepting sites of the de-protonated molecule such that there is never a proton transfer to the catalyst. Instead, the catalyst complexes with and stabilizes the transition-state structure, thereby lowering the activation-energy barrier of the uncatalyzed reaction. Like the uncatalyzed reaction, this is a concerted bond-breaking/bond-making mechanism. The neutral bases or catalysts in this study (Ar, Kr, Xe and N_2), have lower proton affinities than both the leaving and accepting sites for the $CH_3OH^{+\bullet} \rightarrow CH_2OH_2^{+\bullet}$ isomerization such that their reactions would be examples of this form of catalysis.

For completeness, a third interaction is described which Gauld and Radom have described as the 'spectator mechanism' (Mechanism III).[16] In this mechanism the catalyst is not directly involved in the migration of the proton, but is complexed at another position on the reacting cation. The extent of catalysis, consequently, is not as great as it is for the first two mechanisms, but may still lower the barrier with respect to the separated catalyst and reactant cation ($M + R^+$) compared to the isolated system. However, since stabilization of the reactant-catalyst complex ($M\cdots R^+$) is considerably greater, the barrier for isomerization of this complexed species is generally higher than that of the uncomplexed species in the isolated system.

As with HCO^+ and COH^+, the methanol radical cation ($CH_3OH^{+\bullet}$, **1**) and its distonic isomer ($CH_2OH_2^{+\bullet}$, **3**) have been individually observed. They do not interconvert and, therefore, must be separated by a large barrier.[17,18] Calculations have predicted this barrier to be slightly greater than 100 kJ mol^{-1}.[19] Experimentally, it has been shown that interaction of **1** with H_2O[20,21] or neutral methanol[21] facilitates the **1** to **3** isomerization. High-level ab initio calculations[22] predict that when a 'spectator' water molecule is bound to the hydroxyl hydrogen, the barrier for interconversion with respect to complexed **1** and complexed **3** increases but lies slightly below the energy of separated H_2O and **1**. In contrast when the water molecule interacts with the shifting proton, a barrier of only 15.9 kJ mol^{-1} above the **1**-H_2O complex is predicted.

Quite recently, a detailed theoretical survey of the effects of HF, H_2O and

NH_3 on the isomerization of the three radical cations $CH_3F^{+\bullet}$, $CH_3OH^{+\bullet}$, and $CH_3NH_2^{+\bullet}$ to their respective distonic isomers $CH_2FH^{+\bullet}$, $CH_2OH_2^{+\bullet}$, and $CH_2NH_3^{+\bullet}$ has been reported by Gauld and Radom employing a modification of G2 theory.[16] In that paper, it is elegantly demonstrated that H_2O is ideally suited to catalyze the **1** to **3** isomerization by Mechanism I, since its proton affinity lies between that of C and O in $CH_2OH^{\bullet}$. This is in contrast to hydrofluoric acid which has a lower proton affinity than both ends of $CH_2OH^{\bullet}$ but still greatly reduces the energy barrier to isomerization (Mechanism II). NH_3 has a greater proton affinity than both ends and would likely react to give NH_4^+ and $CH_2OH^{\bullet}$ rather than catalyze the **1** to **3**, isomerization.

In this paper, the work of Gauld and Radom is extended to include the study of the effects of the non-polar reagents Ar, Kr, Xe and N_2 on the **1** to **3** isomerization. These gas-phase interactions can be of utmost importance in matrix isolation experiments where hydrogen-containing cations are in the presence of a great abundance of the aforementioned agents in the gas phase prior to condensation on the low-temperature substrate. Subsequently-recorded spectra may reveal decomposition products of catalyzed isomerization rather than simple unimolecular decomposition products of energetic ionic species. Similarly, mass spectrometrists employ some of these neutral bases as CID agents and/or cooling agents in sector instruments and flow tubes as well as ion trap and ICR trap mass spectrometry. The possibility, therefore, exists that catalytic isomerization may occur in these contexts.

6.2 Computational Details

The accurate prediction of thermochemical quantities by G2, MP2, CBSQ (complete basis set-quadratic configuration interaction) and numerous DFT approaches have recently been compared by Curtiss *et al.*[23] and in numerous papers by Jursic.[24,25,26,27,28] Of these methods, CBSQ ranks highest for accuracy followed closely by G2-related methods.[24,25] Hybrid DFT methods, although inferior to CBSQ and G2, also give very good results and, of these, the B3LYP method in conjunction with large Gaussian basis sets is particularly recommended. Although many of these procedures can be very accurate, they can be extremely time consuming. The main density functional method and numerical basis sets utilized in this study were chosen both for reasons of availability of reasonably large basis sets for Kr and Xe and for computational expediency.

All calculations were performed using the non-local spin density approximation (NLSDA) employing either Becke's gradient-corrected exchange functional (B)[29] or Becke's three parameter functional (B3)[30] combined with either of the gradient-corrected correlation functionals of Perdew (P86)[31], Lee, Yang and Parr (LYP)[32] or Perdew and Wang (PW91)[33]. The corrections to the local spin density gradient were recalculated at each step in the SCF iteration. The calculations were performed utilizing either a numerical double-ζ split-valence basis set with polarization functions added to all atoms including H (referred to as DN**) or the Gaussian double- or triple-ζ basis sets (6-31G*, 6-311G** or 6-311+G**) augmented with polarization functions on the heavy atoms (denoted with *) or on

both the heavy atoms and H (**). Where the + symbol occurs in the basis set, diffuse functions were added to heavy atoms. The DN** basis set has been shown to give results comparable to those obtained using the 6-311G** Gaussian basis set used in conjunction with the same DFT functionals.[34] All calculations using the DN** basis set were performed using the SPARTAN 5.0[35] set of programs and all calculations employing the Gaussian basis sets were performed using the GAUSSIAN 94W computational package.[36] The vibrational wavenumbers were calculated by numerical differentiation of analytical gradients (central differences).

The main method of calculation reported here is the BP86 method. Although the BP86 method is not on the 'recommended list' it will become apparent that this method gives acceptable results for the information desired in this work.

6.3 Results

6.3.1 The Uncatalyzed Proton Transfer

In this section are reported the results of the calculations performed on **1**, **3**, and the transition state joining them (**2**) employing three combinations of exchange and correlation functionals, namely BP86, B3PW91 and B3LYP with either the DN**, 6-31G*, 6-311G** or 6-311+G** basis sets. These combinations of functionals in conjunction with the 6-31G* basis set were chosen in an attempt to extrapolate zero-point vibrational energy (ZPVE) and the vibrational component of the thermal contribution to enthalpy ($\Delta H_{vib}(298)$) scaling factors for the BP86/DN** and other method/basis set combinations from those calculated by Scott and

Radom;[37] these scaling factors could be used to correct the energies for systematic errors inherent in the computational methods. DFT calculated vibrational frequencies are generally quite good[37] resulting in scaling factors very close to 1.[38] It was, therefore, unnecessary to correct the energies which follow since the corrected energies were the same, to a tenth of a kJ mol^{-1}, as those calculated without using scaling factors.

The BP86/DN** calculated structures of the methanol radical cation (**1**), its distonic isomer (**3**) and the transition state joining the two on the potential energy (**2**) surface are shown in Figure 6.1. The geometries of these three cations compare quite well with those geometries found using the Gaussian basis sets. Similarly, the DFT-calculated geometries of all three species compare well with those obtained using HF, MP2, and QCISD(T) methods.[19,39,40,41]

The most noteworthy difference with respect to geometry lies with that of species **1**. Using HF, MP2 and QCISD, the symmetry of the calculated minima of the methanol radical cation are basis-set dependent. In most cases, the C_1 geometry is preferred with the HCOH dihedral angle about 16° from eclipsed[41] and the C_s structures being first-order saddle points on the potential energy surface. The results of all the DFT calculations reported here predict a C_s eclipsed geometry for **1** in agreement with QCISD(T)/6-311G* results[41] and MP2 results using the 6-311G**, 6-311+G**, 6-311G(2df,p) and 6-311+G(2df,p) basis sets.[39] The calculated C-H(2) and C-H(3) bonds in **1** are 1.135 Å using BP86/DN**, considerably longer than normal C-H bond lengths. This is likely the result of the strong interaction

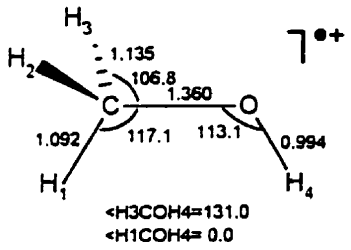

1

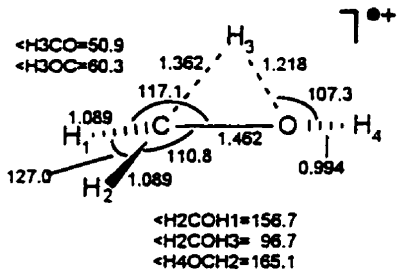

2

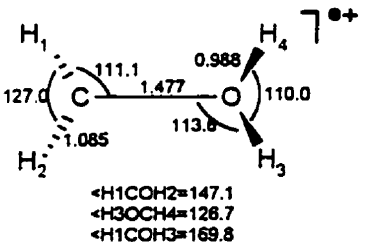

3

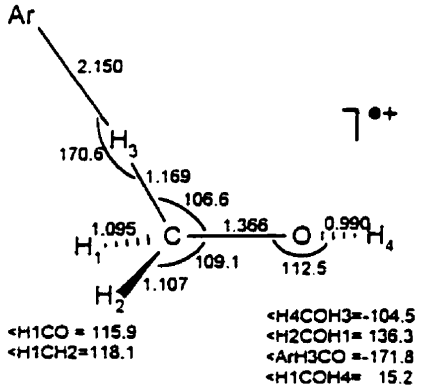

1-Ar

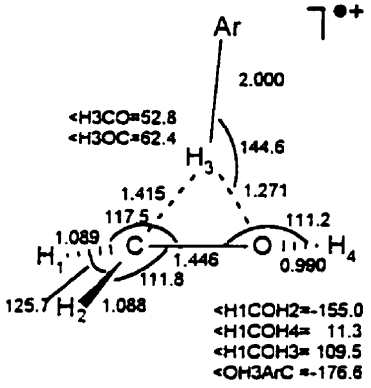

2-Ar

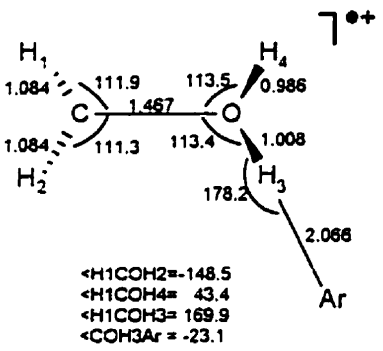

3-Ar

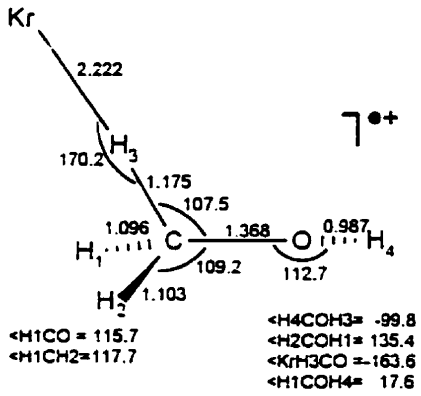

1-Kr

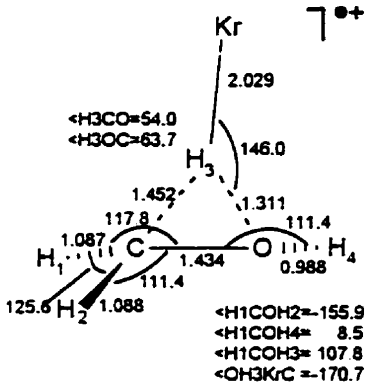

2-Kr

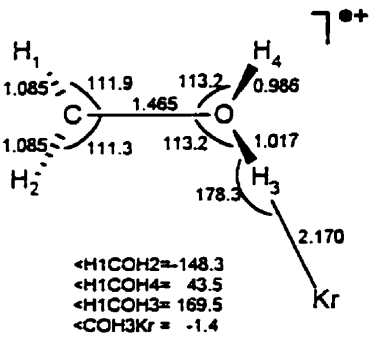

3-Kr

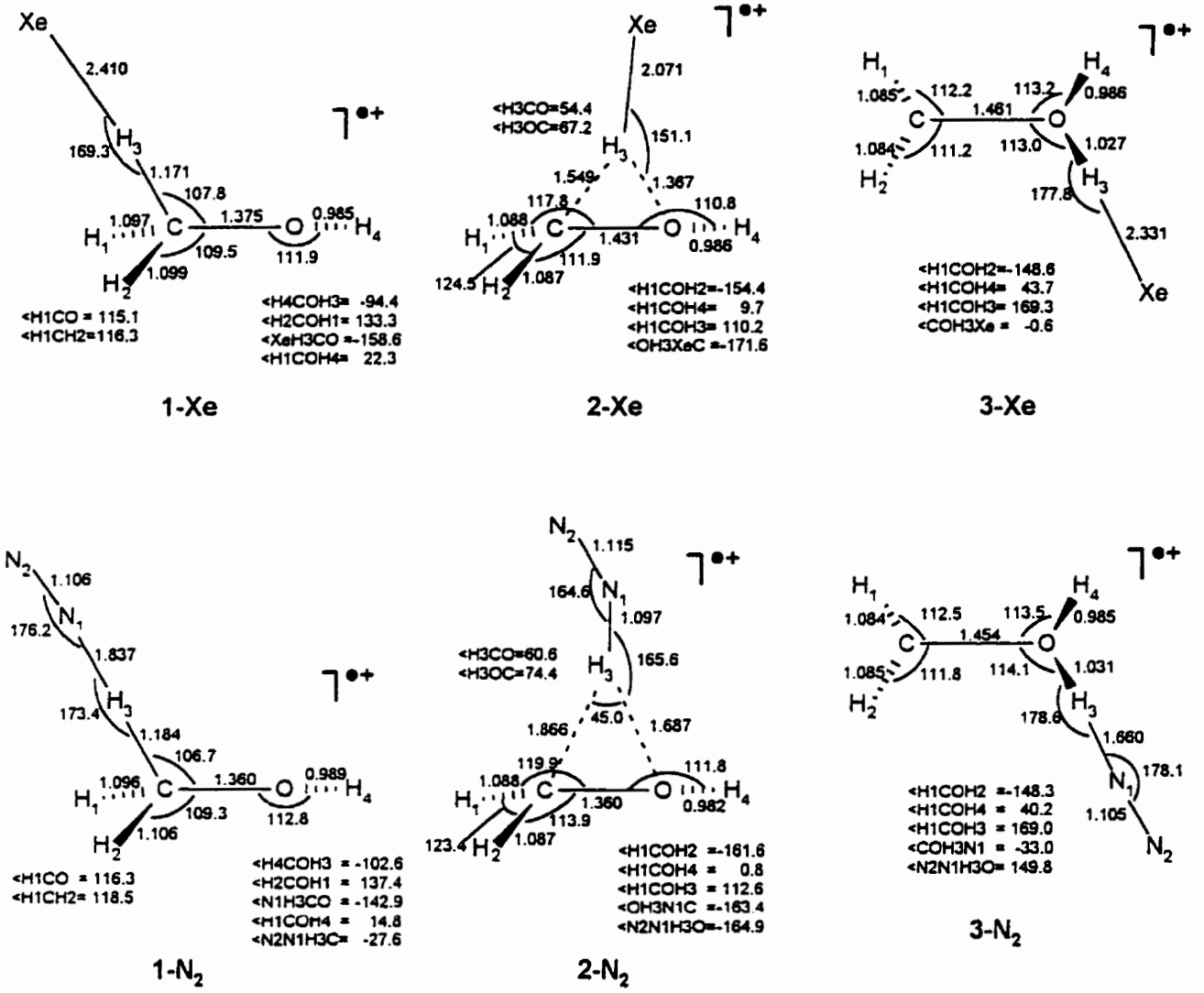

Figure 6.1. BP86/DN** calculated geometries of the methanol radical cation (**1**), its distonic isomer (**3**), the transition state joining the two (**2**), and the Ar-, Kr-, Xe- and N_2-associated species.

between the oxygen $2p_x$ and $2p_z$ atomic orbitals and the C-H(2) and C-H(3) bonds which form the fourth-highest occupied molecular orbital and which Tureček[42] and Ma *et al.*[19] have interpreted as hyperconjugative interaction in explaining the one longer C-H bond in their calculated C_1 structure of $CH_3OH^{+\bullet}$. These hyperconjugative interactions were also present in the C_s structures from references 39 and 41.

In Table 6.1, the enthalpies are listed for various stationary points on the $CH_4O^{+\bullet}$ potential energy surface. These calculated enthalpies are listed relative to the distonic isomer **3** for reasons discussed below. As has been asserted in the past,[34] it is quite obvious that the DN** basis set yields similar results as the triple-ζ Gaussian basis using the same combination of exchange and correlation functionals. In fact, the BP86/DN** results are as good as the BP86/6-311+G** results from this point of view.

The most dissatisfying results of these calculations are associated with the energies of the methanol radical cation **1**. On examination of Table 6.1, it is clear that all of the DFT-calculated relative energies of **1** are in significant error when compared with both the G2 and experimental values. The best calculation is in error by 24 kJ mol^{-1}. In many cases **1** is calculated to be more stable than **3**, including all calculations employing BP86 theory; this is in direct contrast with experiment and all other methods of calculation. Comparing the proton affinities of the O end and C end of CH_2OH in the last column of Table 6.1 (C end proton affinities in the shaded column), it is recognized that the DFT methods employed

Table 6.1. Calculated and experimental 298 K relative[a] enthalpies (kJ mol^{-1}) for various stationary points on the $CH_4O^{+\bullet}$ potential energy surface.

method/basis set	$CH_3OH^{+\bullet}$(1)	$H_2C(H)OH^{+\bullet}$ (2)	$CH_2OH_2^{+\bullet}$ (3)	$CH_2OH^{\bullet}$(4) + H^{+a}	
BP86/DN**	-10.2	115.7	0	685.0	
BP86/6-31G*	-22.4	109.6	0	699.4	
BP86/6-311G**	-10.6	111.3	0	700.8	
BP86/6-311+G**	-10.2	111.5	0	686.7	
B3LYP/6-31G*	-8.8	129.0	0	702.8	
B3LYP/6-311G**	5.0	131.7	0	706.2	
B3LYP/6-311+G**	5.6	131.9	0	691.7	
B3PW91/6-31G*	-6.2	128.1	0	704.9	
B3PW91/6-311G**	5.8	128.4	0	709.7	
B3PW91/6-311+G**	6.3	130.1	0	697.6	
G2(b)	31.8	135.7	0		
exptl(c)	30.3		0	689.1	

a: energies in the darker columns are relative to $CH_3OH^{+\bullet}$, ie. they correspond to the proton affinity of $CH_2OH^{\bullet}$ at C.

b: from reference 19.

c: calculated using data from reference [43].

here greatly overestimate the stability of the methanol radical cation. The calculated proton affinities of **3** are, however, in fairly good agreement with experiment and many of the barrier heights for the **1** to **3** isomerization are in good agreement with the G2-calculated values.

The results of the DFT calculations reported above have obvious problems with respect to the over-stabilization of the methanol radical cation, however, the primary values of interest here are the *differences* in barrier heights when Ar, Kr, Xe or N_2 are complexed with the transition state. That the differences in barrier heights calculated here using BP86/DN** density functional theory are acceptable values will be addressed below.

6.3.2 Ar-, Kr-, Xe- and N_2- Catalyzed Proton Transfer

In Table 6.2, the BP86/DN** and B3LYP/6-311+G** calculated relative energies of the stationary points in the Ar-catalyzed **1** to **3** isomerization are compared. As is the case for the uncatalyzed reaction and these two DFT method/basis set combinations (Table 6.1), the calculated energies do not agree. The calculated barrier heights are not in agreement, however, the decreases in barrier heights from the uncatalyzed reaction are predicted to be 18 and 12 kJ mol^{-1} for the BP86/DN** and B3LYP/6-311+G** calculations, respectively, differing by only 6 kJ mol^{-1}. Since we are primarily concerned with the difference between barrier heights we are confident in using the BP86/DN** DFT method to probe the effect of Ar, Kr, Xe and N_2 on the barrier height of the **1**→**3** proton-transfer

Table 6.2. Comparison of calculated stationary point energies along the Ar-catalyzed 1 to 3 isomerization reaction pathway.

Stationary Point	BP86/DN**	B3LYP/6-311+G**
Ar + 1	-10.2	5.6
Ar-1	-26.1	1.4
Ar-2	97.5 (-18)	119.9 (-12)
Ar-3	-14.6	-15.0
Ar + 3	0.0	0.0

Values in parentheses denote the difference between the respective calculated uncatalyzed barrier heights and the Ar-catalyzed barrier heights.

isomerization.

The BP86/DN** structures of the Ar-, Kr-, Xe- and N_2-associated species of **1**, **2** and **3** are shown in Fig. 6.1. The C-H(3) bond lengths of both **1-X** and **3-X** are seen to get progressively longer over the series X=Ar, Kr, Xe or N_2. This increase seems reasonable as some degree of X-H bonding with a concomitant decrease in the order of C-H or O-H bonding is to be expected. This has also been observed in the reports on catalyzed HCO^+ isomerization.[13,16] Note that the C-H(3) bond distance of **1-X**, however, shows a significant increase (0.034 Å) on going from **1** to **1-Ar** while the remaining two C-H bond lengths are quite normal, reflecting a strong interaction with the catalyst.

The calculated vibrational wavenumbers for species **1**, **2**, **3** and the Ar-, Kr-, Xe-, and N_2-associated structures are reported in Table 6.3. It can be seen that for all of the calculated minima (species **1** and **3** as well as associated structures) all vibrational wavenumbers are real. For the transition structures there is only one imaginary wavenumber which corresponds to the isomerization reaction coordinate. The magnitude of the imaginary wavenumber in each of the uncatalyzed transition states and the Ar-, Kr- and Xe-associated structures shows that the motion along the reaction coordinate is due primarily to the H(3) hydrogen. By substituting H(3) for deuterium in the Ar-catalyzed transition state the imaginary wavenumber drops from 1655i cm^{-1} to 1238i cm^{-1}. From these values, a ν^H/ν^D ratio of 1.337 is calculated. For pure hydrogenic motion this ratio would have a value which of 1.414. By substituting ^{12}C to ^{13}C in the same structure, the imaginary wavenumber

Table 6.3. Calculated vibrational wavenumbers (cm^{-1}) and zero-point vibrational energies (kJ mol^{-1}) for the various $CH_4O^{+\bullet}$ and Rg-$CH_4O^{+\bullet}$ species.

$CH_3OH^{+\bullet}$ (1) ZPVE=121.6	$H_2C(H)OH^{+\bullet}$ (2) ZPVE=115.4	$H_2COH_2^{+\bullet}$ (3) ZPVE=127.9
277 953 980 1048 1160 1207 1278 1452 2616 2724 3154 3481	1712i 684 887 963 988 1182 1263 1405 2098 3098 3279 3469	306 689 731 884 917 1259 1393 1649 3129 3315 3496 3597
(1-Ar) ZPVE=123.7	**(2-Ar) ZPVE=116.4**	**(3-Ar) ZPVE=129.0**
76 111 172 308 941 980 1081 1147 1211 1325 1447 2330 2932 3110 3520	1655i 139 173 246 688 881 950 998 1173 1274 1408 1650 3100 3274 3512	85 150 164 389 647 787 915 948 1272 1400 1642 3134 3141 3324 3564
(1-Kr) ZPVE=124.9	**(2-Kr) ZPVE=115.3**	**(3-Kr) ZPVE=128.6**
94 167 192 363 951 997 1084 1154 1216 1337 1440 2268 2970 3101 3551	1606i 152 190 268 678 864 943 1007 1139 1274 1374 1466 3106 3282 3537	86 161 174 408 662 816 923 952 1272 1397 1634 2991 3136 3319 3565
(1-Xe) ZPVE=126.3	**(2-Xe) ZPVE=112.9**	**(3-Xe) ZPVE=127.4**
90 161 216 407 976 1015 1082 1188 1232 1344 1452 2280 2995 3101 3578	1513i 183 202 300 631 798 842 1009 1096 1146 1292 1434 3106 3275 3562	79 158 174 413 650 827 932 954 1270 1397 1617 2811 3136 3320 2567
(1-N_2) ZPVE=141.4	**(2-N_2) ZPVE=137.6**	**(3-N_2) ZPVE=147.2**
71 131 144 210 265 482 981 1013 1100 1145 1217 1323 1461 2160 2365 2943 3102 3529	882i 163 273 249 352 370 671 739 944 1037 1115 1327 1449 2082 2304 3101 3259 3615	126 197 224 225 267 491 653 893 957 1016 1299 1410 1676 2385 2757 3136 3314 3572

drops to 1650i cm^{-1} showing that there is indeed some C motion. By using the animation feature in SPARTAN it is also observed that there is some carbon and hydrogen motion. The relatively lower imaginary wavenumber calculated for the N_2-associated transition state is due to some motion of both nitrogen atoms in this coordinate. The results of these calculations, with respect to the energies, are shown graphically in Figure 6.2. With respect to the **3-X** complexes, the barrier to isomerization does not decrease inordinately. However, with respect to (**X + 3**), the barrier decreases quite dramatically (that is, the net decrease in the barrier, with respect to separated reagents, is significantly reduced). Decreases of 18, 34, 55 and 65 kJ mol^{-1} are calculated for the Ar-, Kr-, Xe- and N_2-catalyzed reactions, respectively. These catalyzed isomerization reactions become increasingly important, competing against the lower-energy decomposition pathway of **1** and **3** to form hydroxy methylene cation and hydrogen atom. It is important to note that the lowest energy pathways for decomposition of the $CH_4OX^{+\bullet}$ complex will be to form either of the $CH_4O^{+\bullet}$ isomers and X. Given enough energy and momentum along the appropriate reaction coordinate, however, it is still quite possible, to catalyze the **1**-**3** isomerization. This was considered as a possible source of mixed isotopomeric decomposition products in the electron-bombardment matrix-isolation experiments conducted on methanol which was reported in Chapter 4[44] and is discussed further below.

It can be seen by comparing the structures in Fig. 6.1 that the H(3)-X bond distances in the transition state (**2-X** species X=Ar, Kr, Xe or N_2) are considerably

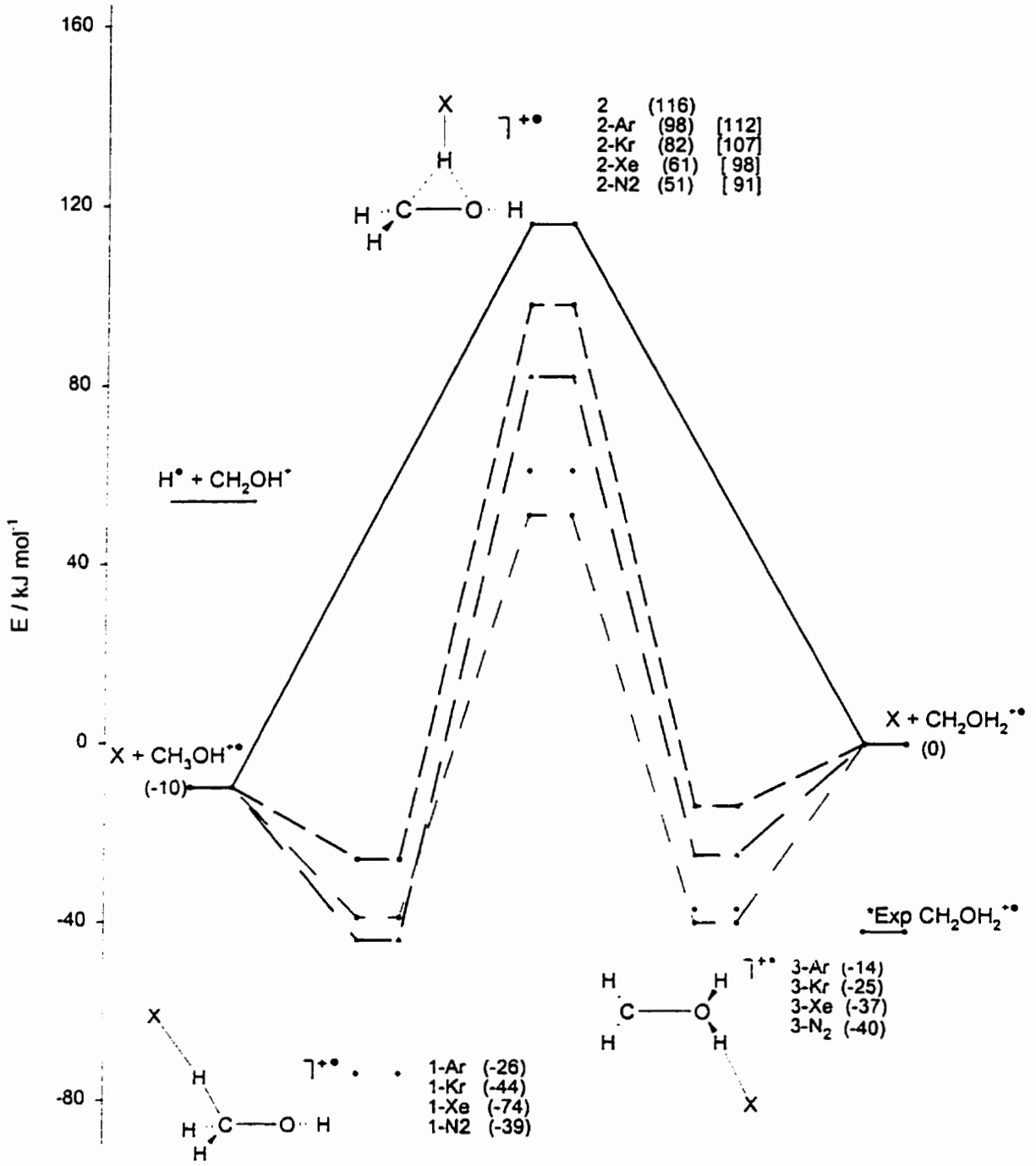

Figure 6.2. Schematic 298 K energy profile showing the uncatalyzed isomerization (solid line), and the Ar, Kr, Xe, and N_2 catalyzed isomerization reactions (dashed line, dash-dot line, dotted line, and dash-dot-dot line, respectively). The values in squared parentheses denote the barrier height with respect to the complexes 3-X. The energy of H + CH_2OH^+ is from ref. 19. Experimental value of $CH_2OH_2^{+\bullet}$ is relative to $CH_3OH^{+\bullet}$

shorter than in the **1-X** and **3-X** structures. This shorter bond distance can be thought of as owing to a strong interaction and stabilization of the transition structure. It is also apparent that the ratio of the H(3)-X bond distance in **2-X** to that in **1-X** (or **3-X**) decreases across the series Ar, Kr, Xe, N_2 which can be thought of as due to a greater stabilization of the transition structure across this series. Further evidence of this stronger interaction comes from the increasing H(3)-C and H(3)-O bond distances in the transition structures (**2-X**) over the same series; the H(3)-O bond distance increases from 1.218 Å in the unassociated structure (**2**) to 1.271 Å, 1.311 Å, 1.367 Å and 1.687 Å for the Ar-, Kr-, Xe- and N_2- associated transition structures respectively (see also Fig. 6.3).

We may also gain insight into the stabilization of the transition state by the catalysts from inspection of the charge distributions. The charge distributions obtained from the electrostatic potentials show that, on average 31% of the charge is on H(3) of the uncatalyzed transition state, **1**, while in the Ar-, Kr-, Xe-, and N_2-stabilized transition states 32, 34, 41 and 57% of the charge is on the XH(3) portion respectively (Fig. 6.3). This increase in charge on the XH(3) portion of the transition state is associated with an increase in positive charge on the catalyst. The average charge associated with H(3) decreases from 31% on the uncatalyzed transition structure to 14, 6 and 1% in the Ar-, Kr-, and Xe-stabilized transition state and is 16% in the N_2-stabilized structure. Thus on the X portion, the charge increases from 18% when X=Ar to 28, 40, and 41% when X=Kr, Xe and N_2, respectively. The charges on the catalysts in the respective transition states are

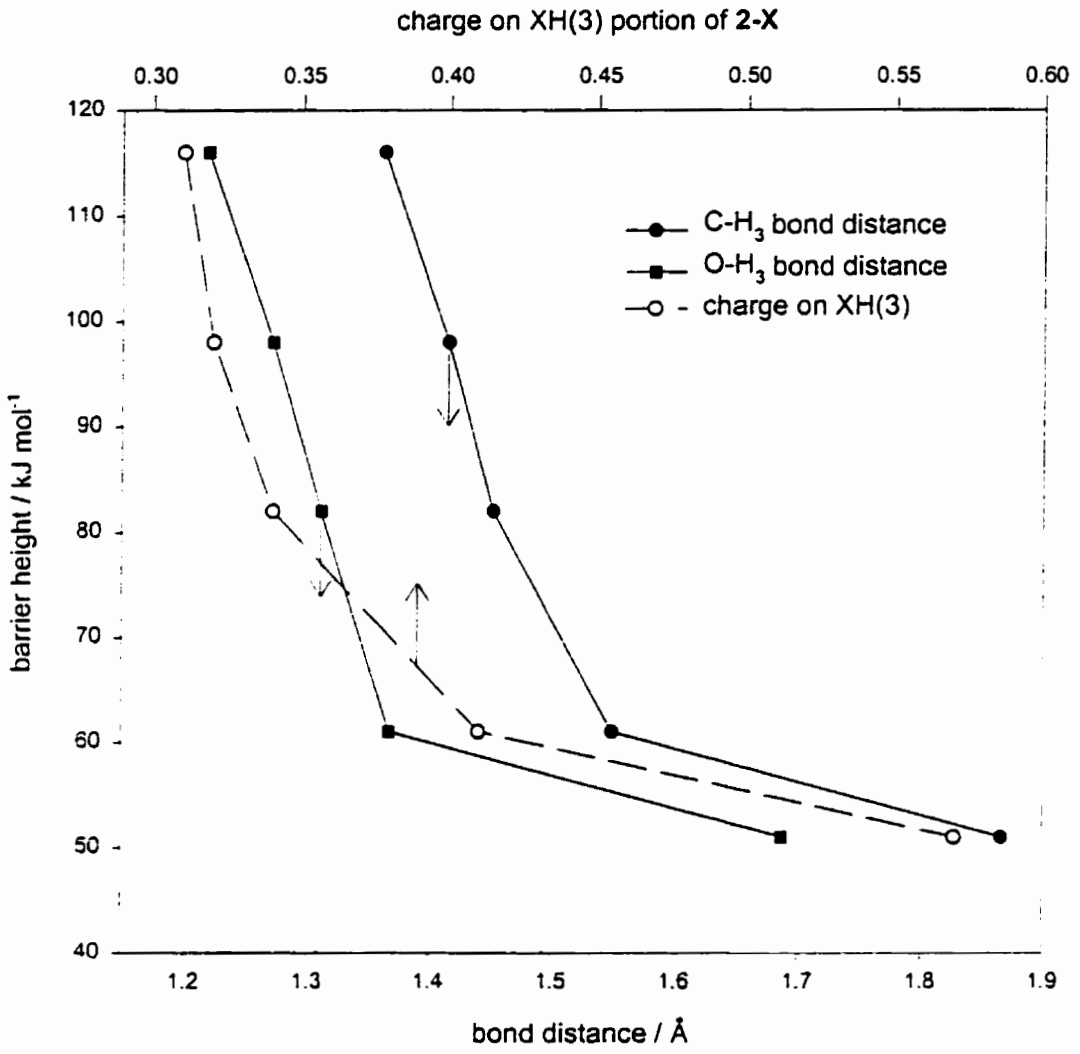

Figure 6.3. Plot showing the relationship of the barrier heights of the catalyzed and uncatalyzed 1 to 3 H-atom transfers with the C-H(3) and O-H(3) bond lengths in the predicted transition state, and the charge on the XH(3) portion of the transition state. The abscissa for the latter is at the top of the plot.

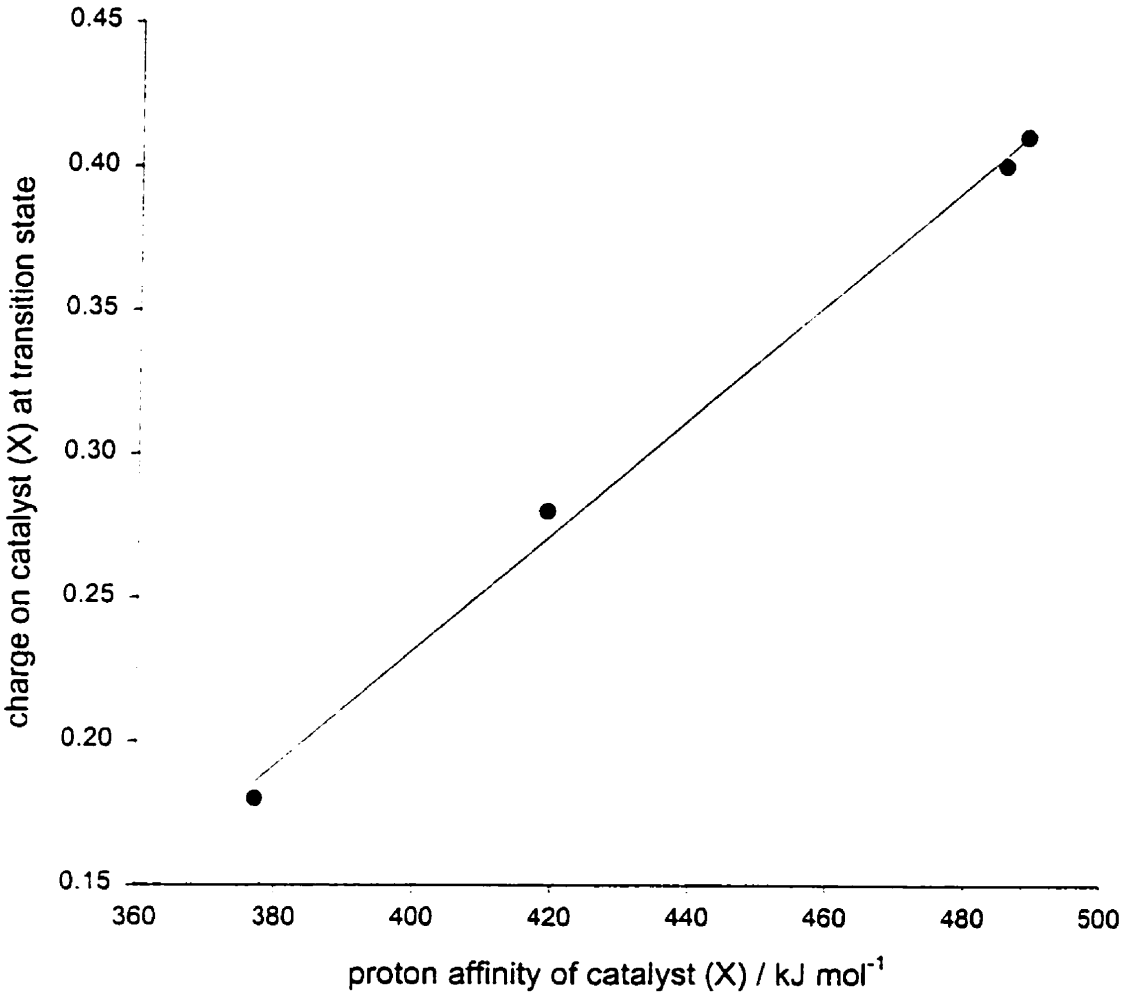

Figure 6.4. Plot showing the relationship between the calculated proton affinities and the calculated charge on the catalyst (X) derived from the electrostatic potentials.

plotted in Fig. 6.4 against their proton affinities and a linear relationship is obtained. It should be noted here that although the isomerization reactions discussed in this paper have been given the unfortunate misnomer "intramolecular proton transport," the identity of the migrating substituent more closely resembles that of a hydrogen atom in both the catalyzed and uncatalyzed reactions. Therefore, from here on, the process will be referred to as intramolecular H-atom transport.

With respect to the unpaired spin density, all transition states closely resemble $CH_2OH_2^{+\bullet}$ in that the radical centre is mostly on C. Neither the catalyst nor H(3) have any appreciable unpaired spin density consistent with a net transfer of charge to the stabilized ion from the catalyst through the H atom. In $CH_3OH^{+\bullet}$, the spin density is more evenly distributed between C and O but is still slightly greater on C. Since there is some extent of transfer of spin density from O to C, the reaction may also involve some degree of electron transfer but, this transfer is complete before the transition state is reached.

6.4 Discussion

6.4.1 Catalyzed Proton Transfer

In the work by Chalk and Radom,[12] it was realized that the calculated barrier height of the catalyzed isoformyl cation to formyl cation rearrangement decreased as the proton affinity of the catalyst increased. Similarly, the relationship between proton affinity of the catalyst and the charge distribution on the catalyst in the transition state depicted in Fig. 6.4 strongly suggests a linear relationship. In Fig.

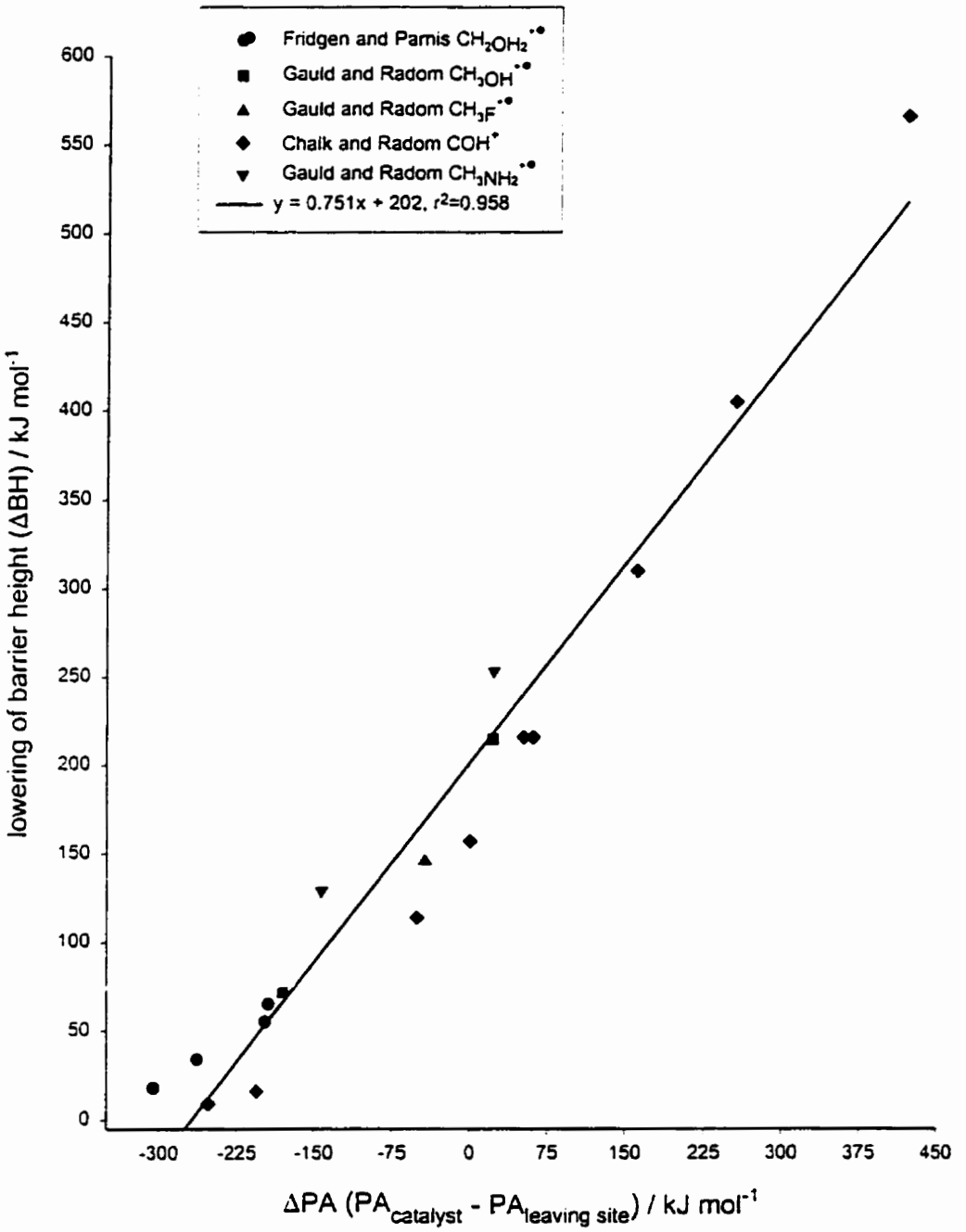

Figure 6.5. Plot of the lowering of the barrier height (ΔBH) against the difference in proton affinities of the catalyst and leaving site (ΔPA) for various 1,2-H atom shift isomerization reactions and various catalysts. Data taken from references 12 (diamonds), 16 (square, triangle, inverted triangle), and this work (circle).

6.5, is plotted the difference between the uncatalyzed barrier height and the catalyzed barrier height (ΔBH, for change in barrier height) versus the difference between the proton affinities of the catalyst and the leaving site of the proton (ΔPA).[45] It is immediately apparent that there is a convincing linear relationship between ΔBH and ΔPA. This linear relationship is even more striking when one considers that there are data from four different 1,2-proton shift isomerization reactions and twelve different catalysts in Fig. 6.5. The vertical line in Fig. 6.5 denotes where the proton affinities of the leaving site and the catalyst are equal (ΔPA=0). To the left of this line (ΔPA<0) the catalysts may act by stabilizing the transition structures as in mechanism II. Although all catalyzed reactions plotted in Fig. 6.5 and to the right of this line (ΔPA>0) have been calculated according to mechanism II the catalyst's proton affinities are actually larger than that of the leaving site's, and experimentally the 'forth and back' mechanism may be preferential over mechanism II. High proton affinity catalysts, such as NH_3, would actually extract the proton (intermolecular proton transfer) since it has a higher proton affinity than both the leaving and accepting site.

The correlation depicted in Fig. 6.5 suggests that one could easily assess the extent of barrier lowering that is possible and by what mechanism it may effect the outcome of a given experiment by knowing, or given reasonable estimates of, the proton affinities of the leaving site and the neutral base. For example, in experiments designed to measure rates of reactions involving hydrogen-containing cations or to measure branching ratios of competing reactions, this correlation could

be used to assess the possibility of catalysis of isomerization as an intermediate step before dissociation and to determine the likely mechanism. It also has value in the context of using appearance potential measurements to get at thermodynamic properties where neutral bases present as an 'inert' bath or as an impurity, may catalyze isomerization.

It is now recognized that rare-gas catalyzed H-atom transfer is likely to be an active mechanism in two recent electron bombardment matrix isolation (EBMI) studies including that reported in Chapter 4. In work by Zhang *et al.*,[46] 1-propen-2-ol was isolated and spectroscopically characterized in rare-gas matrices following periods of electron bombardment of gaseous rare gas/acetone mixtures (EBMI). It was assumed in that study that the 1-propen-2-ol observed was the neutralized isomerization product of the *electronically excited* (*A* state) of acetone radical cation. This *A* state mechanism arose due to the fact that the barrier to isomerization of the acetone radical cation to the 1-propen-2-ol radical cation is ~71 kJ mol^{-1} higher in energy than the lowest energy dissociation into the acetyl cation and methyl radical,[47] making isomerization of the cation in the ground state highly unlikely. The acetone radical cation to 1-propen-2-ol radical cation H-atom shift isomerization is not a 1,2-shift as is the **1** to **3** isomerization, but is a 1,3-H atom shift. We recognize that use of Figure 6.5 for this system is only of qualitative value, however, one may expect that the mechanisms to catalysis should be similar for 1,3- and 1,2-H-atom shifts. BP86/DN** calculations predict the ΔPA for Ar and the carbon site of $CH_3C(O)CH_2$ to be -469 kJ mol^{-1}. From Fig. 6.5 one can presume

that the argon present in these experiments would have little or no effect on the barrier height. In fact for catalysis by Ar, preliminary calculations predict that the barrier is lowered from the parent system by less than 1 kJ mol^{-1}. However, there are expected to be many other neutral bases present such as CO and H_2O (impurities and products) which have proton affinities that differ from that of $CH_3C(O)CH_2$ at the carbon site by much less, -189 and -100 kJ mol^{-1}, respectively. The extent of catalysis is estimated from Fig. 4 to be 60 and 127 kJ mol^{-1} for CO and H_2O, respectively. Both CO and H_2O would be expected, therefore, to stabilize the transition structure, thereby lowering the barrier such that the dominant process could be isomerization of the acetone radical cation to 1-propen-2-ol radical cation. It should also be noted that acetone has a higher proton affinity than either the C or O end of CH_2-CO-CH_3, and, therefore, catalysis would be impossible but self protonation would occur. Catalysis of the isomerization of acetone radical cation to 1-propen-2-ol radical cation has been observed using benzonitrile as the catalyst.[48] Benzonitrile, however, has a proton affinity which is greater than the C end but lower than the O end of CH_2-CO-CH_3 and, therefore, catalysis would follow the forth and back mechanism (mechanism I). More work using weaker bases as catalysts needs to be conducted in order to directly observe catalysis by mechanism II. Nevertheless, such catalysis may be plausible in the isomerization step of the ionization-isomerization-matrix isolation-neutralization mechanism proposed for the production of 1-propen-2-ol observed by Zhang *et al.* Detailed calculations aimed at assessing the catalytic effect of various neutral bases on 1,3

H-atom shifts are currently underway.

In chapter 4, it was concluded that the presence of species such as HDCO and $D_2COD^{\bullet}$ in the rare gas matrices after EBMI of gaseous mixtures of D_3COH diluted in rare gases was a result of a gas-phase decomposition of the isotopically labeled methanol radical cation following Ar-catalyzed proton transfer to the more thermodynamically-stable distonic cation.[44] The barrier to isomerization of the methanol radical cation is expected to be about 43 kJ mol^{-1} higher in energy than the lower energy dissociation to CH_2OH^+ and $H^{\bullet}$.[19] Since Ar is only expected to lower the isomerization barrier by about 18 kJ mol^{-1}, it may not be as likely that Ar is the catalyzing species, but rather impurities such as N_2, CO or H_2O. In experiments where Kr or Xe replaced Ar as the diluent gas, it is expected that they might be effective catalysts for the isomerization. Unfortunately, in that study the mixed isotope experiments were not conducted with Kr or Xe as the diluent gas.

6.4.2 The Density Functional Approach

It is quite obvious that there are some serious difficulties with employing even the best of the density functional theory approaches in attempting to predict thermodynamic and kinetic quantities for the ionic reactions presented in this chapter.

With respect to calculated energies, the BP86 method fails as is made clear by the relative energies of **1** and **3** on comparison with experimental and G2 values. The B3LYP- and B3PW91-calculated values are in better agreement using the

triple-ζ Gaussian basis sets, at least correctly predicting the proper ordering of the energies of the **1** and **3** isomers. It is important to note that there is little difference in the calculated energies by the addition of diffuse functions to the triple-ζ basis sets. The relative energies and proton affinities of **1**, however, are still not very reliable values employing any of the methods presented here. Obviously the G2 values are quite superior. However, the calculations with the Gaussian basis sets were performed on a 200 MHz PC with 32 MB of RAM and G2 calculations would be impossible to perform with such modest computer facilities. It is maintained, however, that these DFT calculations accurately predict the expected trend in Ar, Kr, Xe and N_2 catalytic effects of the **1** to **3** isomerization, as confirmed by the fact that the results obtained by this method, plotted in Fig. 6.5, are in line with the G2 results from the work of Radom's group.

6.5 Conclusions

The calculations presented here show that rare gases and N_2 can catalyze the $CH_3OH^{+\bullet}$ to $CH_2OH_2^{+\bullet}$ 1,2-H atom transport isomerization. The presence of Xe and N_2 may very well result in a catalytic effect such that the isomerization of the methanol radical cation to the distonic isomer competes against the lowest energy dissociation route which produces a hydrogen atom and the hydroxy methylene cation. In this work, the theoretical results of other groups as well as from this study have been used to show that there is a linear relationship between the difference in proton affinities of neutral base (catalyst) and the H leaving site of a radical

cation (ΔPA) and the barrier lowering of the isomerization process with respect to the separated base-cation pair (ΔBH). The effect of neutral bases, either as bath gases or impurities, should be considered seriously when conducting experiments with hydrogen-containing cations. Further experiments designed to test the theoretical results provided here need to be designed. Similarly, experimental and theoretical work needs to be conducted on 1,3- and 1,4-H-atom shift isomerization reactions.

It has also been shown that, although DFT methods are for the most part inferior to other computational modeling methods, fairly good results can be obtained with respect to the catalytic processes described in this paper. Further development of the DFT models used here needs to be done with respect to ionic potential energy surfaces before they will be useful in quantitative prediction of thermodynamic properties of ionic systems.

6.6 References to Chapter 6

1. For example see a) Glukhovtsev, M.N.; Szulejko, J.E.; McMahon, T.B.; Gauld, J.W.; Scott, A.P.; Smith, B.J.; Pross, A.; Radom, L. *J. Phys. Chem.* **1994**, *98*, 13099. b) Szulejko, J.E.; McMahon, T.B. *J. Am. Chem. Soc.* **1993**, *115*, 7839.
2. For example a) Bohme, D.K.; Mackay, G.I.; Schiff, H.I. *J. Chem. Phys.* **1980,** *73*, 4976. b) Bohme, D.K. *Trans. R. Soc. Can. Sect. 3* **1981**, *19*, 265.
3. Bohme, D.K. *Int. J. Mass Spectrom. Ion Processes***1992**, *115*, 95.
4. Strictly speaking this process is not a proton transfer, as it is commonly referred to in the literature. It is in fact an H-atom transfer. This point is addressed later in the chapter.
5. Gudeman, C.S.; Woods, R.C. *Phys. Rev. Lett.* **1982**, *48*, 1344.
6. Woods, R.C.; Dixon, T.A.; Saykally, R.J.; Szanto, P.G. *Phys. Rev. Lett.* **1975**, *35*, 1269.
7. Nobes, R.H.; Radom, L. *Chem. Phys.***1981**, *60*, 1.
8. Yamaguchi, Y.; Richards, C.A.Jr.; Schaefer, H.F. J. Chem. Phys. **1994**, *101*, 8945.
9. Freeman, C.G.; Knight, J.S.; Love, J.G.; McEwan, M.J. *Int. J. Mass Spectrom. Ion Processes* **1987**, *80*, 255.
10. Wagner-Redeker, W.; Kemper, P.R.; Jarrold, M.F.; Bowers, M.T. *J. Chem. Phys.* **1985**, *83*, 1121.
11. Dixon, D.A.; Komornicki, A.; Kraemer, W.P. *J. Chem. Phys.* **1984**, *81*, 3603.
12. Chalk, A.J.; Radom, L. *J. Am. Chem. Soc.* **1997**, *119*, 7573.
13. Cunje, A.; Rodriquez, C.F.; Bohme, D.K.; Hopkinson, A.C. *J. Phys. Chem.* **1998**, *102*, 478.
14. Ferguson, E.E. *Chem. Phys. Lett.* **1989**, *156*, 319.

15. Hansel, A.; Glantschnig, M.; Scheiring, C.; Lindinger, W.; Ferguson, E.E. *J. Chem. Phys.* **1998**, *109*, 1743.

16. Gauld, J.W.; Radom, L. *J. Am. Chem. Soc.* **1997**, *119*, 9831.

17. Bouma, W.J.; McLeod, J.K.; Radom, L. *J. Am. Chem. Soc.* **1982**, *104*, 2930.

18. Holmes, J.L.; Lossing, F.P.; Terlouw, J.K.; Burgers, P.C. *J. Am. Chem. Soc.***1982**, *104*, 2930.

19. Ma, N.L.; Smith, B.J.; Pople, J.A.; Radom, L. *J. Am. Chem. Soc.* **1991**, *113*, 7903.

20. Morgues, P.; Audier, H.E.; Lablanc D.; Hammerum, S. *Org. Mass Spectrom.* **1993**, *28*, 1098.

21. Audier, H.E.; Leblanc, D.; Morgues, P.; McMahon, T.B.; Hammerum, S. *J. Chem. Soc. Chem. Commun.* **1994**, 2329.

22. Gauld, J.W.; Audier, H.; Fossey, J.; Radom, L. *J. Am. Chem. Soc.* **1996**, *118*, 6299.

23. Curtiss, L.A.; Redfern, P.C.; Raghavachari, K.; Pople, J.A. *J. Chem. Phys.* **1998**, *109*, 42.

24. Jursic, B.S. *Chem. Phys. Lett.* **1998**, *284*, 281.

25. Jursic, B.S. *Theor. Chem. Acc.* **1998**, *99*, 171.

26. Jursic, B.S. *Theochem.* **1998**, *423*, 189.

27. Jursic, B.S. *Theochem.* **1997**, *418*, 11.

28. Jursic, B.S. *Theochem.* **1997**, *417*, 89.

29. Becke, A.D. *Phys. Rev.* **1988**, *A38*, 3098.

30. Becke, A.D. *J. Chem. Phys.* **1993**, *98*, 5648.

31. Perdew, J.P. *Phys. Rev.* **1986**, *B33*, 8822.

32. Lee, C.; Yang, W.; Parr, R.G. *Phys. Rev.* **1988**, *B37*, 785.

33. Perdew, J. P.; Wang, Y. *Phys. Rev.* **1992**, *B45*, 13244.

34. Hehre, W. J.; Lou, L., Eds. *A Guide to Density Functional Calculations in SPARTAN*, **1997**, Wavefunction, Inc., Irvine.

35. Spartan Version 5.0, Wavefunction, Inc., 18401 Von Karman Avenue, Suite 370, Irvine, CA 92612 USA.

36. Gaussian 94, Revision E.1, Frisch, M.J.; Trucks, G.W.; Schlegel, H.B.; Gill, P.M.W.; Johnson, B.G.; Robb, M.A.; Cheeseman, J.R.; Keith, T.; Petersson, G.A.; Montgomery, J.A.; Raghavachari, K.; Al-Laham, M.A.; Zakrzewski, V.G.; Ortiz, J.V.; Foresman, J.B.; Cioslowski, J.; Stefanov, B.B.; Nanayakkara, A.; Challacombe, M.; Peng, C.Y.; Ayala, P.Y.; Chen, W.; Wong, M.W.; Andres, J.L.; Replogle, E.S.; Gomperts, R.; Martin, R.L.; Fox, D.J.; Binkley, J.S.; Defrees, D.J.; Baker, J.; Stewart, J.P.; Head-Gordon, M.; Gonzalez, C.; Pople, J.A., Gaussian Inc., Pittsburgh PA, 1995.

37. Scott, A.P.; Radom, L. *J. Phys. Chem.* **1996**, *100*, 16502.

38. Scaling factors of 1.005(±0.004) and 1.016(±0.003) were obtained for the ZPVE's for the BP86/DN** and BP86/6-311G** methods, respectively. Similarly, scaling factors for $\Delta H_{vib}(298)$ were calculated to be 1.00(±0.05) and 0.98(±0.08) for the BP86/DN** and BP86/6-311G** methods, respectively

39. Gauld, J.W.; Radom, L. *J. Phys. Chem.* **1994**, *98*, 777.

40. Ma, N.L.; Smith, B.J. Radom, L. *J. Phys. Chem.* **1992**, *96*, 5804.

41. Yates, B.F.; Bouma, W.J.; Radom, L. *J. Am. Chem. Soc.* **1987**, *109*, 2250.

42. Tureček, F. *Int. J. Mass Spectrom. Ion Processes* **1991**, *108*, 137.

43. Lias, S.G.; Bartess, J.E.; Liebman, J.F.; Holmes, J.L.; Levin, R.D.; Mallard, W. *J. Phys. Chem. Ref. Data* **1988**, *17* Supp. 1.

44. Fridgen, T.D.; Parnis, J.M. *J. Chem. Phys.* **1998**, *109*, 2155.

45. The proton affinity of the leaving site is defined as follows, for the $CH_3OH^{+\bullet}$ to $CH_2OH_2^{+\bullet}$ isomerization it is the proton affinity of $CH_2OH^{\bullet}$ at carbon. For the reverse isomerization it would be the proton affinity of $CH_2OH^{\bullet}$ at oxygen. Similarly for the other reactions denoted in Figure 6.5.

46. Zhang, X.K.; Parnis, J.M.; Lewars, E.G.; March, R.E. *Can. J. Chem.* **1997**, *75*, 276.

47. Osterheld T.H.; Brauman, J.I. *J. Am. Chem. Soc.* **1993**, *115*, 10311.

48. Trikoupis, M.A.; Terlouw, J.K.; Burgers, P.C. manuscript submitted to J. Am. Chem. Soc.

Chapter 7

Summary and Future Work

7.1 Summary

The utility of matrix isolation for the study of gas-phase ion reactions has associated with it, many complications. The worst of these complications is that there are very many different products formed from one precursor. This problem could be solved by mass selection with a quadrupole mass filter prior to matrix isolation.

It has been shown in this work that the products observed in these experiments are, indeed, resultant from gas-phase ionic reactions. These reactions may be unimolecular in nature but due to the presence of an abundance of rare

gas, neutral decomposition products, and precursor, ion-molecule interactions cannot be disregarded as possible routes to the observed products.

It has been concluded in this work, that excited metastable states of the rare-gas atoms do not contribute significantly to the chemistry observed in these experiments. It has been determined that the chain of events occuring during these experiments is as follows. In the gas phase, due to the relatively large abundance of rare gas, the initial step is electron impact ionization of rare-gas atoms. Interaction of this rare-gas cation with the organic dopant (i.e. methanol) results in charge transfer and excitation of the newly formed radical cation by an amount of energy equal to the difference between the electron affinity of the rare-gas cation and the ionization potential of the dopant. Following ionization/excitation, the newly-born radical cation may undergo the various unimolecular decompositions which are available to it based on the amount of internal energy associated with it.

In these EBMI experiments there is much rare-gas and other neutral bases present. If the rare-gas cation contains hydrogen, such as $CH_3OH^{+\bullet}$ and $CH_3COCH_3^{+\bullet}$, interaction with neutral base may catalyze hydrogen-transfer isomerization to $CH_2OH_2^{+\bullet}$ or 1-propen-2-ol radical cation, respectively, before decomposition. Possible evidence of this has been observed in EBMI experiments on CD_3OH (chapter 4) where products observed included HDCO, $HCO^{\bullet}$, and $HDCOD^{\bullet}$. Furthermore, it is thermodynamically and kinetically feasible that interaction of $CH_3OH^{+\bullet}$ with rare gas may also result in proton abstraction to form RgH^+ and $H_2COH^{\bullet}$. This ion-molecule reaction has been proposed as a step in one

of the probable mechanisms to the formation of proton-bound rare-gas dimers.

It was shown in this work that there is a linear relationship between the difference in proton affinities of neutral base (catalyst) and the H leaving site of a radical cation (ΔPA) and the barrier lowering of the isomerization process with respect to the separated base-cation pair (ΔBH). The effect of neutral bases, either as bath gases or impurities, should be considered seriously when conducting experiments with hydrogen-containing cations. Further experiments designed to test the theoretical results provided here need to be designed. Similarly, experimental and theoretical work needs to be conducted to assess the catalytic effect of neutral bases on 1,3- and 1,4-H-atom shift isomerization reactions. Calculations are presently in progress on the 1,3-H-atom shift isomerization reactions.

7.2 Electron Bombardment Matrix-Isolation Studies

The electron bombardment matrix-isolation technique is a powerful one which should find great utility for spectroscopic characterization of both ions and neutral species. Spectroscopic data combined with *ab inito* calculations lead to structural information, which can only be obtained indirectly in mass spectrometric studies.

It has been shown that argon matrices are poor media for stabilization of cationic species; neon matrices would be a better compliment for this technique. Although most ions would be charge-stabilized in a neon matrix, the photoelectron

emission threshold decreases from 20.3 eV to 15.05, 13.48 and 11.60 by doping the neon matrix with less than 1% Ar, Kr, or Xe, respectively.[1] This would still allow one to easily access novel neutral isomers via the radical cation by charge-exchange neutralization within the stabilizing confines of the cryogenic matrix.

Similarly one may utilize the quenching capabilities of precursor or a dopant such as CO or N_2 when designing EBMI experiments for synthesis of novel species. Also, if the precursor contains hydrogen atoms one needs to be aware that neutral bases catalyze hydrogen migration. This can even be used as an advantage for the preparation and spectroscopic characterization of novel isomeric species.

7.3 Proton-Bound Rare-Gas Dimers

Studies of ionic species has been in the realm of mass spectrometrists since the implementation of mass spectrometry many decades ago. Within the last decade, however, the desire for direct observation of ion structures has led to the development of techniques whereby ions can be produced and stored with enough abundance that they can be observed by direct spectroscopic methods. Matrix-isolation spectroscopists have been the fore-runners of direct spectroscopic characterization and structure elucidation of ionic species to date. In matrices, however, the matrix host perturbs the ion somewhat such that the spectra recorded may not be representative of a gas-phase ion which may be present in the upper atmosphere or in interstellar space making the matrix spectra of only limited use when trying to identify gas-phase absorbers or emitters. For example, the centro-

symmetric proton-bound rare-gas dimers $RgHRg^+$ (where Rg=Ar, Kr or Xe) have been observed in rare-gas matrices but, theoretical calculations predict that the wavenumbers for their antisymmetric-stretching vibration is much higher than what is observed in the matrix. Furthermore, it has been shown in this work (chapters 4 and 5) that species such as $KrHKr^+$ observed in Kr matrices are shifted by unprecedentedly large amounts when observed in predominantly argon matrices. This suggests a large interaction with the matrix host or even that the gas-phase species and matrix-isolated species are different. For example, in chapter 5 it was postulated that the matrix-isolated species may be more accurately described as Rg_6H^+ It would be beneficial to observe the gas-phase spectra of these species in order to compare with the theoretically-predicted gas-phase wavenumbers and to provide a stepping stone for further modeling of matrix isolated ions in order to further understand the matrix-ion interactions.

In Prof. Terry McMahon's Fourier Transform Ion Cyclotron Resonance (FTICR) laboratory at the University of Waterloo, a joint project with Prof. Jim Sloan is currently under way where infrared spectra of gas-phase ions will be recorded in an ICR cell. A step-scan interferometer will be used to introduce light from a high intensity glo-bar source into the ICR cell. The ions will be irradiated for a period of time appropriate to induce approximately 20% dissociation (i.e. into RgH^+ and Rg) following which a FTICR mass spectrum will be recorded. The mirror position is then changed in order to 'scan' the infrared spectrum. The resulting spectrum will be the intensity difference as a function of the wavenumber of the radiation. With

this instrumentation it will be possible to observe the gas-phase infrared spectrum of the proton-bound rare-gas dimers. In fact, these species may be ideally suited to this experiment since the homogenous species (dimers where both rare-gas atoms are the same) are predicted by theory to have dissociation energies, D_{298}, of about 66 kJ mol^{-1}, for Rg=Ar and 74 and 75 kJ mol^{-1} for Rg=Kr and Xe, respectively. Moreover, these proton-bound rare-gas dimers are excellent absorbers of infrared radiation. Their antisymmetric stretching fundamentals have intensities[2] predicted to range from 4000 to 5400 km mol^{-1} and have also been observed to have strong $\nu_3 + n\nu_1$ combination bands.[3,4]

It has also been predicted in this work that the deuterated $RgHRg^+$ species and $(RgHRg')^+$ species, where Rg≠Rg', have lower dissociation energies than the hydrogen isotopomers. This is contrary to normal isotope effects on dissociation energies. If there is no significant energy barrier to dissociation, this inverse isotope effect can be measured in kinetic studies on the dissociation of these species. By utilizing mass spectrometry the dissociation energies of the proton-bound rare-gas dimers can be accurately determined in order to test the existing *ab initio* calculations.

The research described in this section will be of fundamental value to ion chemists, matrix-isolation spectroscopists, and computational chemists. Additionally, the proton-bound rare-gas dimers are possibly the simplest of this class of dimers and further underlying knowledge of these species will have impact in areas of chemistry such as biochemistry where many biological molecules are charged and interact via hydrogen bonds.

7.4 References to Chapter 7

1. Schwentner, N.; Koch, E.-E.; Jortner, J., *Electronic Excitations in Condensed Rare Gases (Chapter 3)*, **1985**, Springer-Verlag, Berlin.

2. Lundell, J. *J. Mol. Struct.* **1995**, *355*, 291.

3. Kunttu, H.M.; Seetula, J.A. *Chem. Phys.* **1994**, *189*, 273.

4. Kunttu, H.; Seetula, J.; Räsänen, M. Apkarian, V.A. *J. Chem. Phys.*,**1992**, *96*, 5630.